

AD/A-004 479

APPLICATION OF ADVANCED METHODS FOR IDENTIFICATION
AND DETECTION OF NUCLEAR EXPLOSIONS FROM THE ASIAN
CONTINENT

T. C. Bache, et al

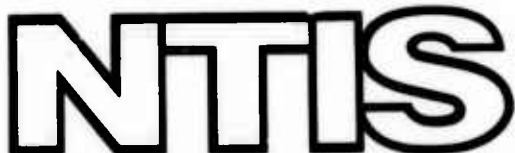
Systems, Science and Software

Prepared for:

Air Force Office of Scientific Research
Advanced Research Projects Agency

October 1974

DISTRIBUTED BY:



National Technical Information Service
U. S. DEPARTMENT OF COMMERCE

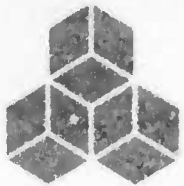
UNCLASSIFIED

SECURITY CLASSIFICATION OF THIS PAGE (When Data Entered)

REPORT DOCUMENTATION PAGE		READ INSTRUCTIONS BEFORE COMPLETING FORM
1. REPORT NUMBER AFOSR-TR-75-0206	2. GOVT ACCESSION NO.	3. RECIPIENT'S CATALOG NUMBER ADIA-004479
4. TITLE (and Subtitle) APPLICATION OF ADVANCED METHODS FOR IDENTIFICATION AND DETECTION OF NUCLEAR EXPLOSIONS FROM THE ASIAN CONTINENT		5. TYPE OF REPORT & PERIOD COVERED Interim
7. AUTHOR(s) T. C. Bache J. T. Cherry J. M. Savino		8. CONTRACT OR GRANT NUMBER(s) F44620-74-C-0063
9. PERFORMING ORGANIZATION NAME AND ADDRESS Systems, Science & Software La Jolla, CA 94550		10. PROGRAM ELEMENT, PROJECT, TASK AREA & WORK UNIT NUMBERS 62701E A0 1827
11. CONTROLLING OFFICE NAME AND ADDRESS Advanced Research Projects Agency 1400 Wilson Boulevard Arlington, VA 22209		12. REPORT DATE October 1974
14. MONITORING AGENCY NAME & ADDRESS (if different from Controlling Office) Air Force Office of Scientific Research/NP 1400 Wilson Boulevard Arlington, VA 22209		15. SECURITY CLASS. (of this report) Unclassified
		15a. DECLASSIFICATION/DOWNGRADING SCHEDULE
16. DISTRIBUTION STATEMENT (of this Report) Approved for public release; distribution unlimited.		
17. DISTRIBUTION STATEMENT (of the abstract entered in Block 20, if different from Report)		
18. SUPPLEMENTARY NOTES		
19. KEY WORDS (Continue on reverse side if necessary and identify by block number)		
<p style="text-align: center;">Reproduced by NATIONAL TECHNICAL INFORMATION SERVICE U.S. Department of Commerce Springfield VA 22151</p>		
20. ABSTRACT (Continue on reverse side if necessary and identify by block number) <p>This report presents the results of a continuing effort to obtain an optimum multi-discriminant/detection procedure for earthquakes and explosions occurring within the Asian Continent. Significant improvement of theoretical predictions of teleseismic ground motion from explosions was realized using a deterministic computer model which merges nonlinear shock code calculations with far-field stress wave propagation through a realistic earth structure. The addition to the seismic codes of the Thomson-Haskell matrix formulation and a split earth</p>		

structure capability provides for the inclusion of more realistic earth structure models in the near source and receiver regions and for the intervening path in the upper mantle. The resulting theoretical seismograms show a striking similarity to observations and indicate that a successful matched filter for event detection and discrimination, based on a substantial portion of an event signal, can be constructed.

ja



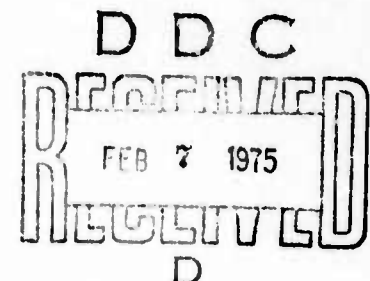
SYSTEMS, SCIENCE AND SOFTWARE

SSS-R-75-2483

APPLICATION OF ADVANCED METHODS FOR IDENTIFICATION AND DETECTION OF NUCLEAR EXPLOSIONS FROM THE ASIAN CONTINENT

T. C. Bache
J. T. Cherry
J. M. Savino

Semi-Annual Report



Contract No. F44620-74-C-0063

S³ Project 261

AIR FORCE OFFICE OF SCIENTIFIC RESEARCH (AFSC)
NOTICE OF TRANSMITTAL TO DDC
This technical report has been reviewed and is
October 1974 approved for public release, IAW AFR 190-12 (7b).
Distribution is unlimited.
D. W. TAYLOR
Technical Information Officer

P.O. BOX 1620, LA JOLLA, CALIFORNIA 92037. TELEPHONE (714) 453-0060

if

FOREWORD

This semiannual technical report entitled, "Application of Advanced Methods for Identification and Detection of Nuclear Explosions from the Asian Continent," is submitted by Systems, Science and Software (S^3) to the Advanced Research Projects Agency and to the Air Force Office of Scientific Research (AFOSR). This report presents the results of a continuing effort to obtain an optimum multi-discriminant/detection procedure for earthquakes and explosions occurring within the Asian Continent. The work is being performed under Contract Number F44620-74-C-0063. Mr. William J. Best is the AFOSR technical contracting officer.

Dr. J. Theodore Cherry is the S^3 project manager. Dr. Thomas C. Bache is responsible for the development and application of the seismic ground motion prediction work. Dr. John M. Savino is responsible for the analysis of the seismic data against which all theoretical developments must eventually be tested. Acting as consultants on the project are Professors Charles B. Archambeau of the University of Colorado and David C. Harkrider of the California Institute of Technology.

ABSTRACT

Significant improvement of theoretical predictions of teleseismic ground motion from explosions was realized using a deterministic computer model which merges nonlinear shock code calculations with far-field stress wave propagation through a realistic earth structure. The addition to the seismic codes of the Thomson-Haskell matrix formulation and a split earth structure capability provides for the inclusion of more realistic earth structure models in the near source and receiver regions and for the intervening path in the upper mantle. The resulting theoretical seismograms show a striking similarity to observations and indicate that a successful matched filter for event detection and discrimination, based on a substantial portion of an event signal, can be constructed.

Parameter studies for different near source and receiver earth structures clearly demonstrate how the conventional procedure employed for body-wave magnitude calculations introduces scatter into the determinations. A more consistent technique for m_b determinations is presented here and is expected to result in more accurate scaling relationships for events of different yields.

A variable frequency magnitude technique, designed to exploit spectral differences between earthquakes and explosions, was developed and applied to short-period recordings of a large population of Eurasian events. Complete discrimination between all explosions and shallow earthquakes down to m_b (LASA) ~ 4.5 was achieved. This technique was found to discriminate various multiple explosion scenarios as well.

TABLE OF CONTENTS

	Page
I. INTRODUCTION	1
II. DETERMINISTIC PREDICTION OF TELESEISMIC GROUND MOTION FROM EARTHQUAKES AND UNDER-GROUND EXPLOSIONS	3
2.1 EQUIVALENT ELASTIC SOURCE REPRESENTATION .	4
2.2 TELESEISMIC BODY WAVES	7
2.3 TELESEISMIC SURFACE WAVES	11
2.4 EFFECTS OF CRUSTAL STRUCTURE ON EXPLOSION GENERATED P WAVES	15
III. DATA ACQUISITION, EDITING AND ANALYSIS	33
3.1 DATA ACQUISITION AND EDITING	33
3.2 DATA ANALYSIS	34
IV. SPECTRAL MAGNITUDE DISCRIMINANT	36
4.1 TECHNIQUE	36
4.2 EVENTS RECORDED AT LASA	37
4.3 MULTIPLE EVENTS	43
V. CONCLUDING REMARKS	50
REFERENCES	51
APPENDIX	54

I. INTRODUCTION

The objective of the research program described in this report is to merge relevant knowledge from rock mechanics, numerical simulation of stress wave propagation, information theory and seismology to obtain an optimum multi-discriminant/detection procedure for earthquakes and explosions occurring within the Asian continent. During the first half year of the program, work has proceeded in several task areas including:

1. Refine and improve the S³ capability for a deterministic prediction of teleseismic ground motion due to underground explosions and earthquakes;
2. Collect and analyze ground motion data from a variety of seismic networks;
3. Design a multi-discriminant procedure for detecting and discriminating nuclear explosion events;
4. Test suggested detection/discrimination procedures, both conventional and newly designed, using actual seismic data.

The seismic code package now operational at S³ consists of more than twenty separate computer codes written over a period of years by many different programmers. These codes include the capability to compute the elastic wave generated by a realistic, large displacement, nonlinear explosion source and to propagate the resulting body and surface waves to teleseismic distances where synthetic seismograms are generated. The code package also includes a versatile seismic data analysis capability.

Recent additions and improvements to the seismic codes are discussed in Section II and III of this report. Of particular interest is the addition of crustal reverberations

to the body wave propagation codes. Preliminary results illustrating the influence of crustal structure on the seismograph record are presented in Section II.

A recently suggested variable frequency magnitude discriminant^[22] employing spectral magnitudes computed from short period compressional waves is being carefully tested and is discussed in Section IV.

Finally, the application of our modeling capability to study the dependence of seismic magnitudes on yield, near source material properties, depth of burial and earth structure was the subject of an S³ report prepared in August at AFOSR request^[4]. This report is included as Appendix A.

II. DETERMINISTIC PREDICTION OF TELESEISMIC GROUND MOTION FROM EARTHQUAKES AND UNDERGROUND EXPLOSIONS

Combining relevant knowledge from rock mechanics, numerical simulation of stress wave propagation and seismology, a deterministic prediction of teleseismic ground motion from earthquakes and underground nuclear explosions has been developed at S³ and is rapidly being improved. This capability and its application to a variety of problems is described in References 1-4 and 7.

Fundamental to the computational techniques applied is the representation of the source in terms of an equivalent elastic source. Various linear wave propagation techniques may then be applied to compute teleseismic body and surface waves. The equivalent elastic source may be obtained for a variety of earthquake and explosion source models including:

1. A realistic large displacement, nonlinear finite difference calculation of the explosion generated shock wave and its conversion to an elastic wave. In most cases a one-dimensional (spherically symmetric) calculation will suffice; when required, two-dimensional (axisymmetric) calculations have also been used.
2. The relaxation of the prestressed material surrounding the explosion induced cavity (tectonic release) using a theoretical model developed by Archambeau. [5]
3. An analytical/numerical earthquake model of the relaxation type developed by Archambeau and Minster. [6,7]

Having the equivalent elastic source representation, Rayleigh and Love surface waves are computed using a

computational technique developed by Harkrider^[9] based on the Thomson-Haskell matrix method.

The propagation of body waves is accomplished using a combination of geometric ray theory and Thomson-Haskell matrix methods in a layered earth model. The anelastic attenuation parameter, generally denoted by the material quality factor, Q , is included in this analysis.

The remainder of this section includes a more detailed description of the equivalent elastic source representation and the techniques used to compute teleseismic body and surface waves, in particular those features to which improvements have been made since our August report^[4] which is included as Appendix A.

2.1 EQUIVALENT ELASTIC SOURCE REPRESENTATION

The Fourier transformed equations of motion in a homogeneous, isotropic, linearly elastic medium may be written

$$\hat{\mathbf{u}} = -\left(\frac{1}{k_p^2}\right) \nabla \hat{\chi}_4 + \left(\frac{2}{k_s^2}\right) \nabla \times \hat{\chi} \quad (2.1)$$

where $\hat{\mathbf{u}}$ is particle displacement and k_p and k_s are the compressional and shear wave numbers. The Cartesian potentials $\hat{\chi}_4$ and $\hat{\chi}$ are defined by

$$\begin{aligned} \hat{\chi}_4 &= \nabla \cdot \hat{\mathbf{u}} \\ \hat{\chi} &= \frac{1}{2} \nabla \times \hat{\mathbf{u}} \end{aligned} \quad (2.2)$$

and may be easily shown to satisfy the wave equation

$$\nabla^2 \hat{\chi}_\alpha - k_\alpha^2 \hat{\chi}_\alpha = 0, \quad \alpha = 1, 2, 3, 4, \quad (2.3)$$

where $k_4 \equiv k_p = \omega/v_p$, $k_i \equiv k_s = \omega/v_s$, $i = 1, 2, 3$. This equation has as a solution the following expansion in spherical eigenfunctions (e.g., Morse and Feshbach, [10]),

$$\hat{x}_\alpha(r, \omega) = \sum_{n=0}^{\infty} h_n^{(2)}(k_\alpha r) \sum_{m=0}^n \left[\hat{A}_{nm}^{(\alpha)}(\omega) \cos m\phi + \hat{B}_{nm}^{(\alpha)}(\omega) \sin m\phi \right] * P_n^m(\cos \theta) \quad (2.4)$$

where the $h_n^{(2)}$ are spherical Hankel functions of the second kind and the P_n^m are associated Legendre functions. The vector \vec{r} has as components the spherical coordinates r, θ, ϕ .

Equations (2.4) together with (2.1) provide an equivalent elastic source representation of the outgoing elastic waves. The values of the multipole coefficients $\hat{A}_{nm}^{(\alpha)}(\omega)$, $\hat{B}_{nm}^{(\alpha)}(\omega)$, $\alpha = 1, 2, 3, 4$, prescribe the displacement field at all points in the homogeneous elastic medium where (2.1) applies.

Given the displacement, \hat{u}_i , or, alternatively, the potentials \hat{x}_α , one may determine the multipole coefficients using (2.4). For example, using the orthogonality of the spherical eigenfunctions, one may derive

$$\begin{Bmatrix} \hat{A}_{nm}^{(\alpha)}(\omega) \\ \hat{B}_{nm}^{(\alpha)}(\omega) \end{Bmatrix} = \frac{c_{nm}}{h_n^{(2)}(k_\alpha r)} \int_0^{2\pi} \int_0^\pi \hat{x}_\alpha(r, \omega) P_n^m(\cos \theta) \begin{Bmatrix} \cos m\phi \\ \sin m\phi \end{Bmatrix} \sin \theta d\theta d\phi \quad (2.5)$$

where

$$c_{nm} = \frac{(2n+1)(n-m)!}{2\pi(n+m)!}, \quad m \neq 0,$$

$$c_{n0} = (2n+1)/4\pi.$$

That is, given the displacements, $\hat{u}(r, \omega)$ on a sphere of radius r , one can use (2.2), (2.5) and (2.4) to compute the displacements at any point in the elastic regime. This procedure was first suggested for geophysical applications by Archambeau.^[11]

Using the equivalent elastic source representation, highly nonlinear finite difference calculations of the near source earthquake or explosion displacement fields may be coupled to the elastic field where efficient elastic wave propagation techniques may be applied. Carrying the nonlinear computation out to a radius at which the material response is in the elastic regime, Eq. (2.5) may be applied to compute the multipole coefficients and thereby the equivalent elastic source.

For a spherically symmetric explosion, the explosion induced elastic field is often represented by the reduced displacement potential, $\psi(\tau)$, defined by (e.g., Cherry, et al.),^[1]

$$u_r(r, t) = \frac{\psi(\tau)}{r^2} + \frac{1}{rv_p} \frac{d\psi(\tau)}{d\tau}, \quad (2.6)$$

where $\tau = t - r/v_p$, is the retarded time. Note that $\psi(\tau)$ is independent of r .

Applying the Fourier transform, (2.6) becomes

$$\hat{u}_r(r, \omega) = \frac{(1 + ik_p r)}{r^2} e^{-ik_p r} \hat{\psi}(\omega). \quad (2.7)$$

Then, carrying out the algebra (observing that the \hat{u} of (2.2) is the Cartesian displacement vector), it may be shown that the multipole coefficients reduce to a single nonzero term, the monopole:

$$\hat{A}_{00}^{(4)}(\omega) = -ik_p^3 \hat{\psi}(\omega) . \quad (2.8)$$

For more complicated sources, additional nonzero coefficients are present. For example, in the case of an explosion in an axisymmetric cavity the coefficients $\hat{A}_{n_0}^{(4)}$, $\hat{B}_{n_1}^{(1)}$, $\hat{A}_{n_1}^{(2)}$, $n = 2, 4, 6 \dots$, are also nonzero.^[2] Also, Archambeau^[6] has given a theory for tectonic stress release due to underground explosions which gives nonzero quadrupole coefficients $\hat{A}_{2m}^{(\alpha)}$, $\hat{B}_{2m}^{(\alpha)}$, $m = 0, 1, 2$.

2.2 TELESEISMIC BODY WAVES

The basic technique used for propagating source (given by an equivalent elastic source representation) generated body waves through a layered earth structure is geometric ray theory in a layered earth model, including the anelastic attenuation parameter Q .^[1] One layered earth model may be used to represent the earth structure beneath the source while a second represents the earth structure in the receiver half of the travel path. The ray crosses into the second (receiver) structure at its point of deepest penetration which, for teleseismic distances, is deep within the mantle where lateral inhomogeneities are thought to be small.

The unembellished ray theory described above has been quite successful in illuminating the important gross properties of the teleseismic body wave record (see Appendix A). Additional complexities observed on the records are thought to be the result of crustal structure details in the source and receiver regions. These details may be included using Thomson-Haskell matrix techniques.

The propagation of body waves is shown schematically in Fig. 2.1. Referring to the figure, the options available for propagating body waves are as follows:

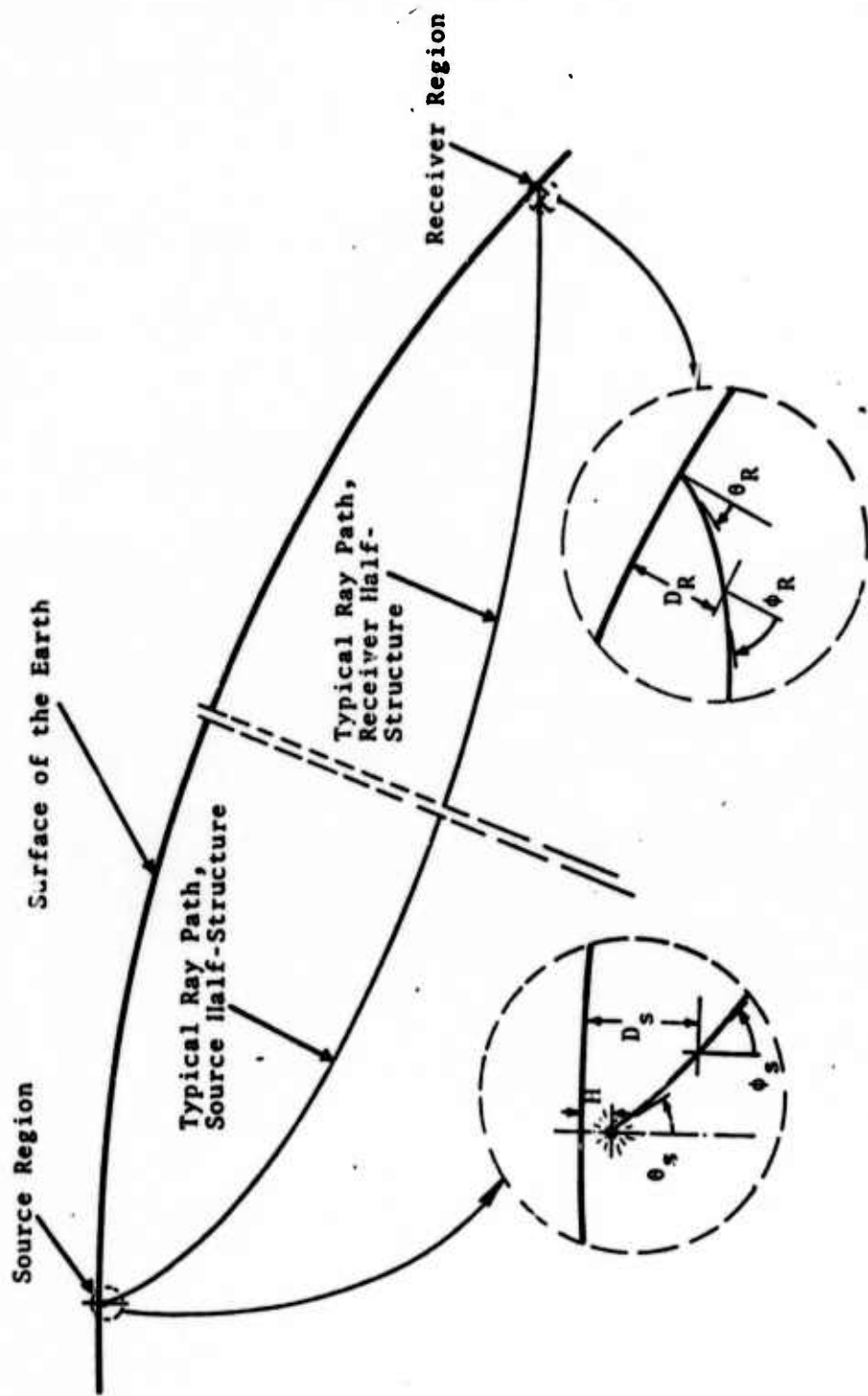


Figure 2.1. Schematic view of body wave propagation from a source at a depth H to a receiver at distance R through four layered earth models. Four layered earth models may be used to represent different portions of the path: (1) Crustal structure of thickness D_s in the source region; (2) Mantle structure for the source region; (3) Mantle structure for the receiver region; (4) Crustal structure of thickness D_R for the receiver region.

1. Geometric ray theory with an average earth structure for the entire travel path (available in 1973).
2. Geometric ray theory with two earth structure models, one for the source region and one for the receiver region (used in preparing Appendix A in August).
3. Use Haskell matrices for receiver crustal structure (recently added).
4. Use Haskell matrices for source region crustal structure (recently added).

Therefore, if $\hat{u}_s(\omega)$ is the far-field component of the source generated displacement spectrum, then the ground motion spectrum, $\hat{u}_R(\omega)$, at teleseismic distances is

$$\hat{u}_R(\omega) = \hat{u}_s(\omega) \cdot T_s^G(\omega) \cdot T_R^G(\omega) \cdot T_s^H(\omega) \cdot T_R^H(\omega), \quad (2.9)$$

where T_s^G and T_R^G represent transfer functions computed by ray theory for the source and receiver structures and T_s^H and T_R^H represent transfer functions computed by Haskell matrices for the source and receiver structures. The ray theory transfer functions include attenuation and dispersion via the material quality factor, Q . The effective Q for the ray travel path is used in the multiplicative factor

$$\exp \left\{ - \frac{\omega T}{2Q} \left(1 + \frac{2i}{\pi} \ln \frac{\omega_h}{\omega} \right) \right\}, \quad (2.10)$$

where T is the travel time and ω_h is a high frequency cutoff, generally set to $\approx 2000\pi$ (the results are rather insensitive to this parameter).

The appropriate theory for the transfer function $T_R^H(\omega)$ has been given by Haskell.^[13] Using his notation, for incident P waves the transfer function is

$$T_R^H(\omega) = 2c(J_{41} - J_{31})/\alpha_n D , \quad (2.11)$$

for the vertical component and

$$T_R^H(\omega) = 2c(J_{42} - J_{32})/\alpha_n D , \quad (2.12)$$

for the radial component of motion. The phase velocity $c = \alpha_n \csc(\phi_R)$ where ϕ_R is computed by ray theory (Fig. 2.1).

At present the transfer function $T_S^H(\omega)$ can only be computed for the case of the spherically symmetric point source for which the equivalent elastic source is given by Eq. (2.8). The transfer function for the wave emerging at an angle ϕ_s from the source crustal structure (see Fig. 2.1), including a point source at a depth of burial H, has been derived by Fuchs.^[14] Normalizing on the displacement for the same source in a halfspace of the source layer material, this transfer function may be written

$$T_S^H(\omega) = 2 \alpha_s^2 \rho_s \sin \phi_s \cos \phi_s \left[-\frac{i}{K} \bar{\Delta}_V' + i \bar{\Delta}_H \right] , \quad (2.13)$$

where the notation of Fuchs, Eq. (3.26), has been used.

Fuchs also gives the appropriate transfer function for a double couple source which can be modified to compute $T_S^H(\omega)$ for an explosion plus tectonic release. However, this has not yet been implemented.

It would be desirable to have a general theory by which an equivalent elastic source including any number of

multipole coefficients could be introduced into a Haskell matrix representation of the crustal structure. Such a theory has been developed for surface waves by Harkrider and Archambeau,^[15] setting forth the procedure to be followed.

At present, the attenuation parameter Q is not included in the Haskell matrix computations. However, an elementary modification by which inclusion of Q may be accomplished has been suggested by Hasegawa.^[16] This will be implemented in the near future.

2.3 TELESEISMIC SURFACE WAVES

Consider a source of pure dilatation in one layer, denoted s , of a multilayered material. Then the spectrum of the vertical Rayleigh wave displacement, $\bar{\omega}_0$, is given by Harkrider^[9] as

$$\hat{\omega}_0 = -i4\pi\mu_s \hat{\psi}_s(\omega) k_R K_{R-R} A_R e^{i\tau_s} H_0^{(2)}(k_R r) \quad (2.14)$$

where

μ_s = rigidity of the material in layer s ,

$\hat{\psi}_s(\omega)$ = Fourier transformed reduced displacement potential,

$k_R = \omega/c_R$, where c_R is the Rayleigh wave velocity at the frequency ω ,

K_R = depth dependent Rayleigh wave excitation factor,

A_R = amplitude response of the multilayered material,

$\tau_s = \omega R_0/\alpha_s$, where R_0 is the effective cavity radius for the explosion and

α_s is the P wave velocity in layer s,

$H_0^{(2)}(k_R r)$ = spherical Hankel function of the second kind.

A similar formula applies for a source specified by a general equivalent elastic source representation.

Surface wave calculations using this formulation are presented in, for example, Appendix A. However, one weakness of this approach is that only a single (average) earth structure model can be used for the entire source-receiver travel path. For surface waves traversing significant discontinuities such as those at oceanic-continental boundaries, large errors may be introduced.

In order to improve our surface wave computational capability, our computer programs are presently being modified to include the option of propagation over a mixed path. In particular, the path may be composed of two earth structure models; the source medium, 1, and the receiver medium, 2. While the modifications will be valid for a general source, it is once again convenient to present them in the context of the center of dilatation.

For a mixed path, the approximate vertical displacement Rayleigh wave spectrum for a selected mode is given by

$$\{\hat{\omega}_0\} = -4\pi\mu_{s_1}\hat{\psi}_{s_1}(\omega) k_{R_1} K_{R_1} A_{R_1} T_{R_1 2} H_0^{(2)}(k_{R_1} r_i + k_{R_2} r_2) e^{-(\gamma_{R_1} r_1 + \gamma_{R_2} r_2)} \quad (2.15)$$

where the subscript denotes media 1 or 2. The total path r is defined as

$$r = r_1 + r_2 \quad (2.16)$$

Assuming that the total horizontal energy flux for a given Rayleigh wave mode remains constant in the process of transmission across the boundary separating the two media, we have

$$T_{R_{12}} = \left(\frac{W_{R_1}}{W_{R_2}} \right)^{1/2} \quad (2.17)$$

where W_{R_i} is the total horizontal energy flux in medium i normalized to a unit vertical displacement at the surface.

The normalized energy flux is given by [17]

$$W_{R_i} = 2E_i U_i \quad (2.18)$$

where U_i is the group velocity and E_i is the total potential or kinetic energy at a particular frequency normalized to the surface vertical displacement.

This correction factor, which has given satisfactory results in predicting the amplitude changes of plane Rayleigh waves traveling across a lateral boundary, has been given by McGarr [18] and McGarr and Alsop. [19] It assumes that there is little or no mode conversion or reflection at the boundary, that the boundary is far enough from the source so that the wave front has small lateral curvature and that the wave front is parallel to the boundary, i.e., no refraction effects are included.

The validity of this approximation has been verified by wave propagation studies in laterally heterogeneous media using the finite difference numerical technique (D. Boore, personal communication to R. Alewine). [20]

For more than two media in the propagation path we can generalize under the same assumption to

$$T_{Rin} = \left(\frac{E_1 U_1}{E_n U_n} \right)^{1/2} \quad (2.19)$$

and the propagation phase and decay terms become

$$H_0^{(2)} \left(\sum_{i=1}^n k_{Ri} r_i \right) \quad (2.20)$$

and

$$\exp \left\{ - \sum_{i=1}^n \gamma_i r_i \right\} \quad (2.21)$$

respectively.

The implementation of the theory described above is expected to substantially enhance our surface wave computational capability.

2.4 EFFECTS OF CRUSTAL STRUCTURE ON EXPLOSION GENERATED P WAVES

Preliminary results illustrating the effect of the crustal structure in the source and receiver regions are presented in this section.

Consider a typical explosion of moderate yield. The far-field component of the displacement pulse generated by such an explosion is shown in Fig. 2.2. Plotted is $\dot{\psi}(\tau)/v_p$ which, at large r , is the far-field displacement (see Eq. (2.6)). The time scale is appropriate to a yield of 20 kT.

According to Eq. (2.9), propagation of the source generated stress wave to teleseismic distances is accomplished by convoluting with transfer functions representing the effects of the crust and upper mantle. Synthetic seismograms can then be generated by convolution with a transfer function representing the response of the seismometer of interest.

Consider first the synthetic seismogram computed using geometric ray theory to represent the entire travel path. In Fig. 2.3 is shown such a seismogram for an explosion at a burial depth such that the average source-to-surface travel time for P waves is 0.2 sec. The epicentral distance is approximately 4000 km and the ray path is characterized by $T/Q = 1.1$, where T is the travel time. Since the arrival time lag between the direct (P) and free-surface reflected (pP) phases is so small (≈ 0.4 sec), the wave train appearing on the seismogram represents a combination of the two phases. The amplitudes given on this and succeeding seismograms are in millimicrons. Also, the time scale on this and succeeding seismograms is relative in that the zero point has no consistent relation to explosion detonation time.

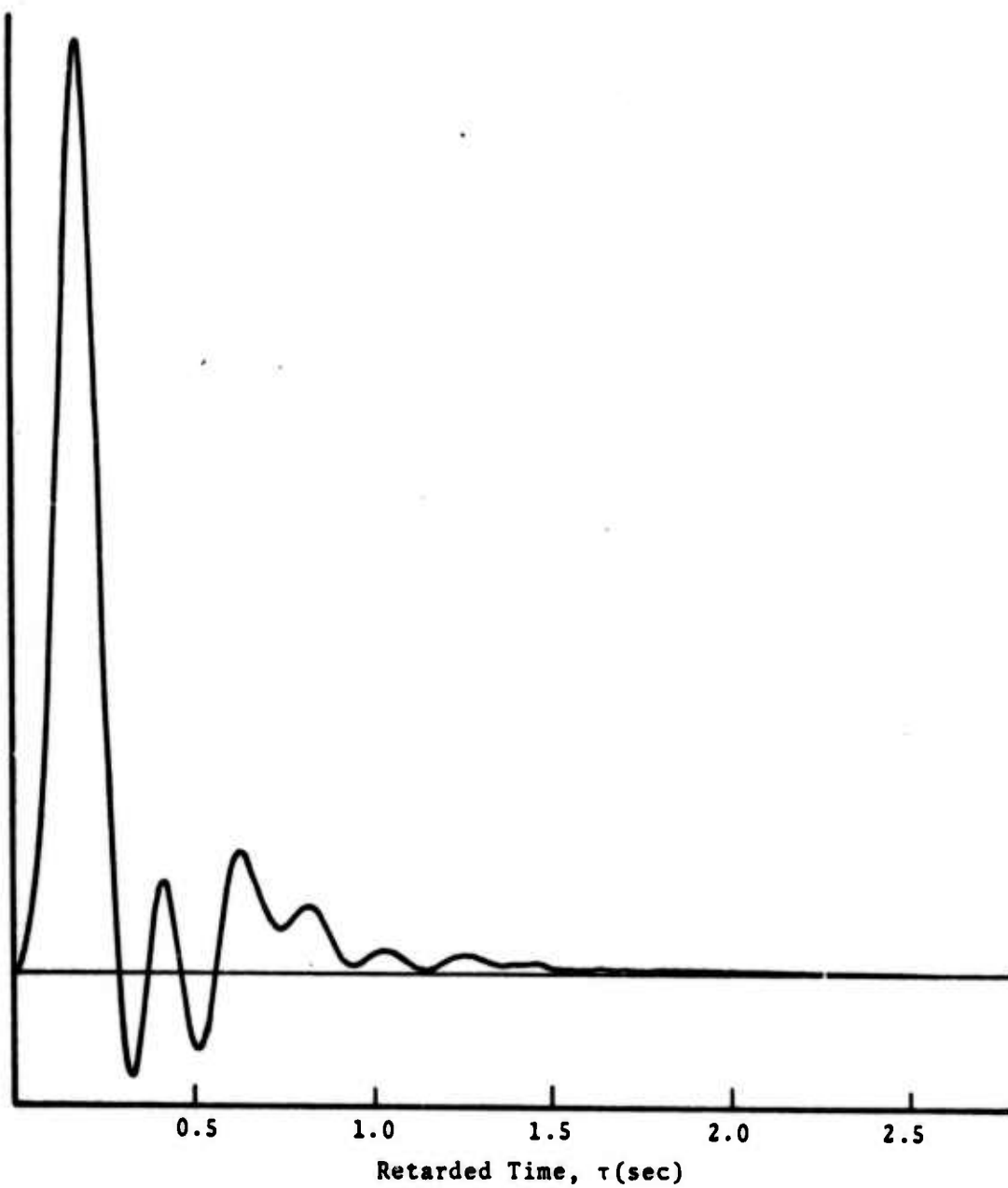


Figure 2.2. The far field component of the displacement pulse ($\psi(\tau)/v_p$) for a typical explosion of moderate yield. The time scale is appropriate to a yield of 20 kT. No amplitude scale is given since the amplitude scales with distance from the source and the properties of the source region (see Appendix A).

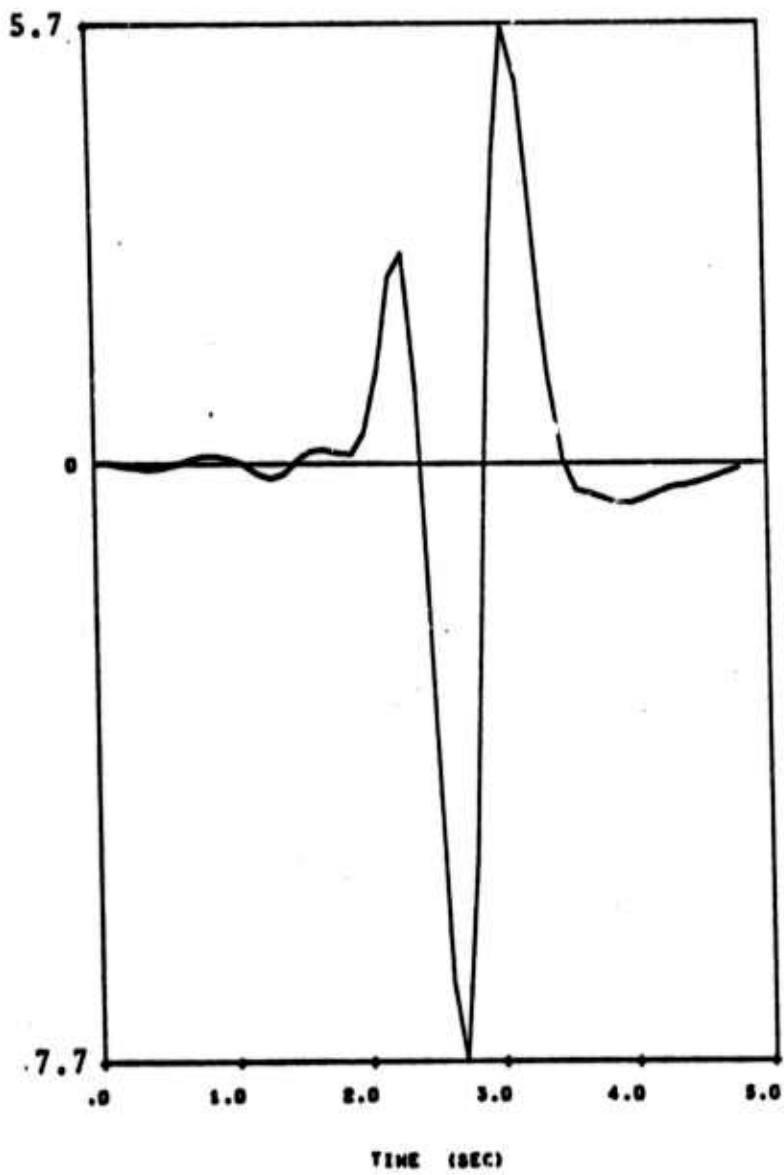
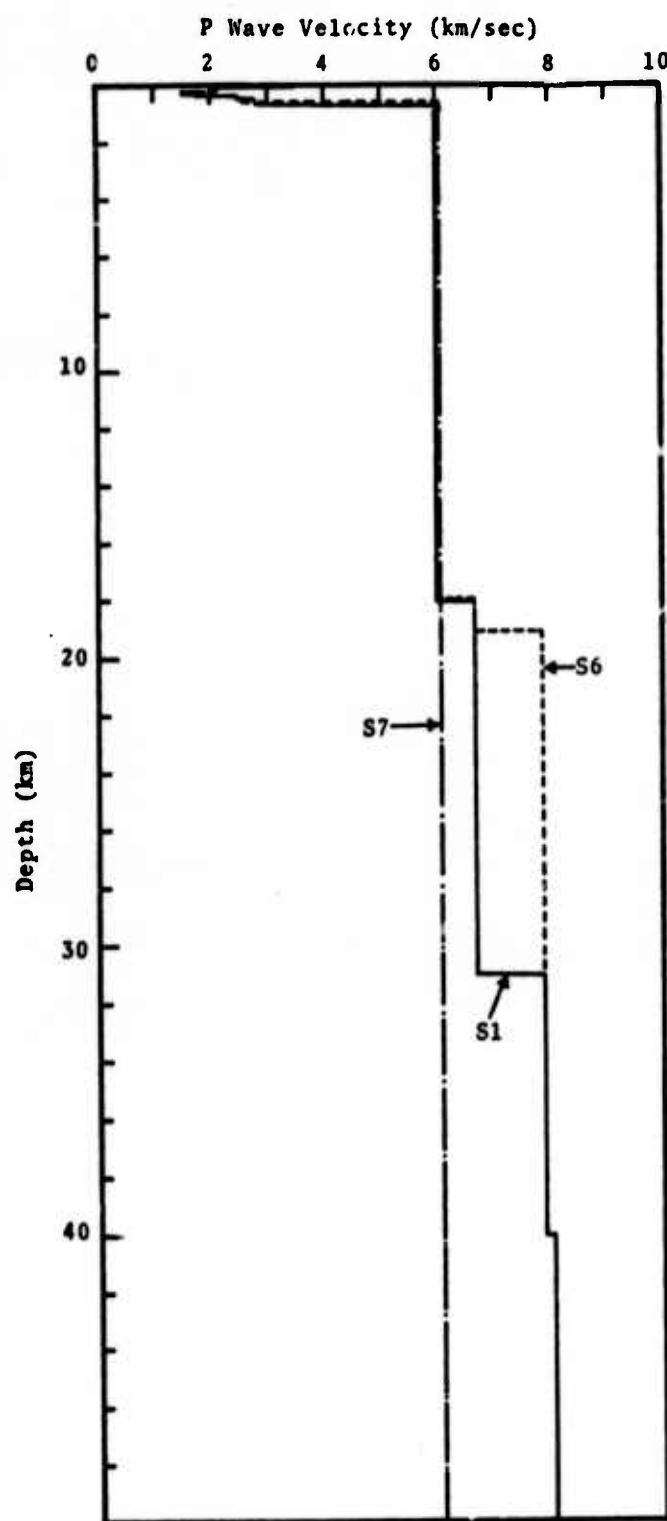


Figure 2.3. Synthetic seismogram for an explosion of 10 kT as recorded by Instrument #1 at \approx 4000 km. Geometric ray theory was used for the entire travel path with $T/Q = 1.1$.

The nature of the effect of the source region crustal structure on the seismogram may be seen by examining a series of seismograms for which the transfer function due to the source crustal structure has been included in the calculation. The P wave velocity profiles for several crustal structures typical of NTS are shown in Fig. 2.4. As seen in the figure, the main differences between these structures are restricted to the top kilometer. In Fig. 2.5 synthetic seismograms illustrating the effect of the source crustal structure S1 of Fig. 2.4 are shown. In Fig. 2.5a the upper mantle model used for the ray theory portion of the calculation was identical to that used for computing the seismogram of Fig. 2.3. Therefore, comparing Figs. 2.3 and 2.5a, the effect of adding to the calculation a detailed model of the source region crustal structure is seen. When making this comparison, it should be noted that two different instrument response functions were used for the two calculations. However, as will be demonstrated below, this has a minor effect.

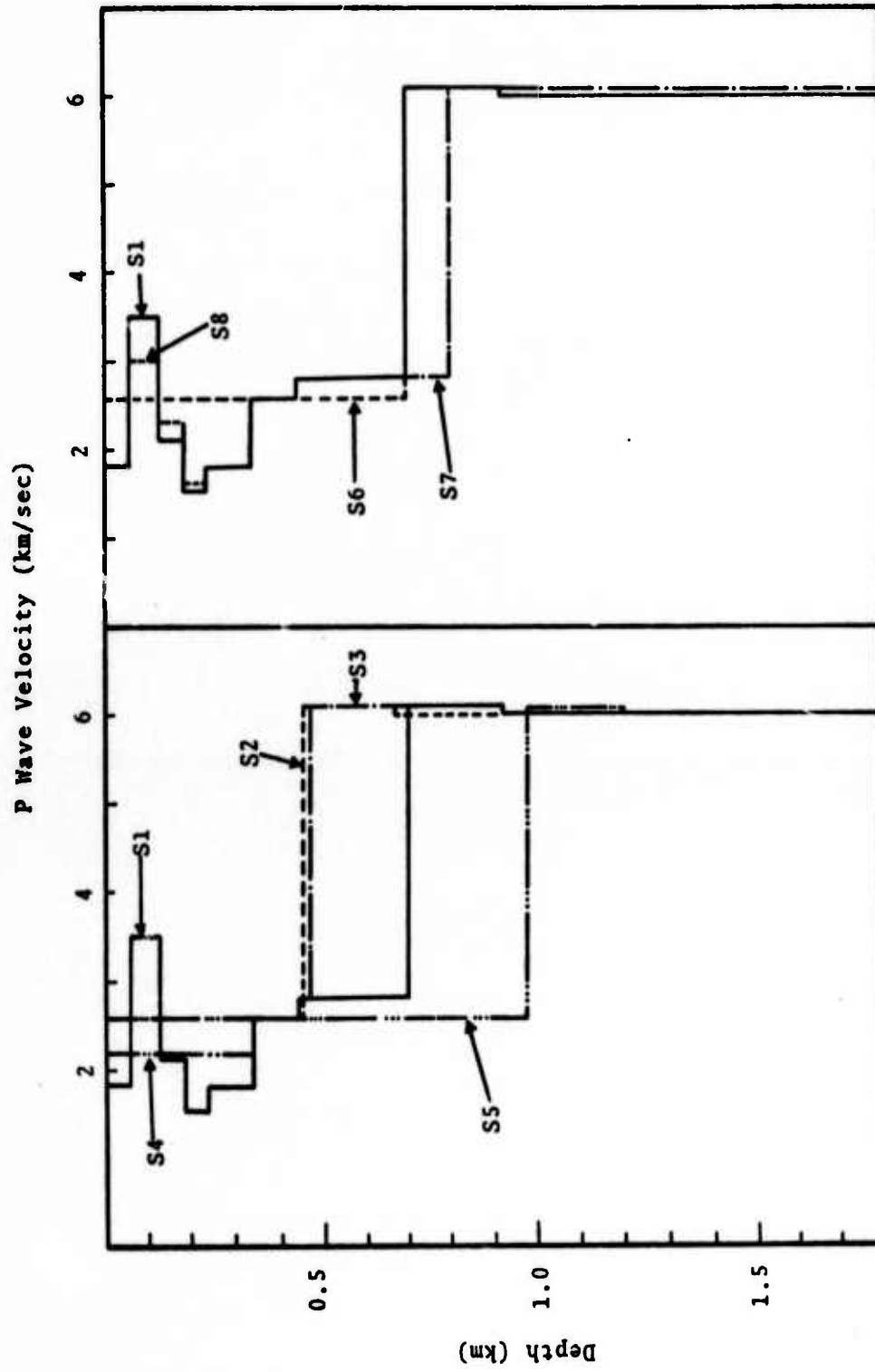
Two additional seismograms, computed using the source crustal structure S1, are shown in Figs. 2.5b and 2.5c. For these two seismograms a higher Q was introduced into the upper mantle model for the ray theory portion of the calculation resulting in $T/Q = 0.7$. The effect of the two instrument response functions, denoted #1 and #2, are seen by comparing Figs. 2.5b and 2.5c. Finally, in Fig. 2.5d the effect of an intermediate Q model, $T/Q = 0.84$, is demonstrated.

The seismograms of Fig. 2.5 were computed using a single model of the source crustal structure. This model, denoted S1 in Fig. 2.4, is characterized by a low velocity zone with a high velocity cap in the region between source and free surface. A few hundred meters below the source is a sharp velocity contrast at the Paleozoic rock which underlies the tuff. The remainder of the crustal structure down



a) Gross velocity profiles.

Figure 2.4. P wave velocity profiles for the source region crustal structure. If not otherwise indicated, each profile is identical to that for S1.



b) Detailed velocity profiles.

Figure 2.4 (Concluded)

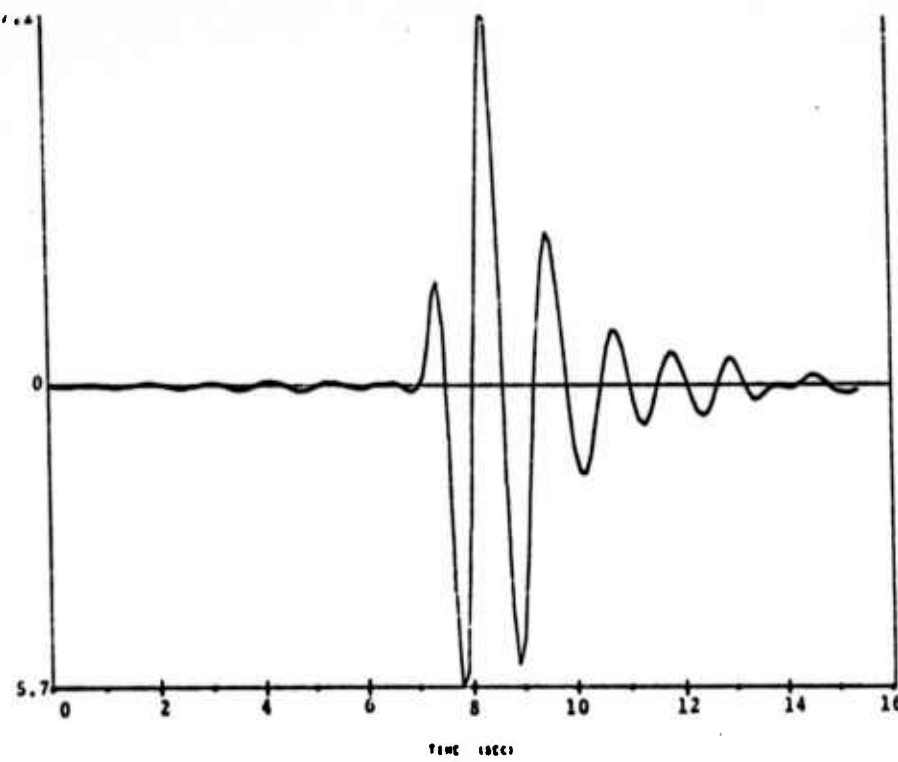
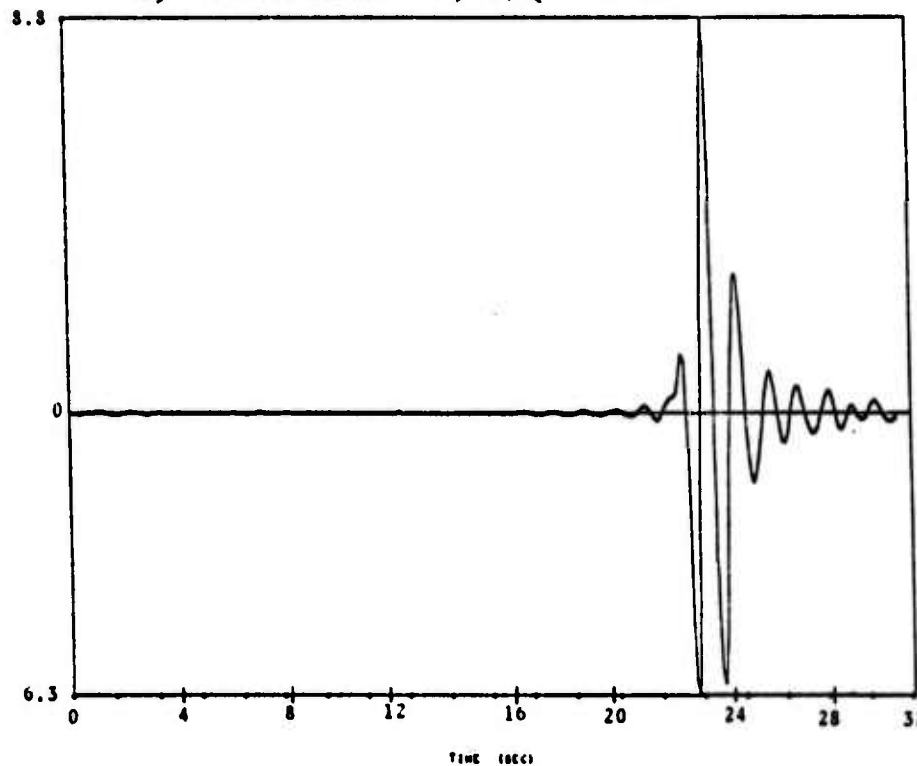
a) Instrument #2, $T/Q = 1.1$.b) Instrument #1, $T/Q = 0.7$.

Figure 2.5. Several synthetic seismograms for the 10 kT explosion recorded at ≈ 4000 km. The source crustal model S1 is included in the calculations which illustrate the effect of several Q models and two different instrument transfer functions.

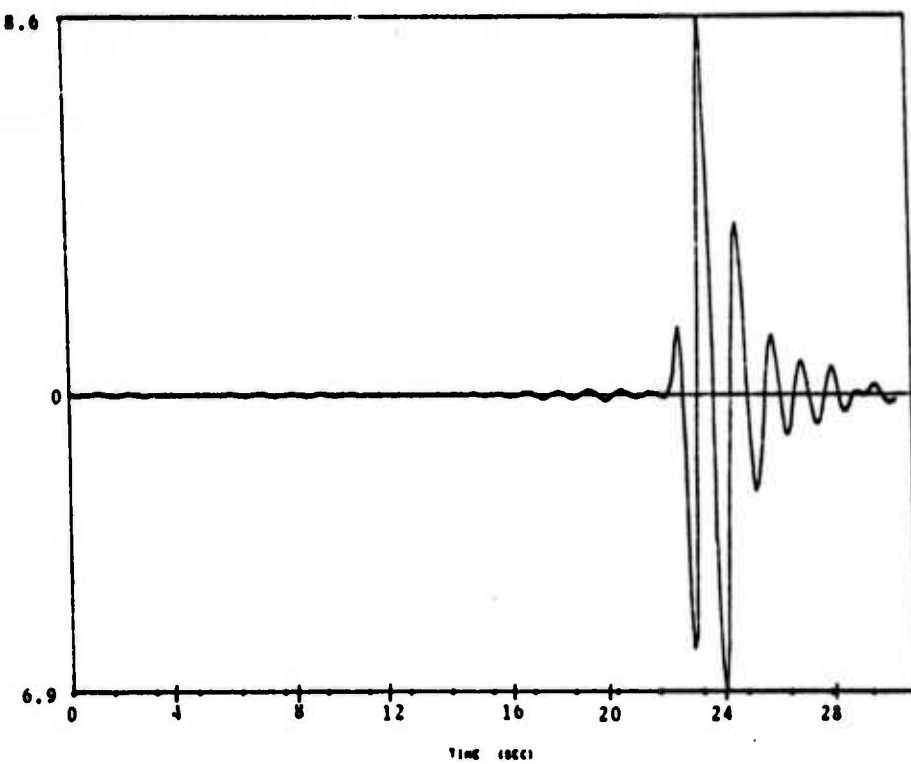
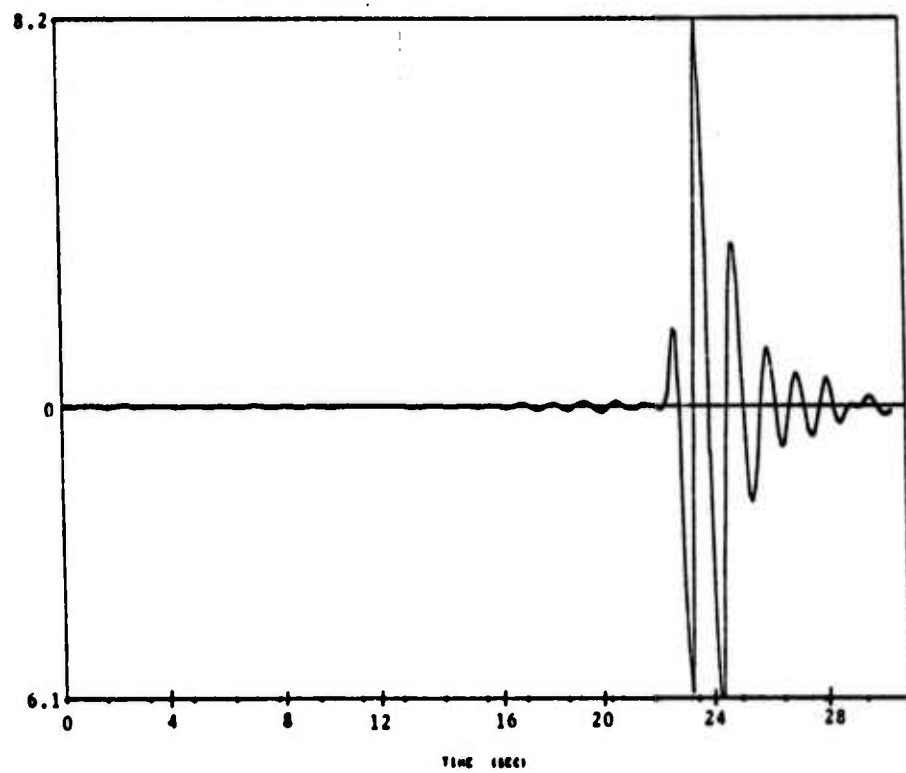
c) Instrument #2, $T/Q = 0.7$.d) Instrument #2, $T/Q = 0.84$.

Figure 2.5 (Concluded)

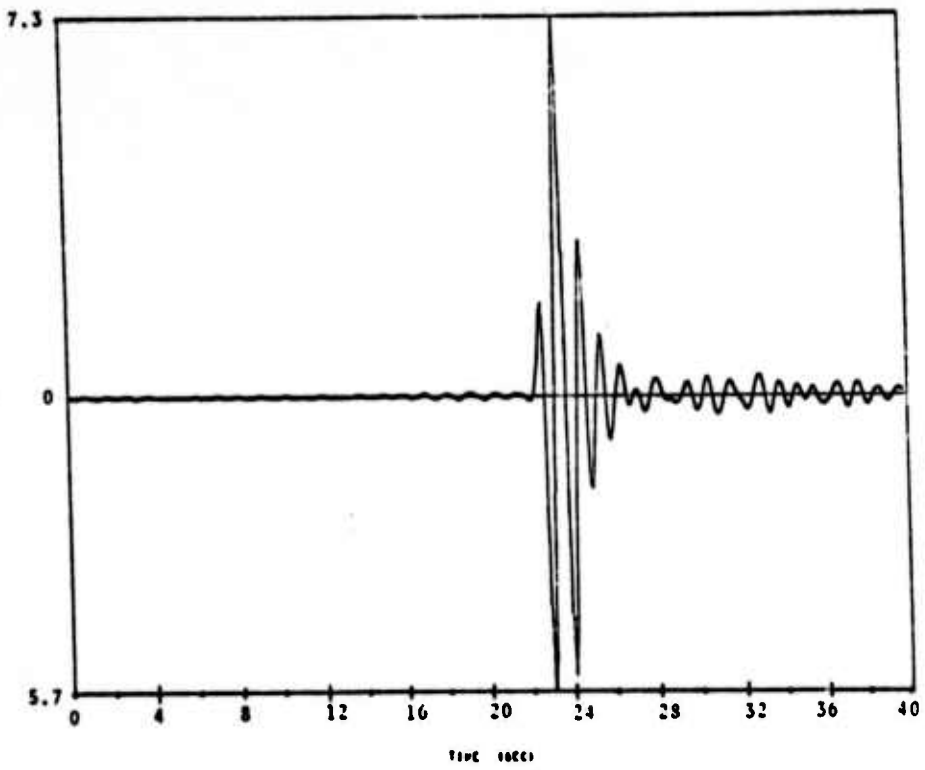
to the M discontinuity is taken from Hill and Pakiser.^[21] The effect of this crustal structure is to give the seismogram its commonly observed "W" shape and to spread its characteristic period.

The effect of variations in the uppermost part of the source crustal structure may be demonstrated by several examples. For the seismogram of Fig. 2.6a the crustal structure S2 was used, thus bringing the Paleozoic layer nearer the source. Comparing Figs. 2.6a and 2.5a, one observes that the Paleozoic depth primarily influences the amplitude of the first peak. A similar comparison is afforded by Figs. 2.6b and 2.5b, this time for a different instrument, with the main effect being a change in the relative amplitudes of the first and second troughs.

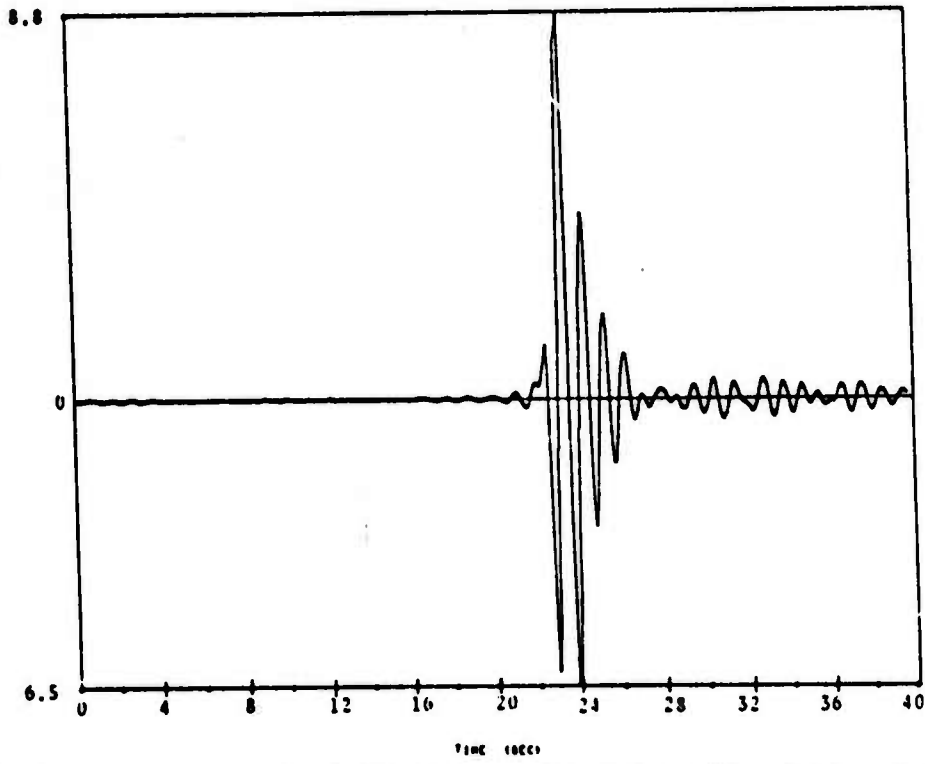
The effect of the layering above the source is portrayed in Fig. 2.7. The crustal model S4 gives an average velocity profile for the region above the source, smoothing the high and low velocity detail of models S1, S2, and S3. The model S5 uses average properties all the way down to the Paleozoic rock. Comparing Figs. 2.7a and 2.7b to 2.5a, it is clear that the first few swings of the seismogram are strongly influenced by the detailed structure in the source region.

The crustal model S6 is similar to S5 except that the M discontinuity is at a much shallower depth. The resulting seismogram is shown in Fig. 2.8a and should be compared to Figs. 2.5a and 2.7b. Finally, crustal model S7 has the M discontinuity essentially deleted. The effect on the pulse shape is shown in Fig. 2.8b.

It has been demonstrated that the near-source crustal structure can have a strong influence on the seismograph trace. The effect of a few typical receiver regional crustal

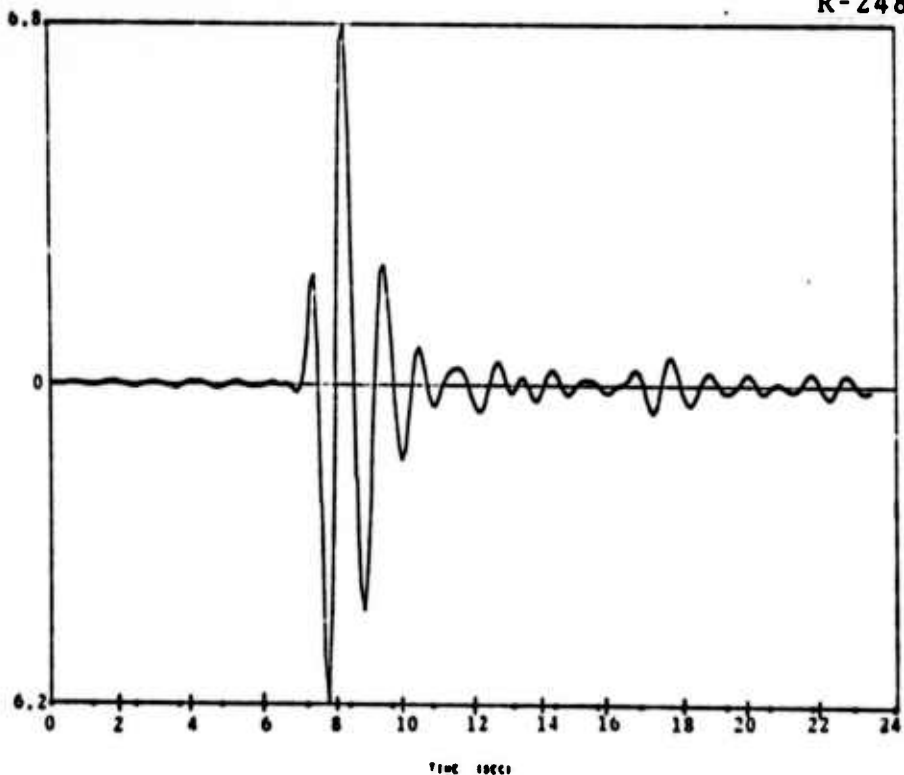


a) Source crustal model S2, Instrument #2, $T/Q = 1.1$.

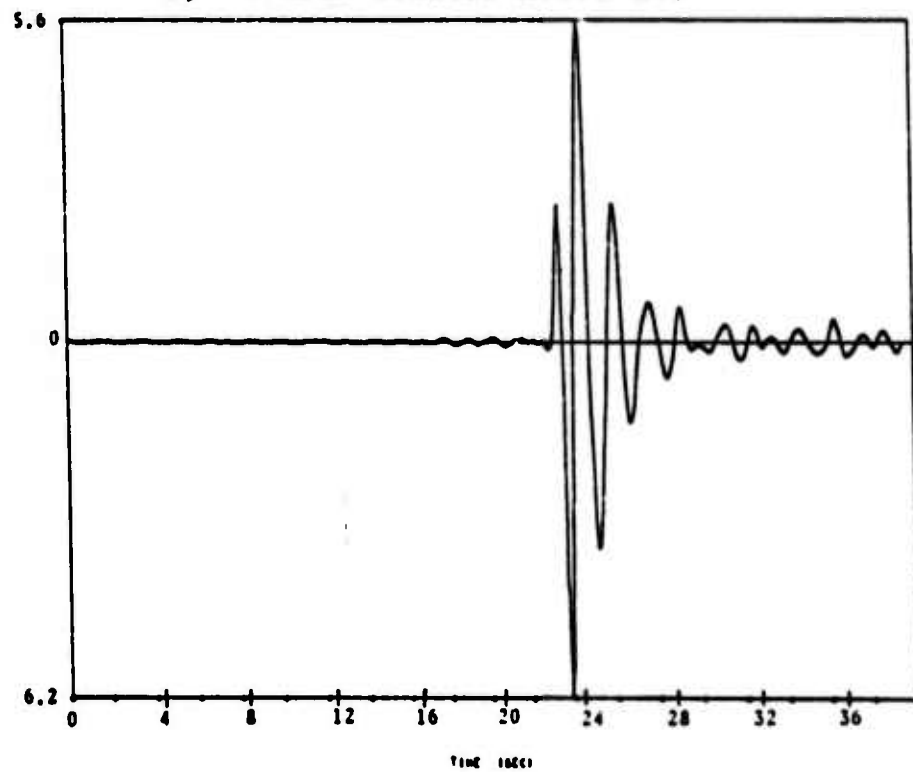


b) Source crustal model S3, Instrument #1, $T/Q = 0.7$.

Figure 2.6. The effect of a modified source crustal structure with the underlying Paleozoic rock at shallow depth.

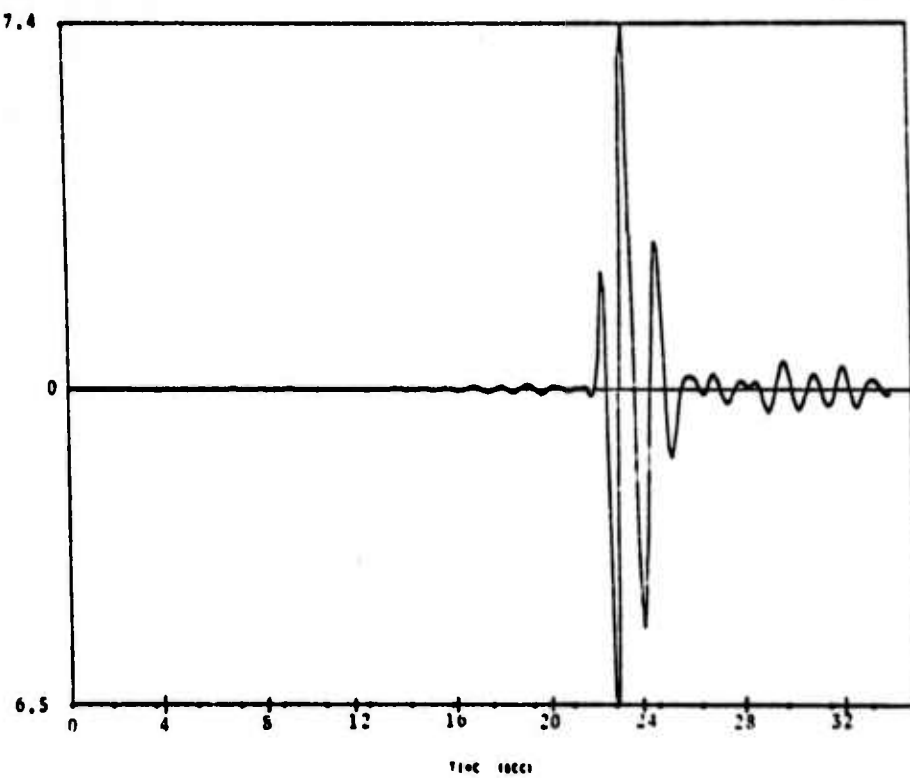


a) Source crustal model S4.

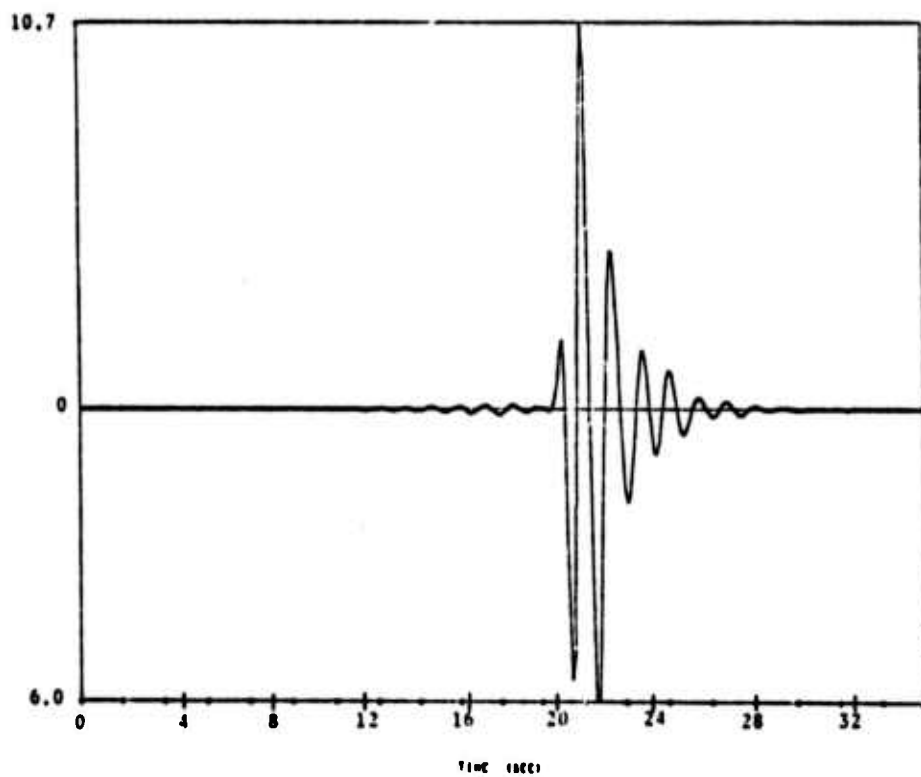


b) Source crustal model S5.

Figure 2.7. The effect of smoothing the velocity profile in the region between the source and the free surface. For both seismograms Instrument #2 was used and $T/Q = 1.1$.



a) Source crustal structure S6, T/Q = 1.1.



b) Source crustal structure S7, T/Q = 0.7.

Figure 2.8. Further examples of seismograms computed with modified crustal structures. Instrument #2 was used.

structures on the wave form will now be demonstrated. Velocity profiles for the receiver region crustal structures R1 and R2 are shown in Fig. 2.9. The only difference between the two is the properties of the top layer - one structure corresponds to an instrument on bedrock and the other to an instrument in the same area located on the sediments.

In Fig. 2.10a is shown the seismogram including the effects of both source structure S1 and receiver structure R1. This should be compared to Fig. 2.5a where only S1 was included. A new parameter is varied for Fig. 2.10b which was calculated with a different depth of burial. In Fig. 2.10c the structure models S3 and R1 are used (compare to Fig. 2.6b). Finally, in Fig. 2.11 three further examples of various combinations of source crustal structure models and the receiver model R2 are shown.

In Table 2.1 the important parameters used in the calculations leading to the seismograms presented in this section are summarized along with key measurements taken from the seismograms. The quantities A_1 , A_2 , A_3 , T , are defined in Fig. 2.11c.

Finally, a brief description of the distinguishing features of the various crustal models of this section (Figs. 2.4 and 2.9) is given in Table 2.2.

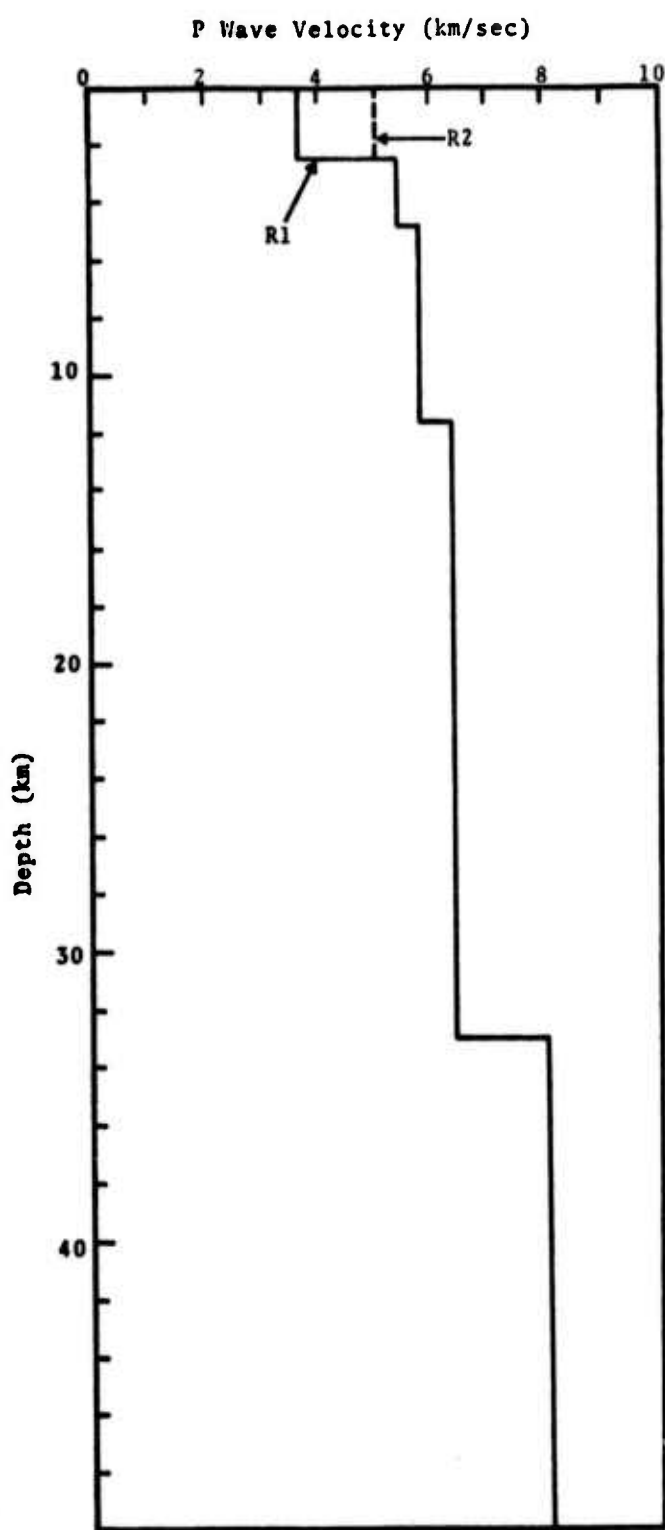
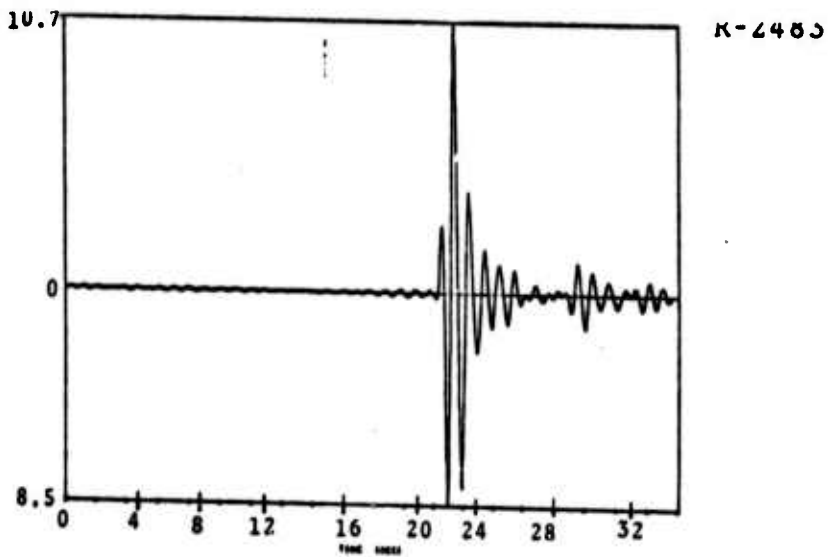
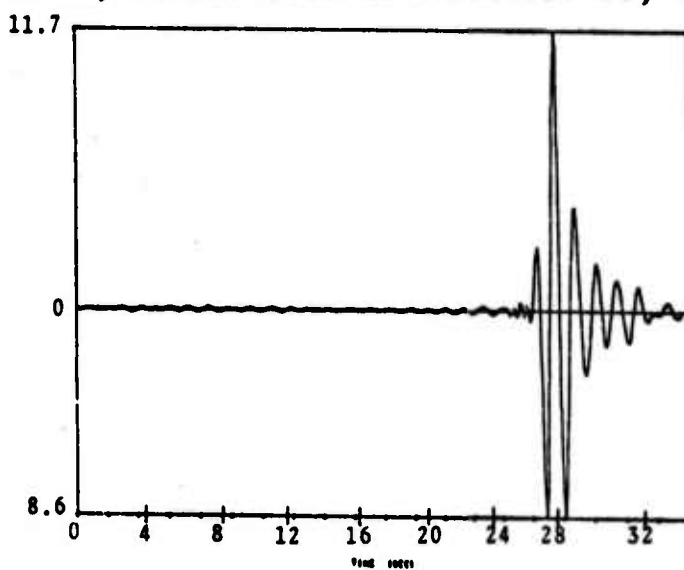


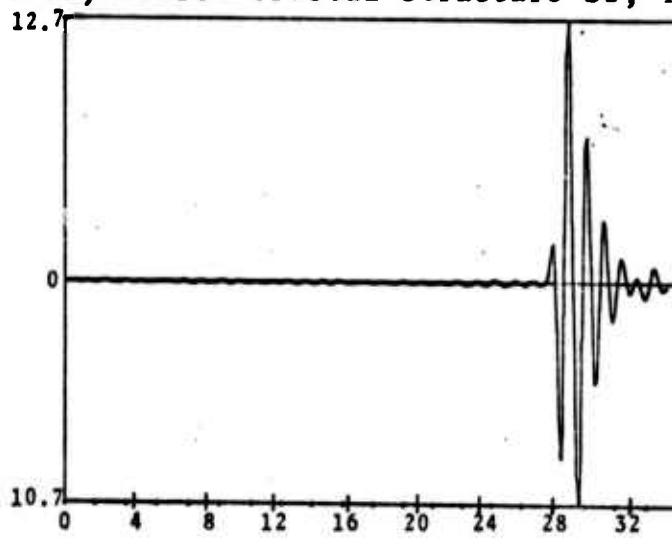
Figure 2.9. P wave velocity profiles for the crustal structure in the receiver region.



a) DOB = 0.4 km, Source crustal structure S1, T/Q = 1.1.

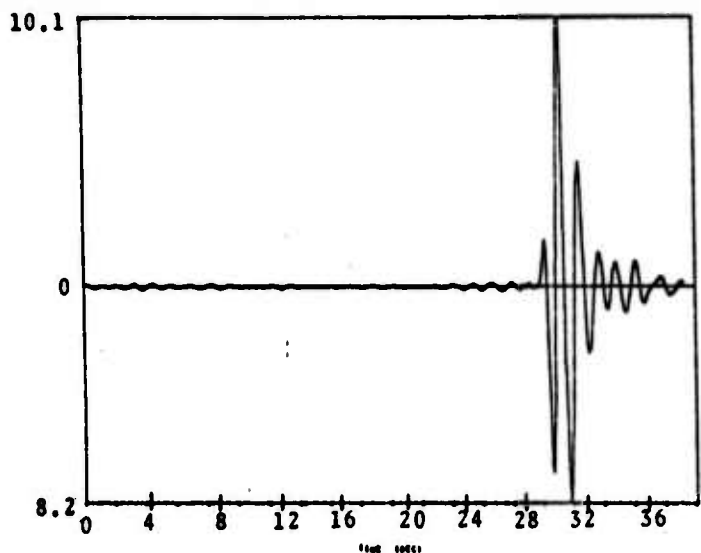


b) DOB = 0.5 km, Source crustal structure S2, T/Q = 1.1.

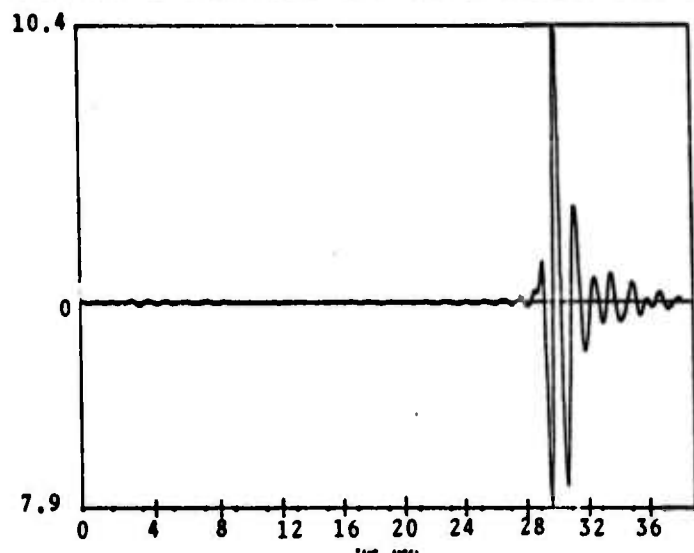


c) DOB = 0.4 km, Source crustal structure S3, T/Q = 0.7.

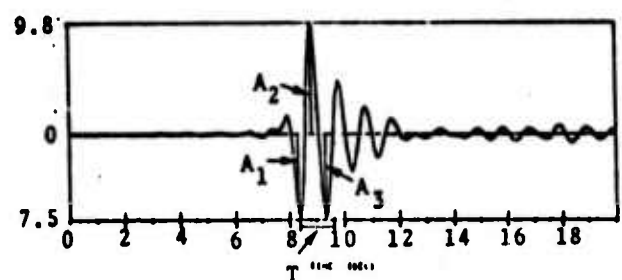
Figure 2.10. Synthetic seismograms including both the indicated source crustal structures and the receiver crustal structure R1. Instrument #2 was used.



a) Source crustal structure S1, Instrument #2, $T/Q = 0.7$.



b) Source crustal structure S8, Instrument #1, $T/Q = 0.7$.



c) Source crustal structure S3, Instrument #1, $T/Q = 0.84$.

Figure 2.11. Synthetic seismograms illustrating the effect of several source crustal structure models in combination with receiver crustal structure model R2.

TABLE 2.1
SUMMARY OF THE IMPORTANT PARAMETERS CHARACTERIZING
THE SEISMOGRAMS OF FIGURES 2.3 - 2.11

<u>Figure</u>	<u>DOB</u>	<u>Source Structure</u>	<u>Receiver Structure</u>	<u>Instr.</u>	<u>T/Q</u>	<u>A₁</u>	<u>A₂</u>	<u>A₃</u>	<u>T</u>
2.3	0.4	None	None	#1	1.1	7.7	5.7	0.55	1.30
2.5a	0.4	S1	None	#2	1.1	5.7	7.1	5.2	1.10
2.5b	0.4	S1	None	#1	0.7	6.3	8.8	6.1	1.02
2.5c	0.4	S1	None	#2	0.7	5.8	8.6	6.9	1.05
2.5d	0.4	S1	None	#2	0.84	6.0	8.2	6.1	1.05
2.6a	0.4	S2	None	#2	1.1	5.7	7.3	5.4	0.98
2.6b	0.4	S3	None	#1	0.7	6.2	8.8	6.5	0.95
2.7a	0.4	S4	None	#2	1.1	6.2	6.8	4.4	1.01
2.7b	0.5*	S5	None	#2	1.1	6.2	5.6	3.6	1.32
2.8a	0.5*	S6	None	#2	1.1	6.5	7.4	5.0	1.15
2.8b	0.4	S7	None	#2	0.7	7.5	10.7	8.0	1.05
2.10a	0.4	S1	R1	#2	1.1	8.5	10.7	7.5	1.05
2.10b	0.5	S1	R1	#2	1.1	8.6	11.7	8.6	1.10
2.10c	0.4	S3	R1	#2	0.7	8.5	12.7	10.7	0.97
2.11a	0.4	S1	R2	#2	0.7	7.0	10.1	8.2	1.05
2.11b	0.4	S8	R2	#1	0.7	7.9	10.4	7.0	0.97
2.11c	0.4	S3	R2	#1	0.84	7.5	9.8	7.3	0.95

* A depth of 0.5 km is required in source crustal structures S5 and S6 to maintain the source-surface travel time at a constant value for all seismograms of the table excepting 2.10b.

TABLE 2.2
SUMMARY OF THE MAJOR FEATURES OF THE CRUSTAL
MODELS S1 - S8 and R1 - R2

<u>Crustal Model</u>	<u>Important Features</u>
S1	Standard source crustal model with Paleozoic rock at 0.7 km and M discontinuity at 31 km
S2	Paleozoic rock at 0.45 km
S3	Paleozoic rock at 0.475 km
S4	Average properties in top 0.35 km
S5	Average properties in top 0.98 km
S6	Average properties in top 0.7 km, M discontinuity at 18.5 km
S7	M discontinuity not present
S8	S1 modified to reduce velocity contrast in top 0.5 km
R1	Standard receiver crustal model with sedimentary top layer
R2	R1 modified for bedrock top layer

III. DATA ACQUISITION, EDITING AND ANALYSIS

3.1 DATA ACQUISITION AND EDITING

During the first half-year of the contract period, considerable time was spent acquiring and editing numerous seismic data sets for North American and Eurasian earthquakes and explosions. These data form the basis for testing our waveform modeling capabilities, the applicability of newly proposed discriminants (e.g., see Section IV on Spectral Magnitude Discriminant) and the specification of a matched filter for improved event detection and identification.

At the present time our library of Eurasian events consists of 192 earthquakes and 42 presumed explosions recorded on digital magnetic tape. One hundred ninety of these event signatures are short-period recordings of best beam signals from the full LASA array while the remaining 44 events are best beam short-period signals from the original Oyer subarray at Norway. These data have been acquired through the cooperation of people at Lincoln Laboratory, in particular, Dr. Richard Lacoss.

Digital magnetic tape data, both short- and long-period, from the former LRSM stations, have been obtained from SDL for a number of NTS explosions. These data represent multi-station recordings of individual explosions and provide important information on different combinations of source-to-receiver path conditions. A request submitted to SDL for additional events is pending.

Each of the sets of digital data has required the development of an editing program for unpacking and verifying the data. As part of the editing procedure seismograms were plotted on a conventional time base for all of the above events and comprise a very important part of our event library.

In addition to the above digitally formatted data, copies of seismograms from selected high-gain long-period stations and from the World-Wide Network of Standard Seismograph Stations (WWNSS) have been obtained. These data provide both extended geographical coverage and a broader band look at event signals. Our plans are to continue expanding the data library to include a wide variety of event and receiver settings, so-called anomalous (M_s - m_b wise) earthquakes, and intraplate earthquakes.

3.2 DATA ANALYSIS

In addition to the extensive code capability for modeling seismic phenomena developed at S³ and described in Section II of this report, two codes were recently brought on-line for analysis of the digitally formatted seismic data. The two new codes, which have been used extensively for application of the spectral magnitude discriminant, are DATCON and MAGIC. DATCON accepts seismic data in digital format and has options to detrend, taper, demean and band-pass filter the data.

MAGIC, a MAGnitude Identification Code, also accepts seismograms of body and/or surface waves in digitized form. The seismograms may be real data or synthetic seismograms generated by source codes in the S³ library. Several events (explosions) may be added together with some desired spacing in distance and time to give a multiple event scenario. The single or multiple event seismograms may then be plotted.

A series of narrow band filters with center frequencies, f, and quality factors, Q, may be specified for recursively filtering the seismograms. The maximum output amplitude of the resulting filtered seismogram is then picked as the amplitude associated with the energy at the center frequency of the filter. Various magnitude definitions may then

be applied and standard Gutenberg-Richter distance corrections are included in the code. The code generates spectral magnitudes at several different frequencies, $\bar{m}_b(f)$, over time windows of varying duration. Plots of $\bar{m}_b(f_1)$ versus $\bar{m}_b(f_2)$, $f_1 < f_2$, can then be tested for event discrimination. In addition the code can determine M_s^R and M_s^L , where M_s^R is the spectral surface wave magnitude for Rayleigh waves at 20 second period and M_s^L is the same magnitude for Love waves, and test for event discrimination using \bar{m}_b versus M_s^R and M_s^L . An application of the codes DATCON and MAGIC to a large population of Eurasian events is described in the next section of this report.

IV. SPECTRAL MAGNITUDE DISCRIMINANT

4.1 TECHNIQUE

A variable frequency magnitude discriminant^[7] employing spectral magnitudes \bar{m}_b computed from short-period compressional waves is presently being tested using a large population of Eurasian earthquakes and underground explosions recorded at LASA^[22] and the original Oyer subarray at Norway. The Norway results are still preliminary and will be discussed in a later report.

This discriminant is designed to exploit spectral differences between earthquakes and explosions. Essentially, it consists of a comparison of a spectral magnitude measurement $\bar{m}_b(f_1)$ at a relatively low frequency (e.g., $f_1 = 0.4$ Hz) to a measurement $\bar{m}_b(f_2)$ at a relatively high frequency (e.g., $f_2 = 2.5$ Hz). The spectral body wave magnitude \bar{m}_b is defined as the log of the amplitude of the output of a very narrow band, phaseless filter (high Q filter), centered at frequency f_g , plus a distance correction factor $\bar{\sigma}$. That is,

$$\bar{m}_b = \log_{10} (A_g/T_g) + \bar{\sigma},$$

where the center period $T_g = 1/f_g$ and A_g denotes the amplitude of the filter output. A particularly desirable feature of this type of discriminant is that its application depends solely on the recording of compressive waves from earthquakes and explosions. By obviating the requirement for the recording of surface waves, the spectral magnitude technique should be applicable to smaller magnitude events than the conventional $m_b - M_s$ discriminant.

4.2 EVENTS RECORDED AT LASA

The event population employed in the first test of the spectral magnitude discriminant consists of 34 presumed underground explosions and 156 earthquakes recorded at LASA. Most of these events occurred in, or very close to, the USSR or China, at epicentral distances of 60° to 100° from LASA. It is important to note that only about 55 percent of the earthquakes in this data base were reported in the Monthly Listings of events published by the USCGS. Thus, 45 percent of the earthquakes in this data base are of either unknown or poorly determined focal depth.

Figures 4.1 and 4.2 are plots of spectral magnitudes at several different frequencies (low frequency \bar{m}_b versus high frequency \bar{m}_b) for all 34 explosions (closed circles) and the shallow earthquakes (open circles) in the data base. Figure 4.1 clearly demonstrates the general enrichment of the high frequency portion of the explosion body wave spectra relative to the earthquake spectra over the entire magnitude range of the data. For instance, for a given value of \bar{m}_b (0.5 Hz) the explosions exhibit \bar{m}_b (2.0 Hz) values that are typically 0.6 to 0.9 units larger than the earthquake \bar{m}_b (2.0 Hz) values. In particular, note that this separation, or discrimination, of earthquakes and explosions holds over the entire magnitude range with no indication of convergence of the two populations at small magnitudes.

Comparison of Figs. 4.1 and 4.2 shows the dependence of the spectral magnitude discriminant on parameters such as background noise, instrument response, and the frequency separation of the magnitude determinations. First note the intermingling of event populations in Fig. 4.2 at small magnitudes, while as indicated in Fig. 4.1 only one small magnitude (LASA $m_b = 3.9$) explosion lies in the earthquake population.

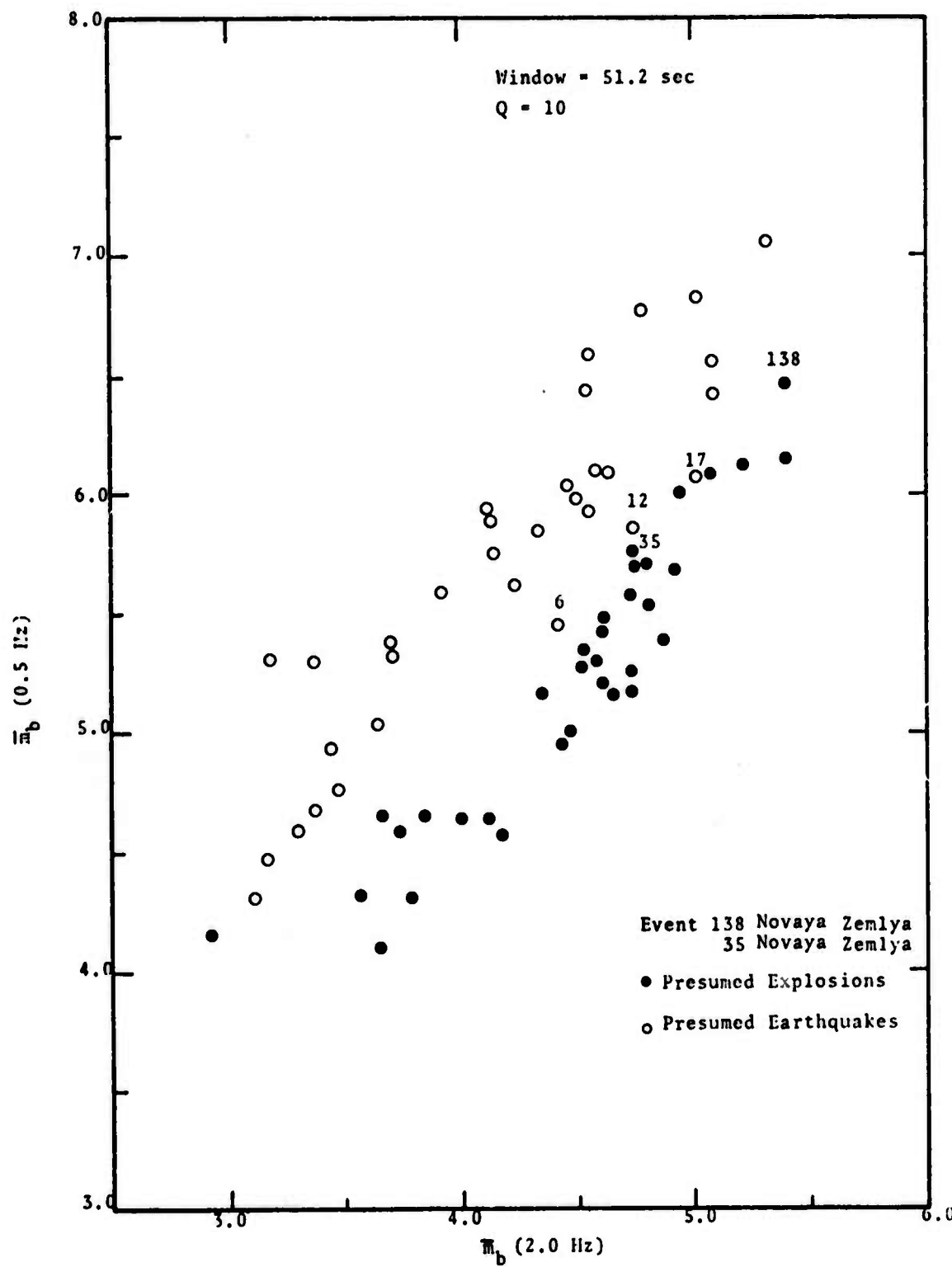


Figure 4.1. Spectral magnitude estimates at 0.5 Hz and 2.0 Hz for Eurasian earthquakes and explosions. Note that the presumed explosions numbered 35 and 138 occurred at Novaya Zemlya.

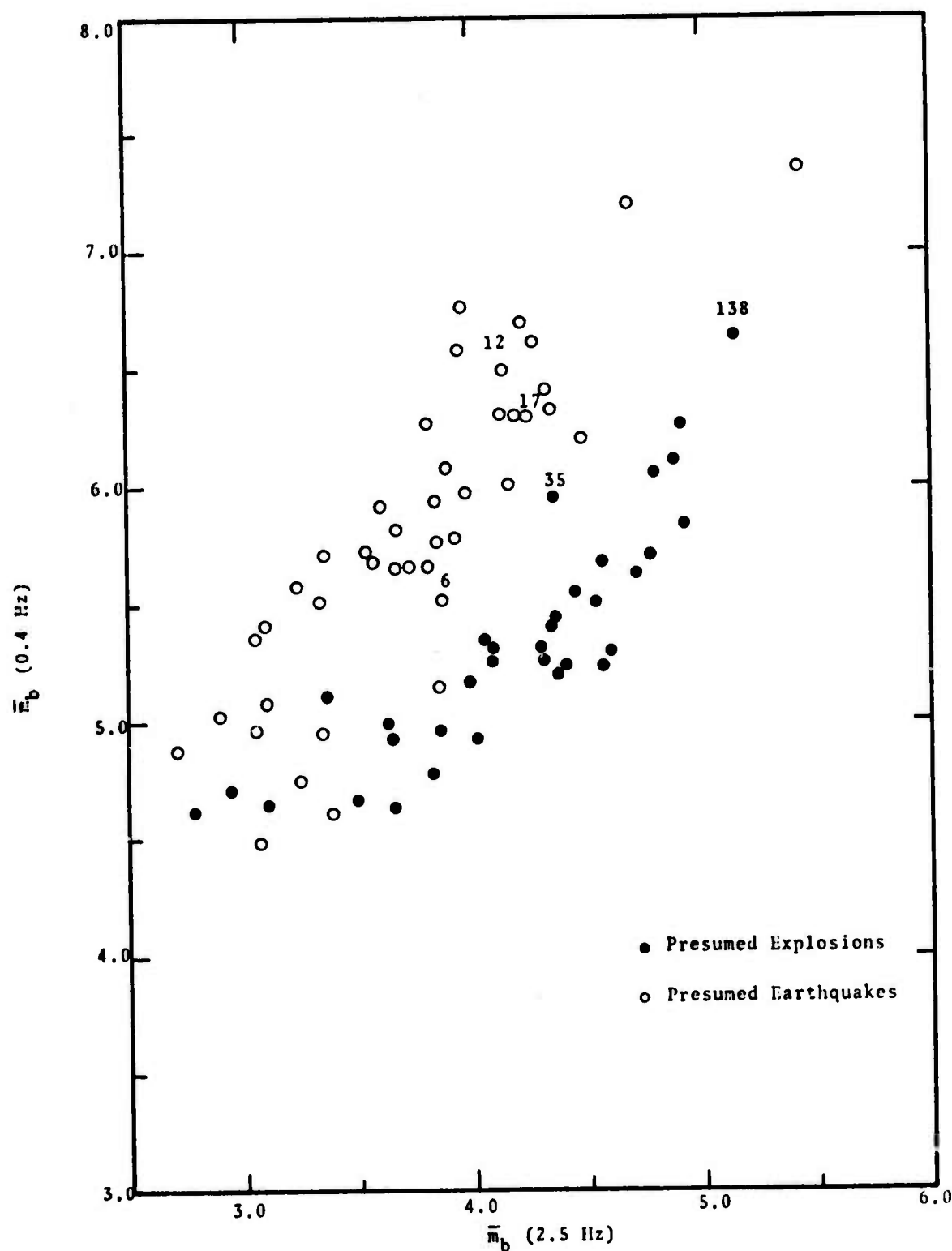


Figure 4.2. Spectral magnitude estimates at 0.4 Hz and 2.5 Hz for the same population of events plotted in Fig. 4.1.

Seismograms for this explosion (Fig. 4.3) and for two other explosions with \bar{m}_b (0.5 Hz) values < 4.5 clearly demonstrate that the very low signal-to-noise ratio (S/N) is the reason for the failure to discriminate this event. Comparison of the seismogram of the small $m_b = 3.9$ explosion (Fig. 4.3) with the seismogram for a larger magnitude ($m_b = 5.8$) and, therefore, better recorded explosion in terms of S/N (Fig. 4.4), indicates that the spectral magnitude determinations based on the small explosion time series are essentially measurements of the noise background, in particular noise in the 0.4 to 0.5 Hz range.

The fact that many of the small magnitude events that fail to discriminate in Fig. 4.2 discriminate well in Fig. 4.1 is a result of narrowing the frequency spread of the magnitude estimates to better coincide with the amplitude response characteristics of the LASA instrumentation and the spectral behavior of the prevailing background noise. This interpretation is supported by the enhanced discrimination of larger magnitude events in Fig. 4.2 compared to Fig. 4.1, in particular for earthquakes 6, 12 and 17. In this case S/N is high over a wider frequency range and the spectral magnitudes computed at the more widely separated frequencies yield the enhanced discrimination observed in Fig. 4.2.

It has been pointed out^[7] that maximum discrimination of event populations are expected for spectral magnitudes $\bar{m}_b(f)$ computed at frequencies of maximum separation. The actual frequencies will depend upon microseismic noise spectra and detector site characteristics. In addition, in order to avoid the effects of spectral maxima and minima that occur for both earthquakes and explosions, it is probably necessary to use combinations of spectral magnitudes at several different frequencies.

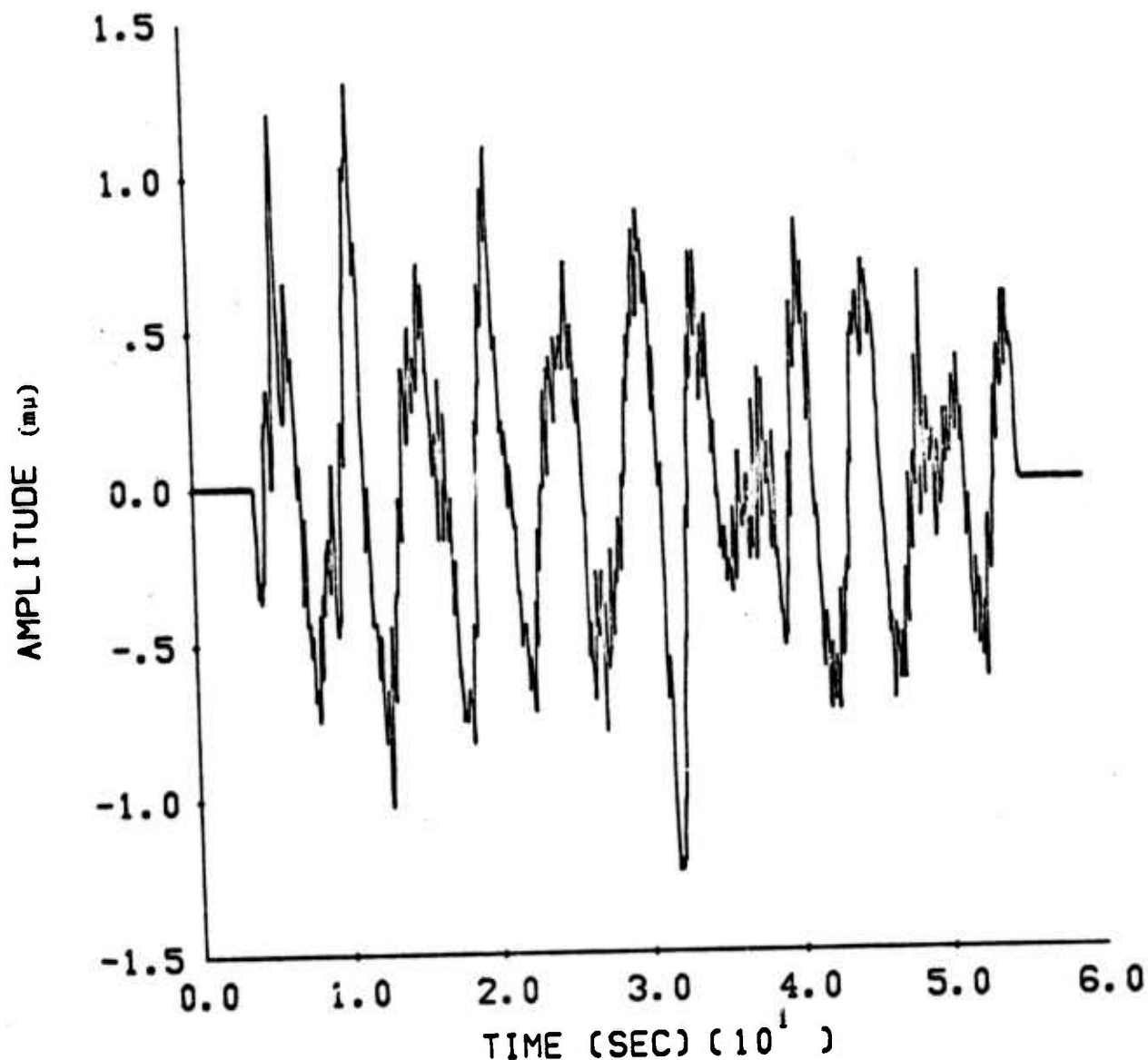


Figure 4.3. Seismogram of reported m_b (LASA) = 3.9 presumed explosion.

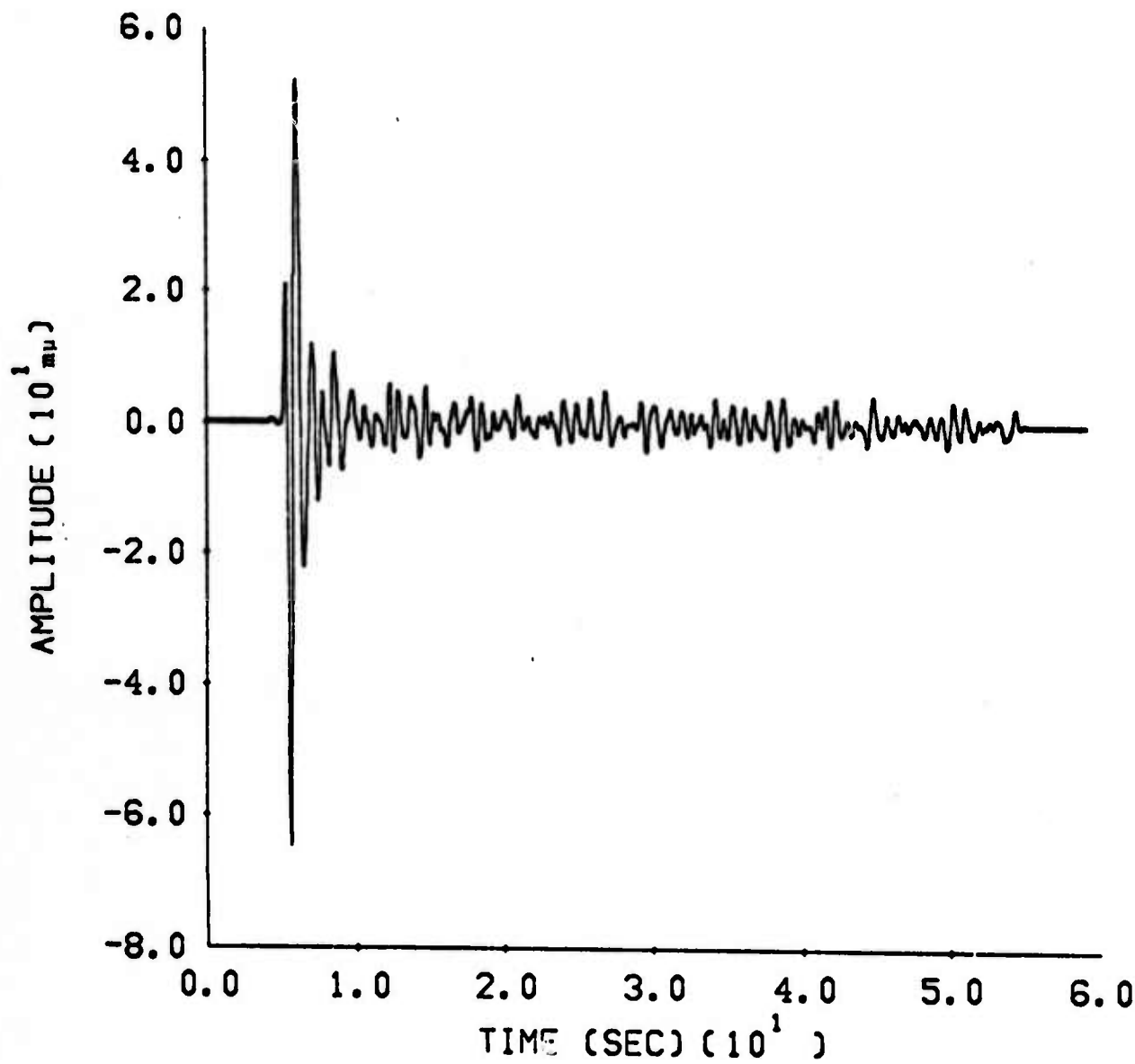


Figure 4.4. Seismogram of m_b (LASA) = 5.8 presumed explosion.

4.3 MULTIPLE EVENTS

The variable frequency magnitude discriminant is especially suited for discrimination of multiple explosion sequences (Figs. 4.5 and 4.6) that are designed to appear earthquake-like in terms of conventional (m_b - M_s , depth of focus, first motion) discriminants. A multiple event scenario, similar to one previously proposed,^[23] was devised by superposing eight seismograms of a presumed explosion in Eastern Kazakhstan recorded at LASA. The actual explosion signature used in this scenario is shown in Fig. 4.4. The array of explosions and their relative yields were designed to produce an earthquake-like seismogram over at least some range of azimuth. The particular array configuration (spacing and firing order) is indicated in the lower right hand corner of Fig. 4.5. Each seismogram comprising the multiple event was delayed in time relative to the first, and scaled in amplitude to correspond to an explosion of the indicated yield.

Spectral magnitude estimates of the multiple event (closed triangles) are plotted in Figs. 4.5 and 4.6 together with the event populations previously plotted in Figs. 4.1 and 4.2, respectively. The numbers 1-5 indicate the different azimuths to the recording sites shown in Fig. 4.5. Note that the legend is not drawn to scale as the shot spacing is 1 km and the recording sites are at teleseismic distances ($\sim 83^\circ$).

The multiple event sequence was especially designed to appear earthquake-like at stations broadside to the shot array. In particular, the composite seismogram (Fig. 4.7) at these azimuths exhibits an apparent rarefaction for the first prominent motion. It should be noted that the P-wave train in Fig. 4.7 is not preceded by background noise. If

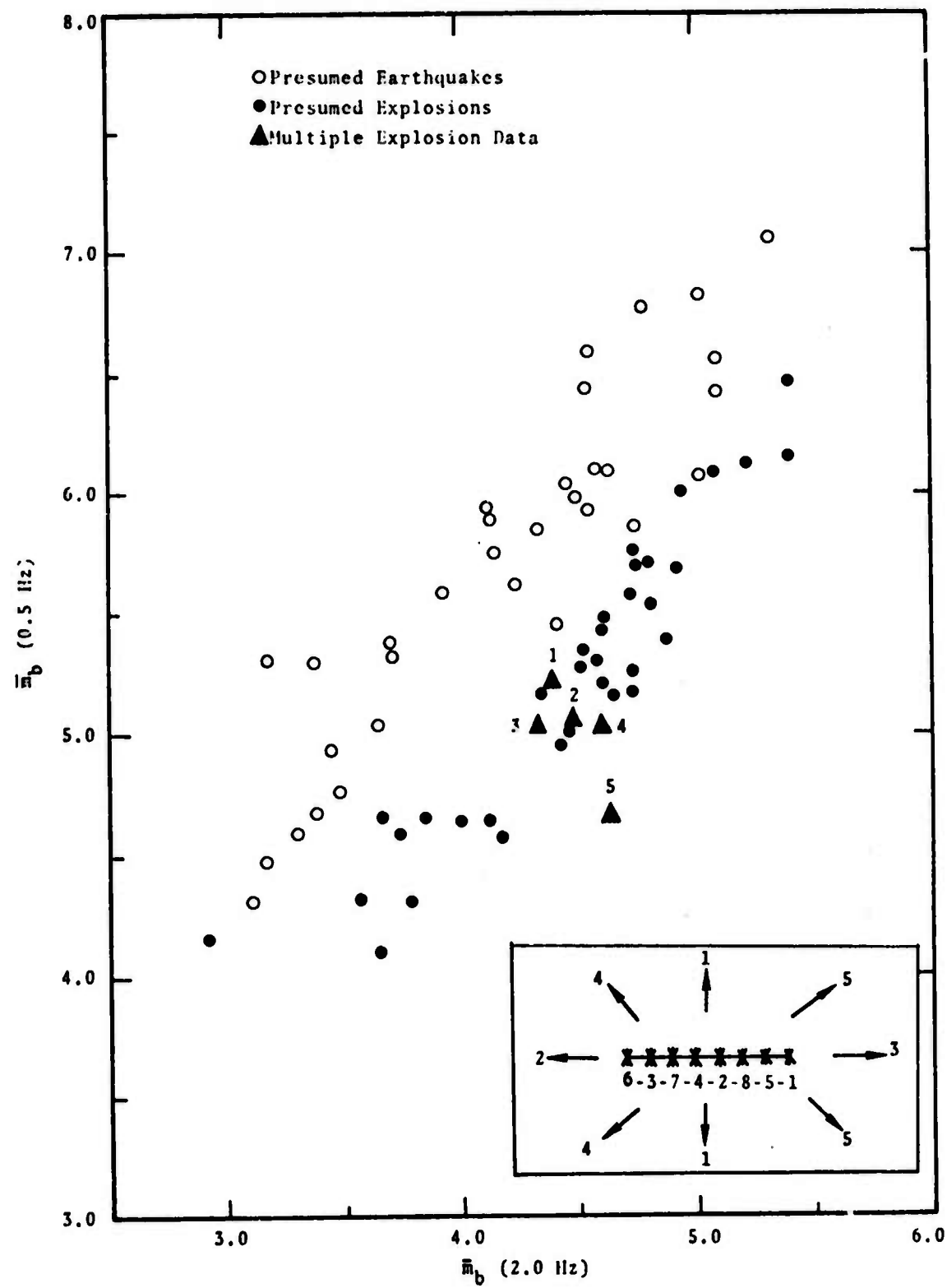


Figure 4.5. Spectral magnitude estimates for the multiple event sequence and the Eurasian event population plotted in Fig. 4.1. The individual shots in the array are evenly spaced and, in the computations, were taken to be 1 km apart. The shot yields are: 1 at 4 kT; 2 at 12 kT; 3, 4 and 5 at 31 kT; 6, 7 and 8 at 100 kT, corresponding to amplitude scaling of 1, 3, 7.8, 7.8, 7.8, 25, 25 and 25.

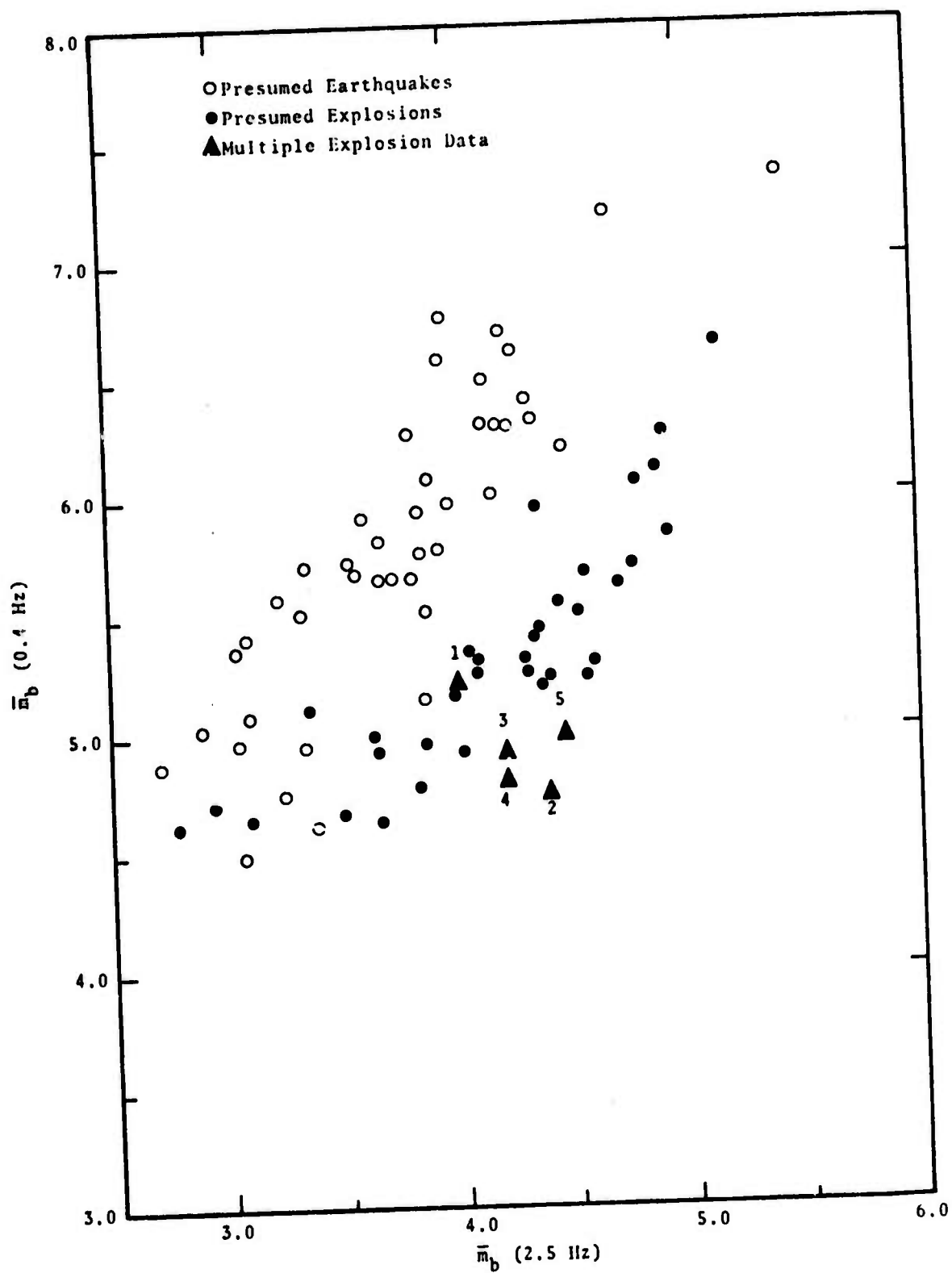


Figure 4.6. Spectral magnitude estimates for the multiple event sequence and the Eurasian event population plotted in Fig. 4.2.

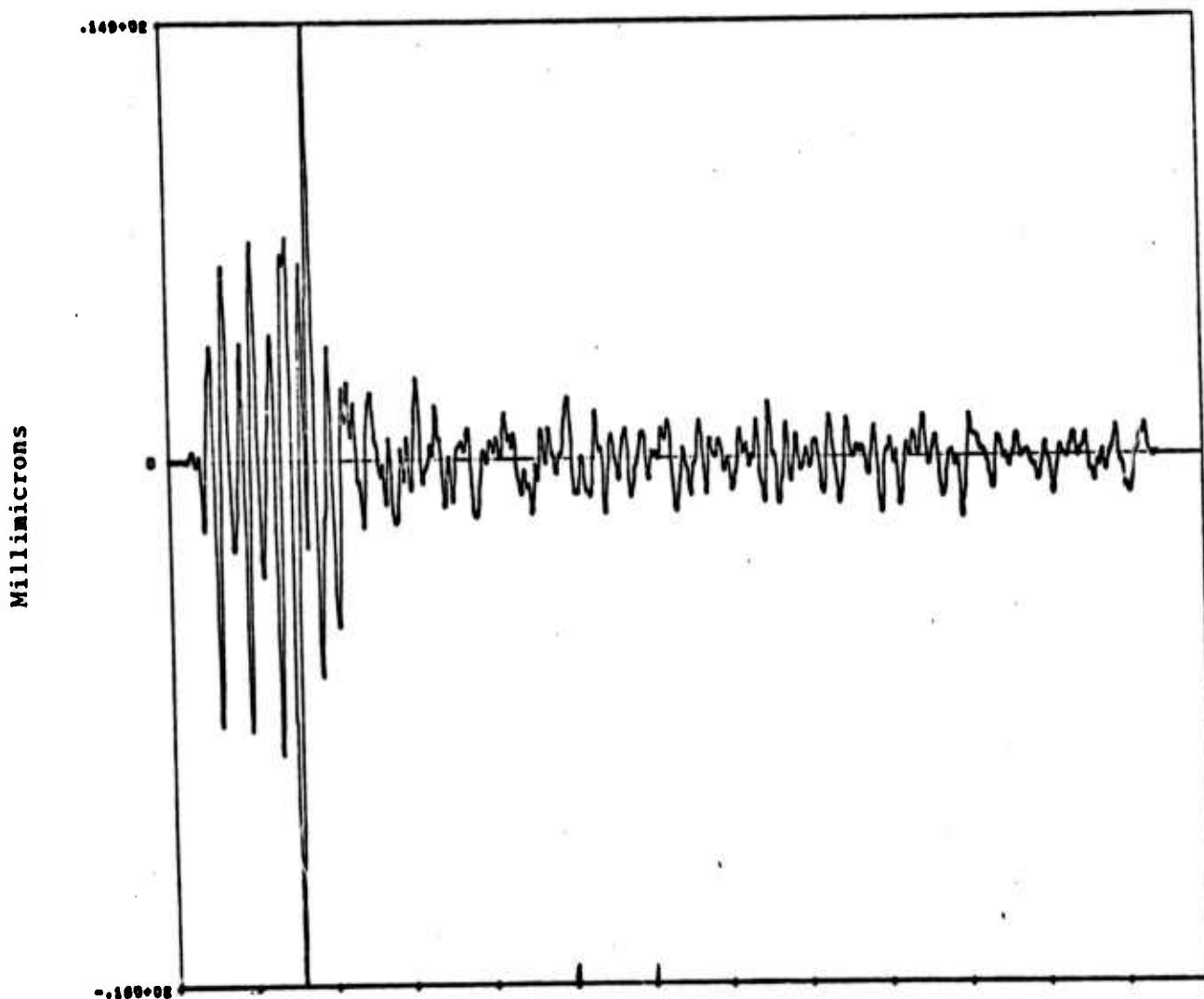


Figure 4.7. Composite seismogram of the multiple explosion scenario described in Fig. 4.5.

it were, the very small excursion starting at about 1 second would most likely be obscured resulting in the larger rarefaction at about 1.7 second being identified as the first motion. The composite seismogram would undoubtedly lead an analyst to measure amplitudes for m_b based on one of the earlier explosions of smaller yield while measuring amplitudes for M_s that would be the superposition of the three high yield explosions. The net effect of these measurements would be to increase M_s relative to m_b making the multiple event approach or lie within the earthquake population on an $m_b - M_s$ plot. The spectral magnitude technique, on the other hand, by basing an \bar{m}_b measurement on the largest amplitude arrival at some frequency f in the wavetrain, exhibits pronounced discrimination (Figs. 4.5 and 4.6) of the multiple event at all azimuths.

The composite seismogram in Fig. 4.7 is dominated by the three largest explosions occurring toward the end of the proposed event scenario. In order to simulate a more earthquake-like seismogram a second multiple explosion scenario was devised. Once again, the presumed explosion signature shown in Fig. 4.4 was used as the primary signal. Most of the shot array characteristics (spatial separation, firing order, and time delays) were identical to the previous experiment, the major difference being in the amplitude (yield) ratios of successive explosions. In this second multiple explosion experiment the amplitude ratios were 1, 3.1, 5, 10, 10, 20, 15 and 12.5. The primary intent of this choice of scaling factors was to simulate more emergent composite seismograms devoid of suspicious prominent arrivals. The time delays and scaling were still such that M_s for the multiple event would be enhanced relative to m_b .

The resulting composite seismograms are shown in Fig. 4.8 at five different azimuths with respect to the shot array. The first point to be noted is that with the addition of noise to the beginning of each seismogram the first motions at azimuths 1, 3 and 5 would most probably be picked as rarefactions. Secondly, the complexity of each composite signal has been greatly increased over that of the primary signal shown in Fig. 4.4. An analyst making amplitude measurements, to be used for m_b determinations in the conventional manner (maximum amplitude within the first 3 or 4 cycles), would undoubtedly pick amplitudes corresponding to the earlier smaller explosions in the sequence. This is equivalent to a further enhancement of M_s and results in an event that appears to be an earthquake on an $M_s - m_b$ basis. However, when subjected to the spectral magnitude technique the five composite signals shown in Fig. 4.8 were found to discriminate in exactly the same manner as the previous scenario (Figs. 4.5 and 4.6).

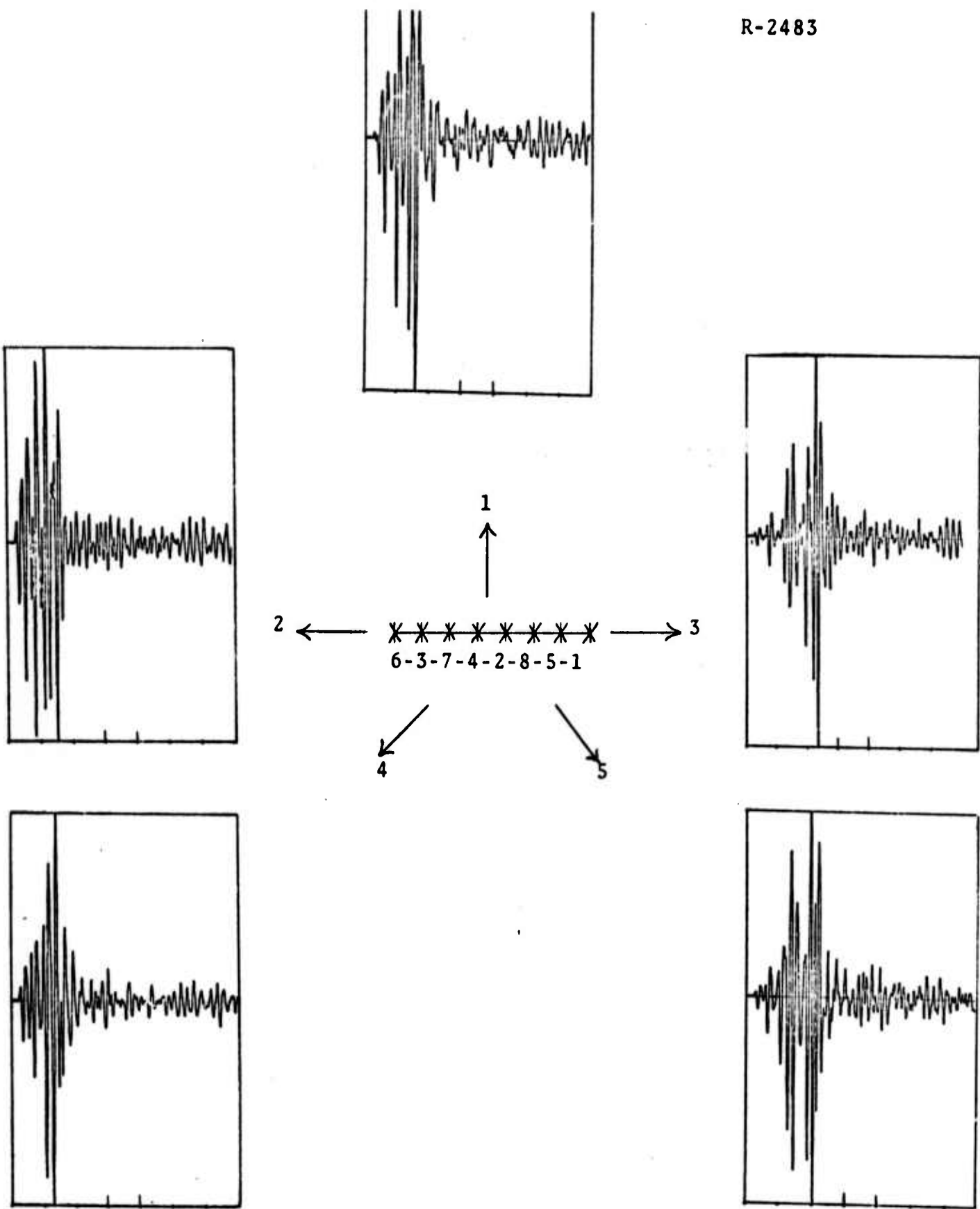


Figure 4.8. Composite seismograms written at five different azimuths for the revised multiple event scenario. Approximately 30 seconds of signal is shown in each case; the two enlarged tick marks along each abscissus represent a time increment of 4.6 seconds. The maximum O-P amplitudes of each signal are about 50 m μ .

V. CONCLUDING REMARKS

Most of the important conclusions concerning the variation of teleseismic magnitude with the various contributing parameters are set forth in Appendix A and will not be repeated here. However, recent work has revealed the important role that crustal reverberations may play in shaping the P wavetrain. For many, though not all, source regions and receiver stations, these effects should be included in the calculations.

The collection and playing out of seismic data from a variety of sources has been a not inconsiderable task accomplished during the first portion of the contract period. Due to magnetic tape I/O incompatibilities between various computer systems, the initial interaction with a data source is often difficult. However, this interaction is now routine with most important data repositories.

The spectral magnitude discriminant suggested by Archambeau has been extensively tested using Eurasian earthquakes and presumed explosions and appears to offer a distinct improvement over previously suggested discrimination techniques (e.g., $m_b - M_s$).

REFERENCES

1. Cherry, J. T., T. C. Bache, C. B. Archambeau and D. G. Harkrider, "A Deterministic Approach to the Prediction of Teleseismic Ground Motion from Nuclear Explosions," Systems, Science and Software Final Contract Report, DNA 2231F, June 1974.
2. Cherry, J. T., T. C. Bache, and D. F. Patch, "The Teleseismic Ground Motion Generated by a Nuclear Explosion Detonated in a Tunnel and Its Effects on the M_s/m_b Discriminant," Systems, Science and Software Final Contract Report (Draft), SSS-R-74-2124, April 1974.
3. Cherry, J. T., T. C. Bache, and C. B. Archambeau, "A Suggested Procedure for Predicting Body Wave Magnitude from an Underground Nuclear Explosion," Systems, Science and Software Topical Report, prepared for DNA, SSS-R-74-2280, June 1974.
4. Cherry, J. T., T. C. Bache, C. B. Archambeau, and J. M. Savino, "Explosion Yield Estimates Based on Seismic Magnitude Observations: Dependence of Magnitudes on Yield, Near Source Materials Properties, Depth of Burial and Earth Structure," Systems, Science and Software Topical Report, prepared for ARPA, SSS-R-74-2400, August 1974.
5. Archambeau, C. B., "The Theory of Stress Wave Radiation from Explosions in Prestressed Media," Geophys. J. Roy. Astr. Soc., 29, p. 329, 1972.
6. Minster, J. B., "Elastodynamics of Failure in a Continuum," Ph.D. Thesis, California Institute of Technology, 1973.
7. Archambeau, C. B., D. G. Harkrider, and D. V. Helmberger, "Studies of Multiple Seismic Events," California Institute of Technology Final Contract Report (Draft) prepared for U. S. Arms Control and Disarmament Agency, August 1974.
8. Cherry, J. T., "Calculations of Near Field Earthquake Ground Motion," Annual Technical Report prepared for ARPA, SSS-R-73-1759, June 1973.
9. Harkrider, D. G., "Surface Waves in Multilayered Elastic Media. I. Rayleigh and Love Waves from Sources in a Multilayered Half-Space," BSSA, 54, p. 627, 1964.

10. Morse, P. M., and H. Feshbach, Methods of Theoretical Physics, Vol. II, McGraw-Hill, 1953.
11. Archambeau, C. B., "General Theory of Elastodynamic Source Fields," Rev. of Geophysics, 6, p. 241, 1968.
12. Strick, E., "A Predicted Pedestal Effect for Pulse Propagation in Constant-Q Solids," Geophysics, 35, p. 487, 1970.
13. Haskell, N. A., "Crustal Reflection of Plane P and SV Waves," J. Geophysical Res., 67, p. 4751, 1962.
14. Fuchs, K., "The Transfer Function for P Waves for a System Consisting of a Point Source in a Layered Medium," BSSA, 56, p. 75, 1966.
15. Harkrider, D. G., and C. B. Archambeau, "Theoretical Rayleigh and Love Waves from an Explosion in Pre-stressed Source Regions," to be submitted for publication.
16. Hasegawa, H. S., "Crustal Transfer Ratios of Short- and Long-Period Body Waves Recorded at Yellowknife," BSSA, 61, p. 1303, 1971.
17. Biot, M. A., "General Theorems on the Equivalence of Group Velocity and Energy Transport," The Physical Review, 105, pp. 1129-1137, 1956.
18. McGarr, A., "Amplitude Variations of Rayleigh Waves--Propagation Across a Continental Margin," Bull. Seismol. Soc. Am., 59, pp. 1281-1305, 1969.
19. McGarr, A., and L. E. Alsop, "Transmission and Reflection Rayleigh Waves at Vertical Boundaries," J. Geophys. Res., 72, pp. 2169-2180, 1967.
20. Alewine, R. A., "Application of Linear Inversion Theory Toward the Estimation of Seismic Source Parameters," Ph.D. Thesis, California Institute of Technology, p. 189, 1974.
21. Hill, P., and C. Pakiser, "Seismic-Refraction Study of Crustal Structure Between the Nevada Test Site and Boise, Idaho," Geological Soc. of Amer. Bull., 78, p. 685, 1967.

22. Lacoss, R. T., "A Large Population LASA Discrimination Experiment," Lincoln Laboratory Contract Report 1969-24, April 1969.
23. Kolar, O. C., and N. L. Pruvost, "Earthquake Simulation by Underground Explosions," Lawrence Livermore Laboratory Reprint, February 1974.

APPENDIX A

EXPLOSION YIELD ESTIMATES BASED ON SEISMIC MAGNITUDE
OBSERVATIONS: DEPENDENCE OF MAGNITUDES ON YIELD,
NEAR SOURCE MATERIAL PROPERTIES, DEPTH OF BURIAL
AND EARTH STRUCTURE

I. INTRODUCTION

We consider, from the onset, that the simplest and most reasonably implemented approach to the estimation of explosive yield using seismic information is through the direct use of the observed seismic magnitude data for the event. We assume that seismic magnitudes will be measured from a number of detectors in the teleseismic range beyond 1000 km and over a range of azimuths covering, at least, an interval of 180°.

The magnitude data that we will consider are m_b , or body wave magnitude, and M_s , or surface wave magnitude, observed for a given event at a number of detectors. In the present discussion we will concentrate most of our attention on the body wave magnitude data since the P wave signal from which m_b is calculated is the most easily detected at teleseismic distances and is most simply interpreted in terms of yield. In particular, the first cycle or two of the wave signal is less perturbed by source zone "anisotropies" or asymmetries such as oriented joints in the rock, initial prestress, or the initial cavity shape. Further, earth structure variations between the different source-receiver paths are strongest in the crust and upper mantle and therefore will usually effect surface waves more strongly than teleseismic body waves. To some degree, however, the stability of the m_b measurement is similarly reduced, since the high frequency body wave is subject to "scattering" by the crustal layering near the source and at the different receivers, giving rise to m_b fluctuations from receiver to receiver. Further, the anelastic effects are much stronger for the high frequency body waves than they are for the much lower frequency surface waves. This rather strong dependence of observed m_b values on structural detail at the source and

receiver and on the upper mantle anelastic properties requires that we have reasonably detailed knowledge of the relevant earth structure. However, it is felt that corrections for the variations of structure that effect the body wave magnitude measurements are more easily and reliably affected than are the corrections required for surface waves. Hence, we have concluded that an m_b measurement, followed by earth structure corrections, will probably give the best yield estimates. Even so, the complementary use of M_s data is highly desirable, since it provides an independent measurement of yield that can, under favorable circumstances, be as reliable or even more reliable than the body wave magnitude data.

In particular, in a very careful study of seismic magnitudes of underground explosions, Basham and Horner (1973) concluded that Rayleigh wave magnitude (M_s) is a more consistant indicator of explosion yield than P wave magnitude. The M_s formula used by Basham and Horner is

$$M_s = \log A_R + B'(\Delta) + P(T) + S, \quad (1.1)$$

which was suggested by Marshall and Basham (1972). In this formula, A_R is the maximum observed Rayleigh wave displacement, $B'(\Delta)$ is the distance normalization term and $P(T)$ is a path correction term which is a function of the period (T) at which A_R is measured. The quantity S is a station correction determined by a statistical analysis of many explosion events recorded by the Canadian Seismic Network. These M_s values appear to be the best currently available in terms of consistancy of measurement and minimization of path and station effects.

Basham and Horner plotted M_s versus yield for 11 NTS explosions in tuff and rhyolite along with two (Gasbuggy and Rulison) explosions in western Colorado. The M_s values for an additional set of 18 NTS tuff/rhyolite explosions with

unpublished yields were also given. A least squares linear fit for the explosions with published yield was given by Basham and Horner as

$$M_s = 1.23 \log W + 1.56 . \quad (1.2)$$

Adding the yield data for the remaining events, this relation is altered to

$$M_s = 1.19 \log W + 1.59 . \quad (1.3)$$

Calculating the error by dividing the difference between predicted and actual yields by the actual yield, one finds that Eq. (1.3) gives an average error of 30 percent for these 28 events. Several of the events have anomalously large errors. Removing the four worst of these from consideration, the average error is reduced to 23 percent.

Using the same approach for body wave magnitude observations, Basham and Horner established the empirical magnitude-yield relationship

$$m_b^* = 1.09 \log \underline{Y} + 3.07 \quad (1.4)$$

where m_b^* is defined as

$$m_b^* = m_b + \log T \quad (1.5)$$

with T the period of the cycle of P wave motion used to compute the magnitude and m_b the usual body wave magnitude defined by

$$m_b = \log (A/T) + B \quad (1.6)$$

Here A is the zero to peak ground motion in millimicrons measured from the largest cycle of motion in the first few cycles (i.e., first three cycles) of P wave motion from the event. The B factor is the distance correction based on the source to receiver distance.

Adding yield data unavailable to Basham and Horner, the relation (1.4) is altered to

$$m_b^* = 0.913 \log \underline{Y} + 3.53 . \quad (1.7)$$

Once again the error may be calculated by dividing the difference between predicted and actual yields by the actual yield. Thus, one finds that Eq. (1.7) gives an average error of 50 percent for these 28 events. This should be compared to the 30 percent average error in yield prediction based on M_s .

It is of considerable importance that we isolate the origins of the scatter in the magnitude-yield relation since even for the carefully measured and empirically corrected data from Basham and Horner, a rather large scatter remains. This results, of course, in a rather large uncertainty in estimation of yield if these purely empirical relations are used. It is clear, however, that we will have different magnitude-yield relations for explosions in different near source materials and if the receiver array is such as to sample the seismic field after it has propagated through vastly different earth structures. Thus, the magnitude-yield relation for hard rock materials is different than that for soft rock materials and further the relation will be different as measured by an array in a shield area as opposed to a detector array in an active tectonic area.

It is desirable, therefore, to establish, in a deterministic fashion, magnitude-yield relations that are appropriate for particular receiver arrays and source locations where depth and near source material properties are also

variable. Equivalently, the magnitude observations may be corrected for source-receiver structure effects, near source material properties, depth and other variables affecting the magnitude observations in a deterministic fashion in order to greatly reduce the scatter in a magnitude-yield relation. In either approach it is necessary to determine which parameters affect the magnitude measurement, and the precise dependence of the magnitude measurement on these parameters. Therefore in this report we will focus our discussion on the variability of m_b and M_s with respect to such variables as near source material properties, initial medium stress state, earth structure and source depth.

In order to see, in a simple and direct way, the relationship of seismic magnitude to the source properties, we will introduce the reduced displacement potential, $\psi(\tau)$. We can easily demonstrate that all seismic magnitudes depend on the single source function, ψ , in a simple way.

Consider first the seismic body wave magnitude m_b from an explosion. For a spherically symmetric explosion the reduced displacement potential, $\psi(\tau)$, is related to the radial displacement, $u(t,r)$, by

$$u(t,r) = \frac{\psi(\tau)}{r^2} + \frac{\dot{\psi}(\tau)}{r^\alpha}, \quad (1.8)$$

where t is time,

r is radial distance from the source,

α is compressional velocity in the source region,

$\tau = t - r/\alpha$, the retarded time.

Note that the steady state value of the reduced displacement potential (RDP) is given by

$$\psi(\infty) = r^2 u(\infty, r) \quad (1.9)$$

where $u(\infty, r)$ is the static displacement at the radius r .

Since the seismometer filters the displacement wave form, it is convenient to transform Eq. (1.8) into the frequency domain. We find

$$\hat{u} = \frac{1}{r^2} + \frac{i\omega}{r\alpha} \hat{\psi}. \quad (1.10)$$

In the teleseismic field, many wavelengths from the source, the term attenuating as r^{-2} is negligible. Therefore, the teleseismic body wave, u_b , is

$$\hat{u}_b = \frac{i\omega}{r\alpha} \hat{\psi} = \frac{\dot{\hat{\psi}}}{r\alpha}, \quad r \gg \frac{\alpha}{\omega}. \quad (1.11)$$

Since the spectrum of $\hat{\psi}$ for an explosion (see Section II) is essentially flat in the teleseismic frequency band ($f < 2$ Hz), then Eq. (1.11) may be written

$$\hat{u}_b = \frac{\psi(\infty)}{r\alpha}, \quad (1.12)$$

where we have used a basic property of the Fourier transform, namely

$$\hat{\psi}(0) = \psi(\infty). \quad (1.13)$$

Since $\psi(\infty)$ has dimensions of L^3 (Eq. (1.9)), then using cube-root scaling we find that both $\psi(\infty)$ and teleseismic body wave displacement should scale directly as the device yield. This important result assumes that the near source material properties do not change, the only variable being the yield of the explosive.

Consequently we have that

$$m_b \sim \log \left[\frac{\psi(\infty)}{\alpha} \right] = \log \left[\frac{\dot{\hat{\psi}}(0)}{\alpha} \right] \quad (1.14)$$

with $\psi(\infty) \sim \underline{Y}$, \underline{Y} being the explosion yield

For the surface wave magnitude M_s we have a similar result. In particular, the spectrum of the vertical surface displacement, \hat{w}_0 , for the Rayleigh waves propagating in a multilayered medium, excited by a source of pure dilatation in a layer with material index s is given by Harkrider (1964, 1971), as

$$\hat{w}_0 = -4\pi i \mu_s \hat{\psi}_s(\omega) k_R K_R A_R e^{i\tau_s} H_0^{(2)}(k_R r) \quad (1.15)$$

where

μ_s = rigidity of the material in layer s ,

$\hat{\psi}_s(\omega)$ = Fourier transformed reduced displacement potential,

$k_R = \omega/c_R$ where c_R is the Rayleigh wave velocity at the frequency ω ,

K_R = depth dependent Rayleigh wave excitation factor,

A_R = amplitude response of the multilayered medium,

$\tau_s = \omega R_0 / \alpha_s$ where R_0 is the effective "cavity" radius for the explosion and α_s is the P wave velocity in layer s ,

$H_0^{(2)}(k_R r)$ = Spherical Hankel function of the second kind.

Except for the small shift in origin time, τ_s , the only source dependent term is $\hat{\psi}_s(\omega)$, the reduced displacement potential. The remaining terms are nearly independent of depth of burial for depths typical of underground explosions. Further, only a small correction is required for the case of an explosion in one medium (e.g., tuff) exciting Rayleigh waves in an average source-receiver crustal structure which is predominantly of granite-like materials.

For the long periods which are of interest for surface wave observations, the source spectrum, $\hat{\psi}_s(\omega)$, is equal to the constant value $\hat{\psi}_s(\infty)$ (see Section II also). With these observations, (1.15) implies that surface wave magnitude is simply related to the source by the proportionality relation

$$M_s \sim \log [\mu_s \hat{\psi}(\infty)] . \quad (1.16)$$

We see that the magnitude m_b and M_s should therefore be related to yield by relations of the form

$$\left. \begin{aligned} m_b &\sim \log \underline{Y} + B \\ M_s &\sim \log \underline{Y} + C \end{aligned} \right\} \quad (1.17)$$

where the coefficient of the $\log \underline{Y}$ term should be close to unity and B and C will be explicitly dependent on the compressional velocity and rigidity of the medium at the source, respectively.

Therefore, we see that all source parameter effects on seismic magnitudes may be discussed in terms of $\hat{\psi}(\omega)$, μ and α .

The success of a deterministic approach to magnitude prediction, wherein earth structure, near source material properties and a variety of other factors are taken into account can be gauged from the results shown in Figure 1.1. Here the circles indicate $m_b^{(1)} - M_s$ values computed from theoretically produced seismograms, where $m_b^{(1)}$ is the magnitude measured from the first cycle of P wave motion and M_s is measured from the 20 second Rayleigh wave (vertical component). The line to the right of the circles indicates the m_b value obtained from a measurement of the largest P wave amplitude in the wave train (the second cycle of motion was actually used). The squares indicate the values of M_s that

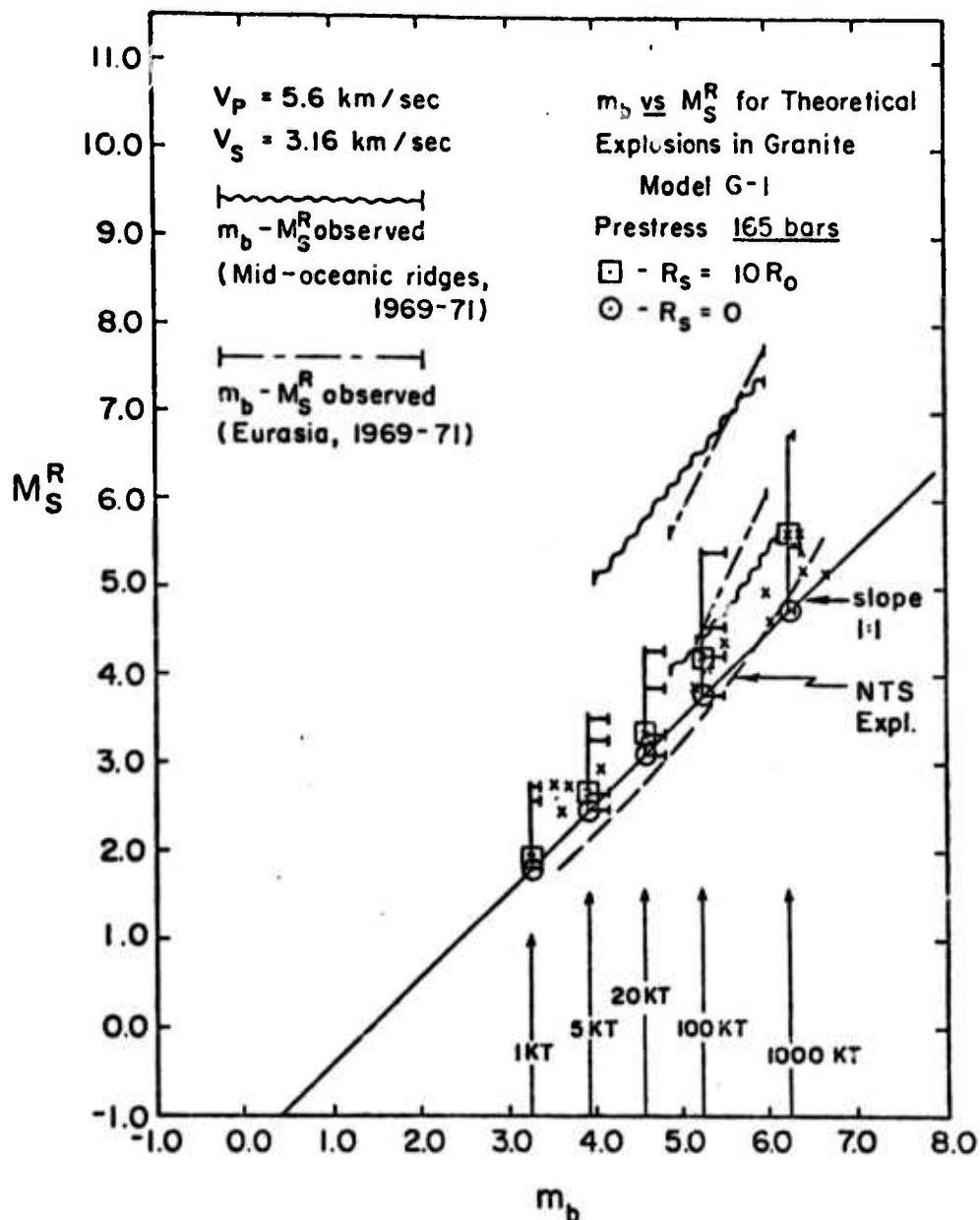


Figure 1.1. Rayleigh surface wave magnitude as a function of body wave magnitude for explosions in granite (model G-1). The circles denote theoretical values of $m_b^{(1)}$ and M_s^R for zero prestress, the squares for 165 bar prestress. The horizontal lines indicate the range of possible m_b values, the vertical lines the range of possible M_s^R values. The upper and lower bound lines for earthquake data are shown for comparison along with the mean NTS explosion magnitude line. The X symbols are individual explosions defining the extreme upper range of observed M_s^R values for explosions. The yields of the explosions are indicated along the m_b scale.

are measured for the same explosions but with tectonic release, under the condition that the medium was prestressed in shear to a 165-bar level. The vertical lines indicate the range of M_s that could be assigned to the individual explosions, the precise value depending on the period of the surface wave used in the measurement. The extreme (upper) value of the M_s magnitude for a given explosion is obtained if the, so called, Airy phase of the surface wave train is used, corresponding to an amplitude measurement at a period of from 12 to 14 seconds. Clearly then, measurement procedures will affect the magnitudes obtained and a stricter definition of the magnitude measurement is called for in order to reduce the scatter in m_b and M_s measurements. (No latitude in the cycle used for the P wave amplitude measurement and only the 20-second surface wave measured, for example.)

These results are in good agreement with observations, as is shown by the NTS = $m_b - M_s$ line. The crosses appearing in the figure are large M_s explosions and indicate the upper bound on the $m_b - M_s$ population. The fact that the theoretical results are somewhat above the NTS line is expected, in that the medium model used was for granite while most of the NTS explosions were in soft materials (e.g., tuff).

The results may be put in the form of theoretically predicted magnitude-yield relations which are shown in Figures 1.2 and 1.3. These may be compared with the empirically determined equations (1.3) and (1.7). The agreement is quite good considering the fact that the empirical data includes explosions in a variety of near source material types.

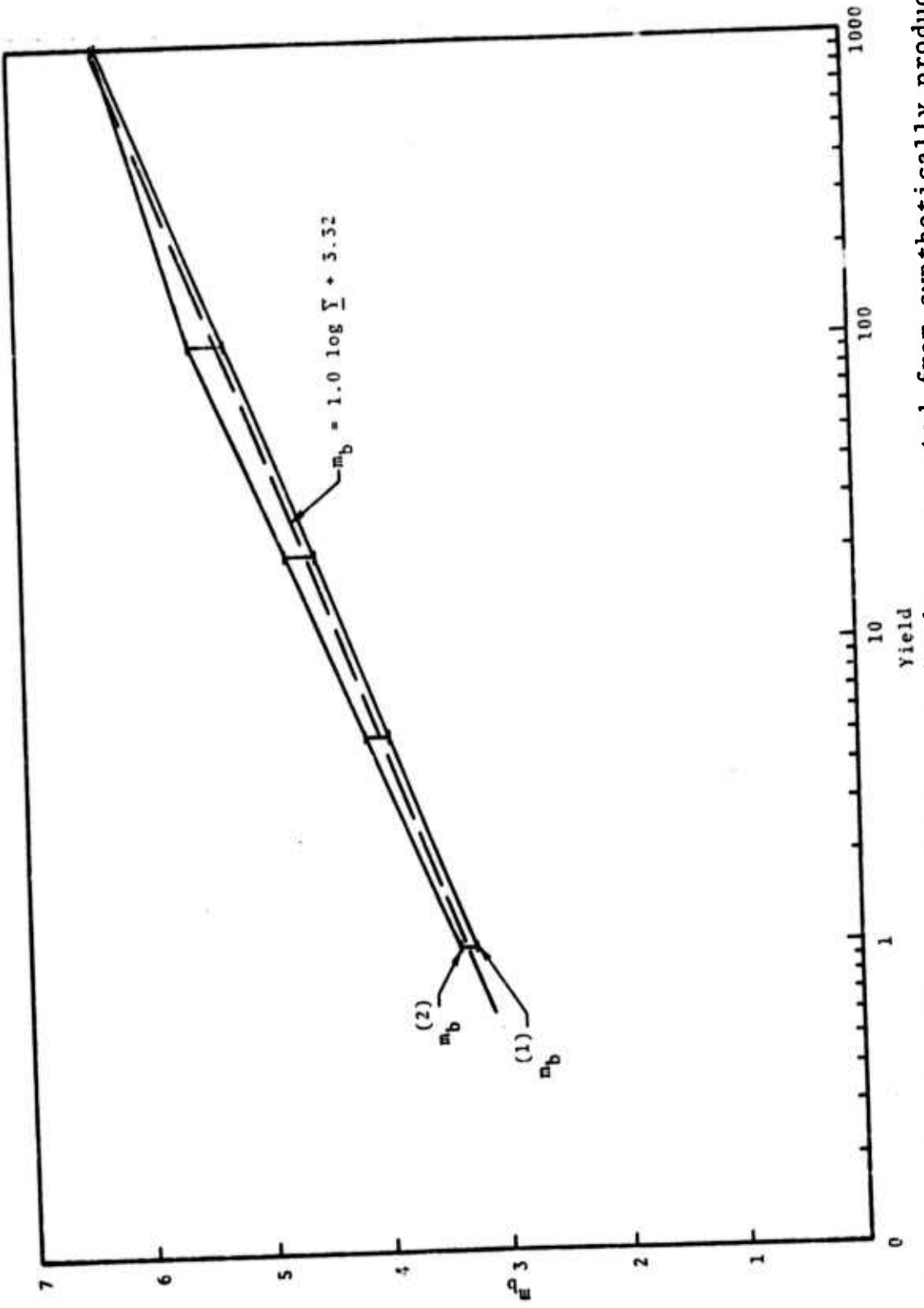


Figure 1.2. Theoretical body wave magnitude mb computed from synthetically produced seismograms as a function of explosion yield in granite (model G-1) using the CIT 109, 0.5Q earth model. The mb value denoted $mb(1)$ was measured from the first cycle of P wave motion while $mb(2)$ was measured from the second cycle of motion, which was the largest cycle of P wave motion. The $mb(2)$ measurement is somewhat contaminated by the P arrival.

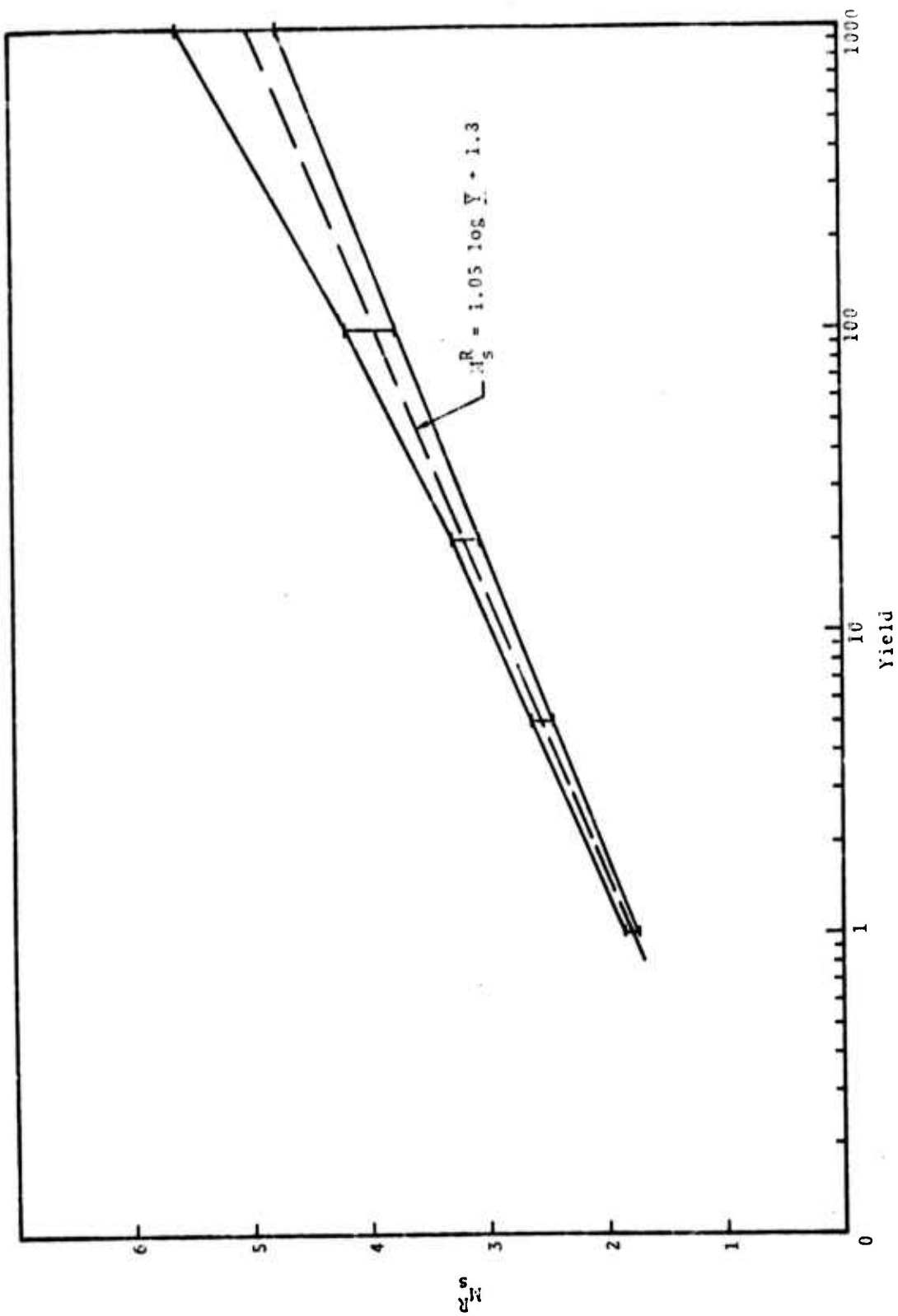


Figure 1.3. Theoretical surface wave magnitude (Rayleigh) computed from synthetically produced seismograms as a function of yield in granite (model 6.1) using the CIT 109, 0.5Q model. The lower M_s value is for explosions without tectonic release, the upper values for explosions in media prestressed in shear to 165 kbars.

These theoretical results strongly suggest that the detailed source description used is accurate and that we can use this capability to either predict the magnitude-yield relations for a wide variety of source and medium conditions or that we can correct observed magnitude data for variability other than yield, to obtain very accurate yield estimates.

In the following sections we give a detailed discussion of all the factors influencing magnitude, from the point of view of yield estimation based on magnitude, with each of these sections containing a concise summary.

II. THE DEPENDENCE OF TELESEISMIC MAGNITUDES ON NEAR SOURCE MATERIAL PROPERTIES

2.1 INTRODUCTION

In order to determine teleseismic amplitude dependence on near source rock environment, it is necessary to obtain an equivalent elastic source that matches the propagation characteristics of the real source at distances over which the medium response is linear elastic. Explosion source function prediction is possible if one is able to simulate a propagating stress wave in at least a spherically symmetric geometry. For nuclear sources, this simulation requires an understanding of material behavior from a few megabars in pressure down to the elastic level. The source function is obtained from the calculated displacement or velocity history of a particle in the elastic region.

By and large, seismologists have been forced to use experimentally determined explosion source functions for teleseismic ground motion predictions. These source functions are limited in number, quality and the rock environment they represent. These limitations are due mainly to the expense and technical difficulty involved in fielding an experiment designed to obtain free field, time history data in the elastic regime for a nuclear source.

Computational techniques and material models have been developed at S³ which permit a prediction of the equivalent elastic source given the yield of the explosive and the material properties of the near source geologic environment.

Since laboratory tests on rock samples provide the essential data base for a preshot estimate of material properties, it is important to determine the sensitivity of the equivalent source to those material properties which are

subject to routine laboratory measurement. In this chapter we present the results of a computational parameter study which identifies the dependence of teleseismic magnitude on near source material properties.

2.2 MODEL CONFIRMATION AND RELEVANCE TO TELESEISMIC GROUND MOTION

Before presenting the results of the parameter study, it is important first to establish at least some confidence in the material models capability to predict close in, free field ground motion and second, to identify the manner in which changes in material parameters will be related to changes in teleseismic ground motion.

Figure 2.1 shows measured and predicted ground motion from a nuclear explosion (CYPRESS) at ranges of 550, 700, and 1100 feet from the detonation point. Figure 2.2 compares measured and predicted ground motion from a chemical explosion (Mine Dust HE) at 12 feet from the center of the explosive. Figure 2.3 shows measured and predicted stress history from a nuclear explosion (Misty North) at 180 feet from the detonation point. While agreement is certainly less than perfect in all cases, the computational technique does seem capable of predicting peak positive and negative velocities along with the overall shape of the propagating stress pulse. The late time disagreement between calculated and measured ground motion for CYPRESS could be due to reflected waves obscuring the free field portion of the measurements.

The results presented in Figures 2.1 through 2.3 show velocity or stress histories at various distances from the source. For teleseismic ground motion it is possible to reduce the coupling efficiency to a single number, ψ_∞ , which scales directly with the yield of the explosion.

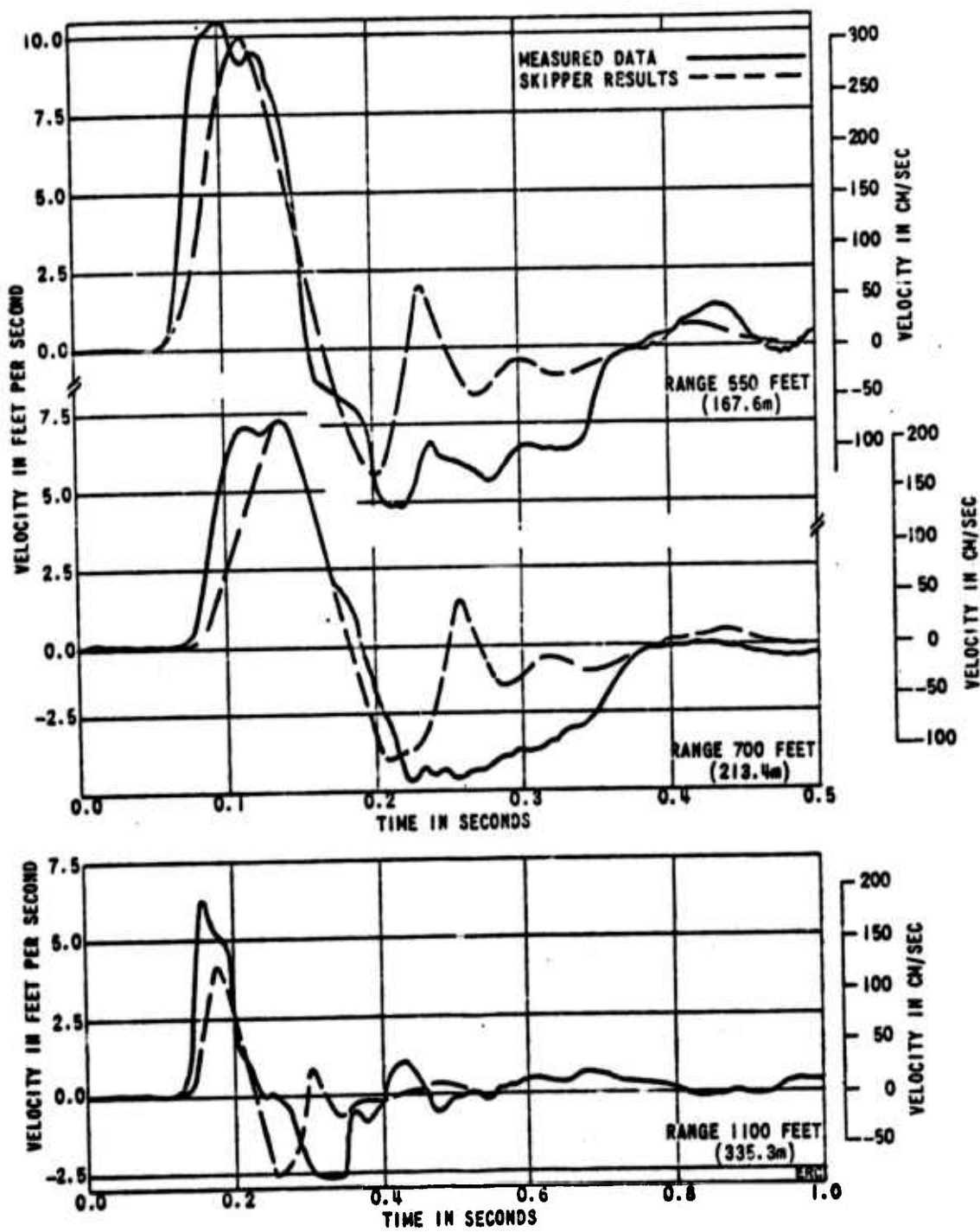


Figure 2.1. Comparison between predicted and observed ground motion from CYPRESS.

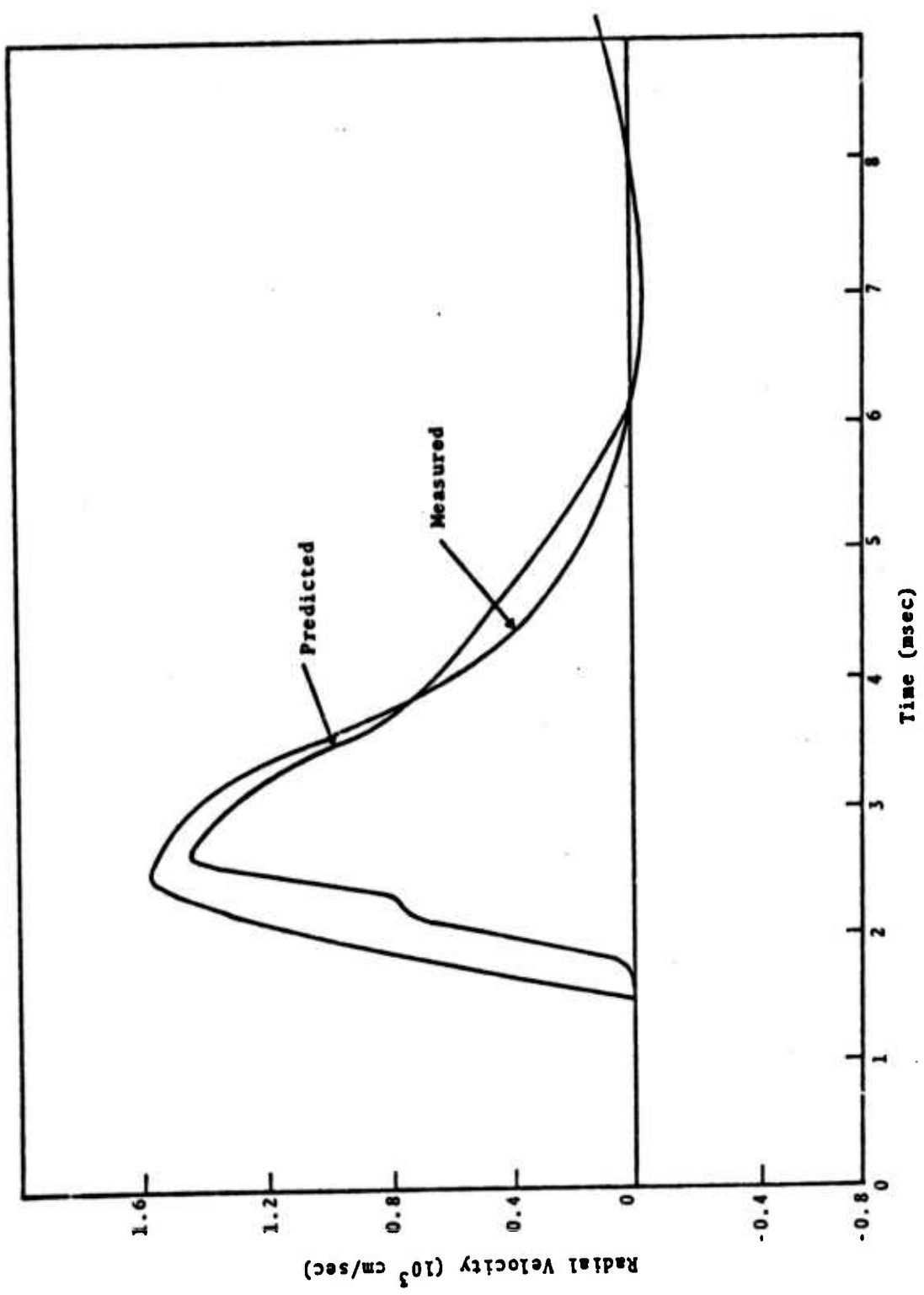


Figure 2.2. Predicted and measured radial velocity histories at 12 feet from Mine Dust HE source.

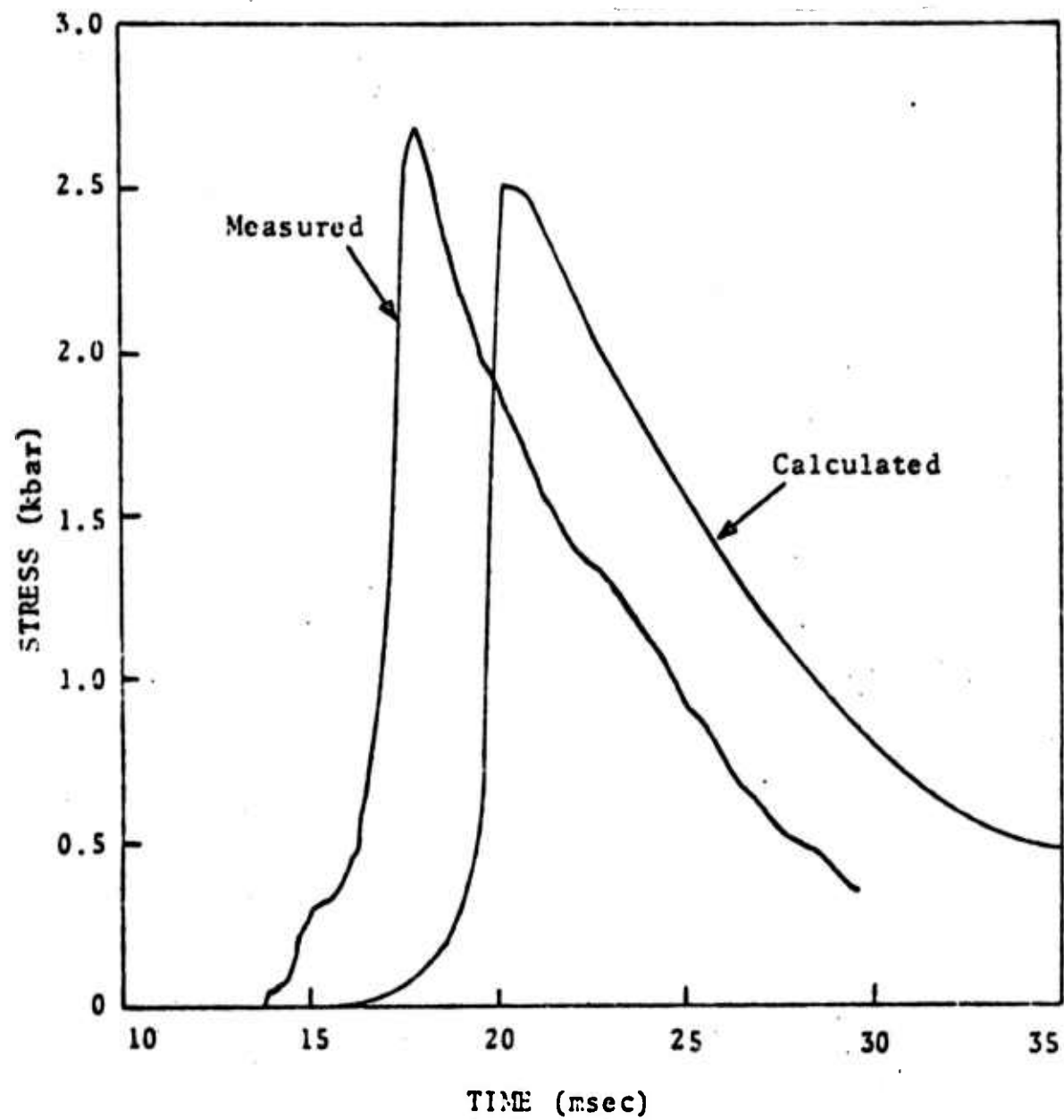


Figure 2.3. Stress-time waveform at 180 feet and predicted waveform at same location for Misty North.

For a spherically symmetric source, the reduced displacement potential, ψ , is defined by

$$u(t, r) = \frac{\psi}{r^2} + \frac{\dot{\psi}}{r\alpha}, \quad (2.1)$$

where $u(t, r)$ = radial particle displacement at t and r ,

α = P wave velocity in the medium,

r = radial position,

$\tau = t - r/\alpha$, retarded time,

$\dot{\psi} = d\psi/d\tau$, reduced velocity potential.

In the elastic region

$$\frac{\partial^2 \psi}{\partial t^2} = \alpha^2 \frac{\partial^2 \psi}{\partial r^2}$$

Therefore ψ depends only on τ and its wave form does not change with changing r .

Given the displacement time history, $u(t, r)$, at an arbitrary radius from the source, then Eq. (2.1) may be used to determine $\psi(\tau)$. The value of $\psi(\tau)$ so determined will be independent of radius if the displacement time history was chosen in the elastic zone.

From Eq. (2.1) the steady state value of the reduced displacement potential is given by

$$\psi(\infty) = r^2 u(\infty, r) \quad (2.2)$$

where $u(\infty, r)$ is the static displacement at the radius, r .

For all the calculated reduced displacement potentials obtained to date it has been found that teleseismic body wave

magnitude, m_b , has the proportionality

$$m_b \sim \log \left[\frac{\psi(\infty)}{\alpha} \right], \quad (2.3)$$

while surface wave magnitude, M_s , obeys

$$M_s \sim \log [\mu \psi(\infty)] \quad (2.4)$$

where μ is the shear modulus of the near source material.

Equations (2.3) and (2.4) are valid for device yields up to approximately 250 kT. Their form is a consequence of the source spectrum's frequency content in the teleseismic band ($f < 2$ Hz). Our calculated spectra are essentially flat over this frequency interval for device yields up to 250 kT. Therefore, changes in teleseismic magnitudes caused by changes in near source material properties may be obtained by comparing the values of $\psi(\infty)$ appropriate for each material.

If $\psi_i(\infty)$ and $\psi_k(\infty)$ are two values of $\psi(\infty)$ corresponding to materials i and k then the change in teleseismic magnitude is given by

$$\Delta m = m^{(i)} - m^{(k)} = \log \left[a \frac{\psi_i(\infty)}{\psi_k(\infty)} \right], \quad (2.5)$$

where

$$a = \frac{\alpha_k}{\alpha_i} \text{ for } m_b$$

and

$$a = \frac{\mu_i}{\mu_k} \text{ for } M_s.$$

If material properties remain constant and the only change is device yield, , then

$$\psi_k(\infty) = \frac{w_k}{w_i} \psi_i(\infty),$$

and Eq. (2.5) becomes

$$m^i - m^k = \log \left(\frac{w_i}{w_k} \right). \quad (2.6)$$

Equation (2.5) gives the "scaling" law for teleseismic magnitudes in terms of $\psi(\infty)$. This equation is always valid as long as the spectrum of the equivalent source is flat within the teleseismic frequency band and path effects associated with the earth structure are invariant between events.

2.3 THE SENSITIVITY OF $\psi(\infty)$ TO AIR-FILLED POROSITY, MATERIAL STRENGTH AND OVERBURDEN PRESSURE

A number of calculations have been performed in order to identify the sensitivity of $\psi(\infty)$ to changes in air-filled porosity, material strength and overburden pressure. Table 2.1 lists the material properties along with the calculated value of $\psi(\infty)$ for a source yield of 0.02 kT. Also included in the table is Δm computed from Eq. (2.5) where calculation 5 has been chosen for the reference magnitude, i.e., $k = 5$ in Eq. (2.5). The P wave velocity is 2.4 km/sec and the shear modulus is 40 kbars for all calculations. Therefore, the value of "a" in Eq. (2.5) is unity for this study.

The volume fraction of air-filled voids in the material is obtained from the column labeled ϕ_0 . The effect of air-filled porosity on magnitude is obtained by comparing the results of calculations 1, 6 and 4. Figure 2.4 shows Δm

TABLE 2.1
SUMMARY OF SOURCE COMPUTATIONS

ϕ_0	P_e (kbar)	P_c (kbar)	P_m (kbar)	γ_m (kbar)	P_0 (kbar)	ρ_0 (g/cc)	$\psi(\infty)$ (m ³)	ΔM	Calculation No.
0	--	--	0.6	0.5	0.116	1.94	7.4	0.739	(1)
0.02	0.075	0.5	0.6	0.5	0.116	1.90	3.6	0.426	(6)
0.05	0.075	0.5	0.6	0.5	0.116	1.84	2.1	0.192	(4)
0.02	0.075	0.5	0.6	0.5	0.075	1.90	4.2	0.493	(9)
0.02	0.075	0.5	0.6	0.5	0.348	1.90	2.41	0.252	(11)
0.02	0.075	0.5	0.6	0.5	0.619	1.90	2.08	0.188	(12)
0.02	0.075	0.5	0.6	0.5	0.075	1.90	4.6	0.532	(10)
0.02	0.075	1.25	0.6	0.5	0.116	1.84	3.3	0.388	(3)
0.05	0.15	1.25	0.6	0.5	0.116	1.84	1.35	0	(5)
0.05	0.075	0.5	0.6	1.0	0.116	1.90	7.7	0.756	(7)
0.02	0.075	0.5	1.25	0.5	0.075	1.90			

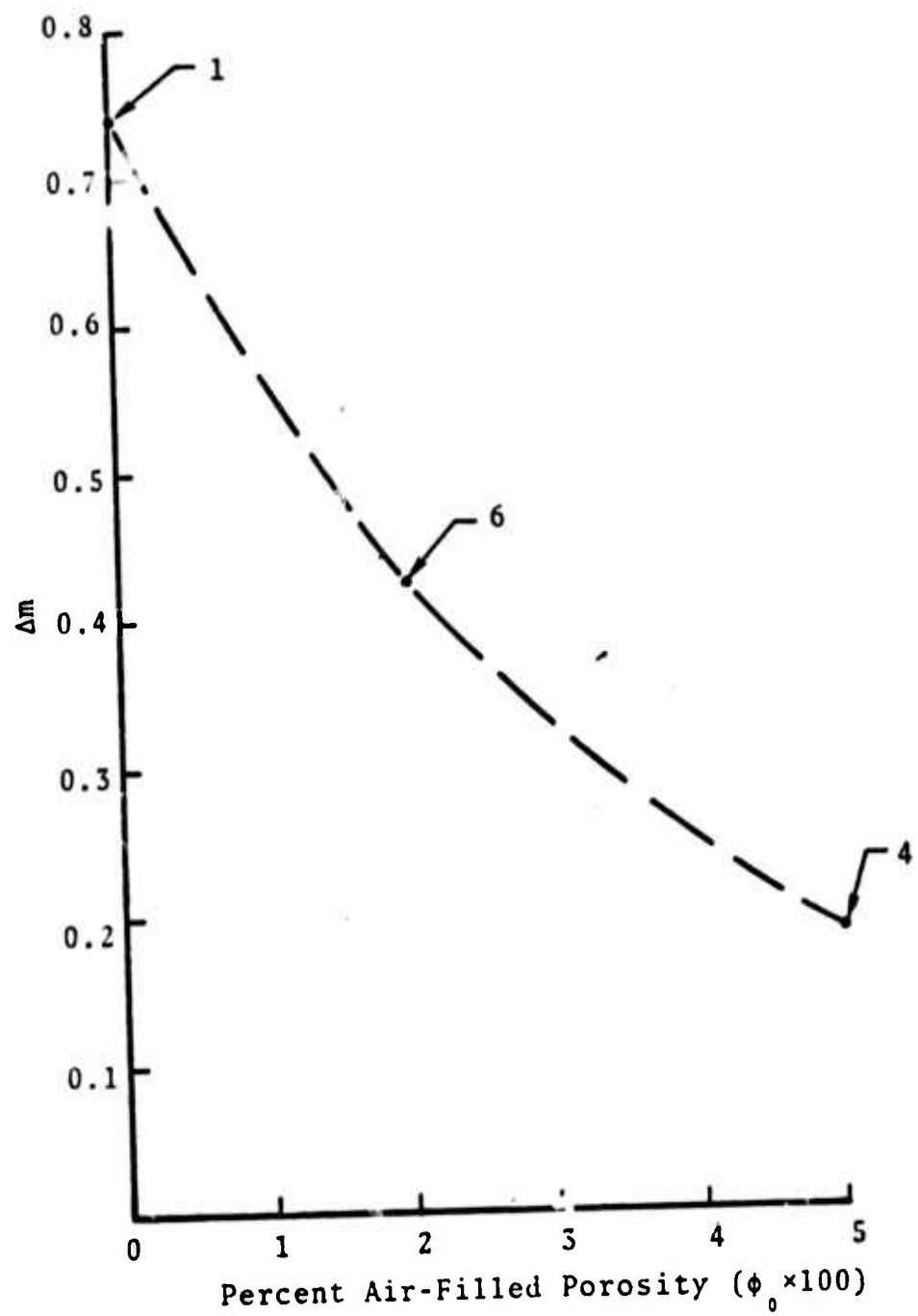


Figure 2.4. Effect of air-filled porosity on magnitude.

versus ϕ_0 for these three calculations. We see that Δm is highly sensitive to changes in air-filled porosity. Over the interval $0 < \phi_0 < 0.02$, magnitude decreases by 0.313 units. A material with 2 percent porosity will give the same magnitude as a material with no porosity if the device yield is increased by a factor of two over that used at the zero porosity site.

Figure 2.5 shows the influence that the maximum allowable material strength, Y_m , has on magnitude. This figure compares the results of calculations 4 and 5. Increasing Y_m by a factor of two causes magnitude to decrease by 0.192 magnitude units. Therefore, the device yield could be increased by a factor of 1.55 in the strong material.

These calculations show that a porous, high strength material optimizes teleseismic decoupling. Increasing both the porosity and material strength may obscure the device yield by at least a factor of three when teleseismic magnitude is used to infer yield. We should note that both high air-filled porosity and high material strength imply that the material characterizing the near source environment is above the water table.

For a given value of Y_m , the shape of the material strength surface is controlled by P_m , the pressure at which Y_m is attained. From calculations 9 and 7 we see that increasing P_m by a factor of 2.08 causes magnitude to increase by 0.26 units. The coupling efficiency increases as P_m is increased, which is opposite to the effect of increasing ϕ_0 or Y_m . This simply indicates that the shape of the failure surface plays an important role in determining coupling efficiency. The material has less strength at low pressures when P_m is increased and we should expect a corresponding increase in magnitude.

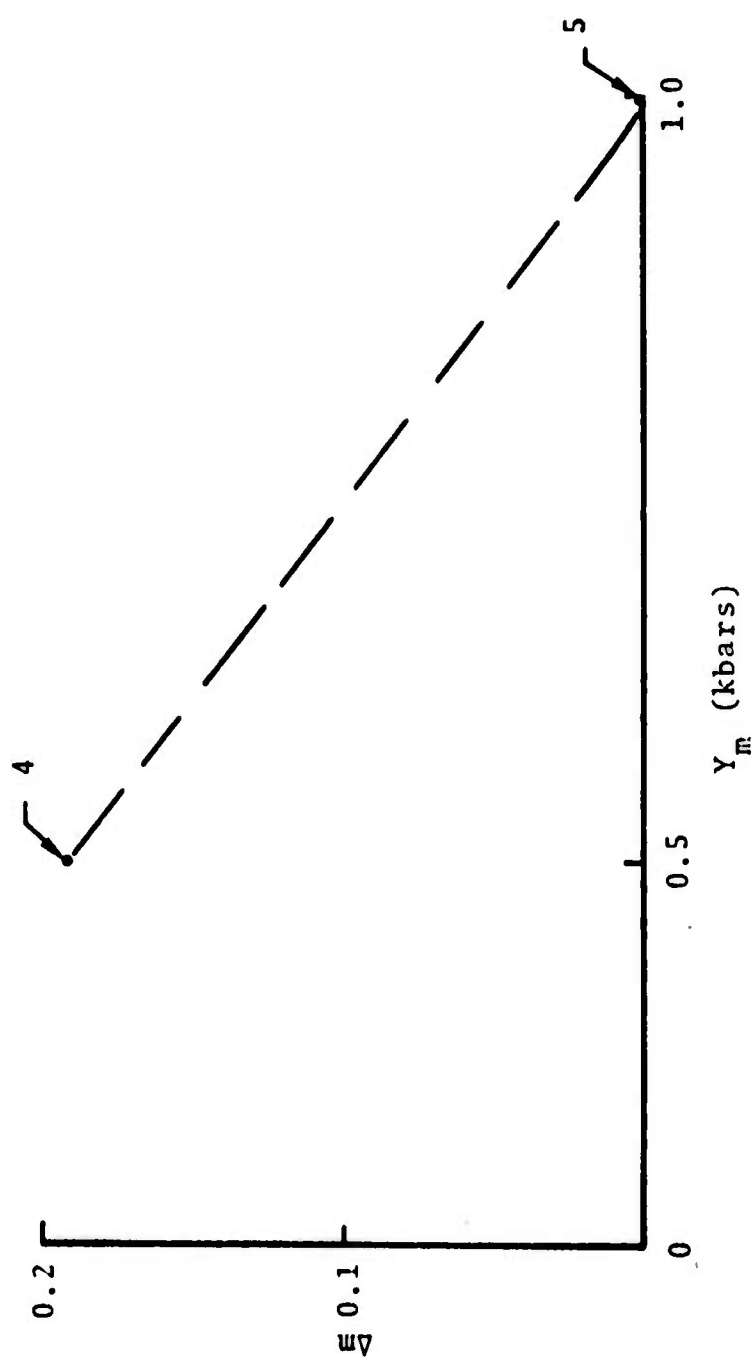


Figure 2.5. Effect of maximum allowable material strength of magnitude.

The effect of overburden pressure, P_o , on magnitude is shown in Figure 2.6. Coupling efficiency decreases with increasing overburden pressure, when all other material properties remain constant. An increase in the depth of burial (DOB) by a factor of six causes magnitude to decrease by 0.3 units, which in turn permits a yield increase by a factor of two. The decrease in magnitude is not uniform with depth. An increase in DOB at shallow depths causes magnitude to decrease more than that caused by an equivalent increase in DOB at greater depths. This effect results from the rapid increase in material strength at low pressures.

We should note that it is unlikely that material properties would remain invariant as overburden pressure is increased from 100 kbars to 600 kbars. An increased DOB usually corresponds to an increase in water content, resulting in decreased air-filled porosity and material strength. These changes would more than compensate for the overburden pressure decoupling effect.

Calculations 9 and 10 show that magnitude is not very sensitive to large changes in P_c , the pressure at which all ambient porosity is irreversibly removed. An increase in P_c by a factor of 2.5 produces an increase in magnitude of 0.03 units.

Finally, calculations 4 and 3 show the sensitivity of magnitude to P_e , the pressure limit at which irreversible pore collapse begins. An increase in P_e produces an increase in coupling efficiency. A preshot estimate of P_e that is incorrect by a factor of two will result in an error in predicted magnitude by 0.2 units.

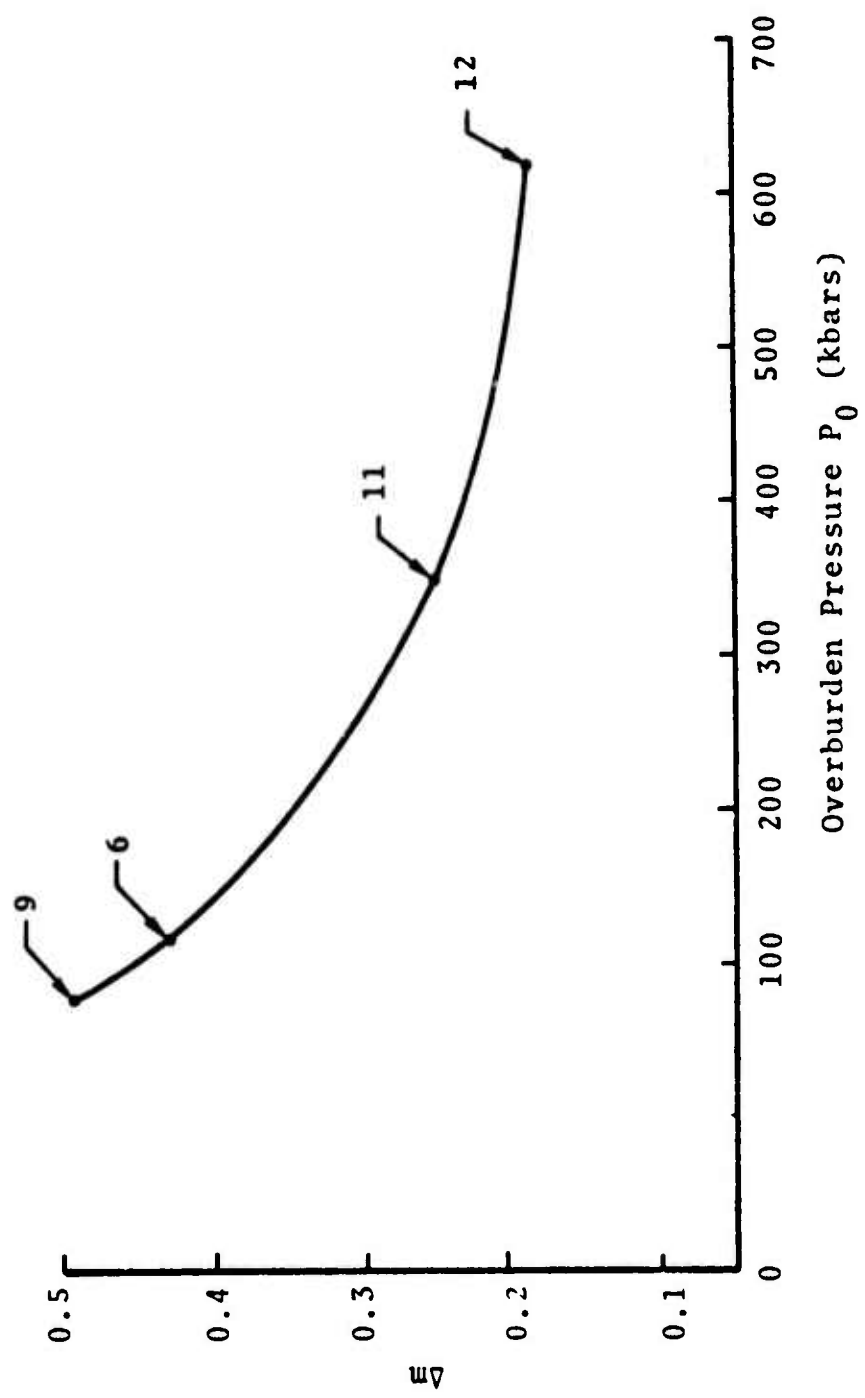


Figure 2.6. Δm versus overburden pressure (P_0).

2.4 SUMMARY

Increases in air-filled porosity, material strength, and overburden pressure reduce seismic coupling. Increasing the pressure at which irreversible pore collapse begins produces an increase in seismic coupling. These are the critical parameters which must be determined prior to a confident prediction of teleseismic magnitude. If any of these parameters is specified without appropriate laboratory tests being performed on rock samples from the near source environment, then predicted magnitude should be suspect by at least 0.2 magnitude units.

For an intrusive igneous rock, i.e., granite, we would expect the major material properties variation to occur from changes in material strength, i.e., variations in porosity are negligible. Therefore, the variation in magnitude between two granite sites could be 0.45 units if the material strength parameters changed by a factor of two between the sites.

The variation in magnitude from changes in the air-filled porosity parameters is 0.513 units where we have limited the porosity to be less than 2 percent and allowed for a factor of two variation in pressure at which irreversible pore collapse begins. For sedimentary and volcanic rocks both porosity and material strength changes between sites could produce a corresponding variation in magnitude of approximately 1.0 magnitude units.

There is no substitute for good, preshot material property data in order to predict the effect of near source geology on teleseismic magnitude. Laboratory tests on appropriate rock samples coupled with density and P wave velocity logs at the site are able to furnish the necessary data required to specify the material properties that

determine seismic coupling. This data base must be established if the effect of near source geology on teleseismic magnitude is to be predicted.

III. DEPENDENCE OF SEISMIC MAGNITUDES ON SOURCE DEPTH, MEDIUM PRESTRESS AND SOURCE ASYMMETRY

In the previous section the influence of the source material parameters on the reduced displacement potential, $\psi(\infty)$, was discussed. This quantity, $\psi(\infty)$, essentially provides the source coupling for elastic waves emanating from the source region and is of paramount importance for determining the amplitude of teleseismic body and surface waves. However, other features also influence the wave train from which measurements of m_b and M_s are ultimately made. One is, of course, the earth structure between source and receiver which is the subject of a subsequent section (Section IV). In this section we consider the effects of medium prestress, source asymmetry (e.g., cavity shape) and free surface generated interference effects, which are dependent on source depth.

3.1 THE DEPENDENCE OF m_b AND M_s ON DEPTH OF BURIAL

The burial depth of the explosion source affects the teleseismic P wave record in several ways. By far the most important is the interference between the direct (P) and free surface reflected (pP) waves. Other depth of burial (DOB) effects include the variation of local material properties and overburden pressure. A minor consideration for explosions is the fact that large DOB changes alter the source-to-receiver travel path and therefore the transfer function. For some events large S waves may be generated due to tectonic release or other causes. In this case the DOB related time lag between P and the reflected sP phase can be important.

III. DEPENDENCE OF SEISMIC MAGNITUDES ON SOURCE DEPTH, MEDIUM PRESTRESS AND SOURCE ASYMMETRY

In the previous section the influence of the source material parameters on the reduced displacement potential, $\psi(\infty)$, was discussed. This quantity, $\psi(\infty)$, essentially provides the source coupling for elastic waves emanating from the source region and is of paramount importance for determining the amplitude of teleseismic body and surface waves. However, other features also influence the wave train from which measurements of m_b and M_s are ultimately made. One is, of course, the earth structure between source and receiver which is the subject of a subsequent section (Section IV). In this section we consider the effects of medium prestress, source asymmetry (e.g., cavity shape) and free surface generated interference effects, which are dependent on source depth.

3.1 THE DEPENDENCE OF m_b AND M_s ON DEPTH OF BURIAL

The burial depth of the explosion source affects the teleseismic P wave record in several ways. By far the most important is the interference between the direct (P) and free surface reflected (pP) waves. Other depth of burial (DOB) effects include the variation of local material properties and overburden pressure. A minor consideration for explosions is the fact that large DOB changes alter the source-to-receiver travel path and therefore the transfer function. For some events large S waves may be generated due to tectonic release or other causes. In this case the DOB related time lag between P and the reflected sP phase can be important.

The variation with depth of the local material property is properly considered a source effect rather than a DOB effect. The dependence of the source spectrum on local material properties was discussed in Section II.

The important parameter controlling the interference between P and pP is the average source-to-surface P wave velocity (v_p^{SS}). For example, a 10 percent decrease in v_p^{SS} results in an 11 percent increase in the arrival time lag between P and pP having the effect of increased depth of burial.

As the overburden pressure (P_o) increases with depth, the effect is to decrease the average low frequency spectral level of the displacement field from the source. For example, in Figure 3.1, the amplitudes of the RVP transforms, $|\dot{\psi}(\omega)|$, from three SKIPPER calculations are compared. The three source models, T-4, T-5, T-6 are identical, except for the overburden pressure. We see that with increasing DOB, the RVP transform exhibits the behavior predicted by the standard scaling laws; that is, a reduced $\dot{\psi}(0)$ and a spectral shift to higher frequencies. However, these effects are quite minor, as a more than two-fold increase in depth results in an apparent yield decrease of about 15 percent, based on the reduced level of $\dot{\psi}(0)$. (Note that $\dot{\psi}(0) = \psi(\infty)$.)

3.2 INTERFERENCE BETWEEN P AND pP

The effect of the free surface on the spectrum of the observed first arrival P wave train may be demonstrated as follows.

Let u_p and u_{pp} denote the displacements for P and pP, respectively. If

$$u_p = F(t), \quad (3.1)$$

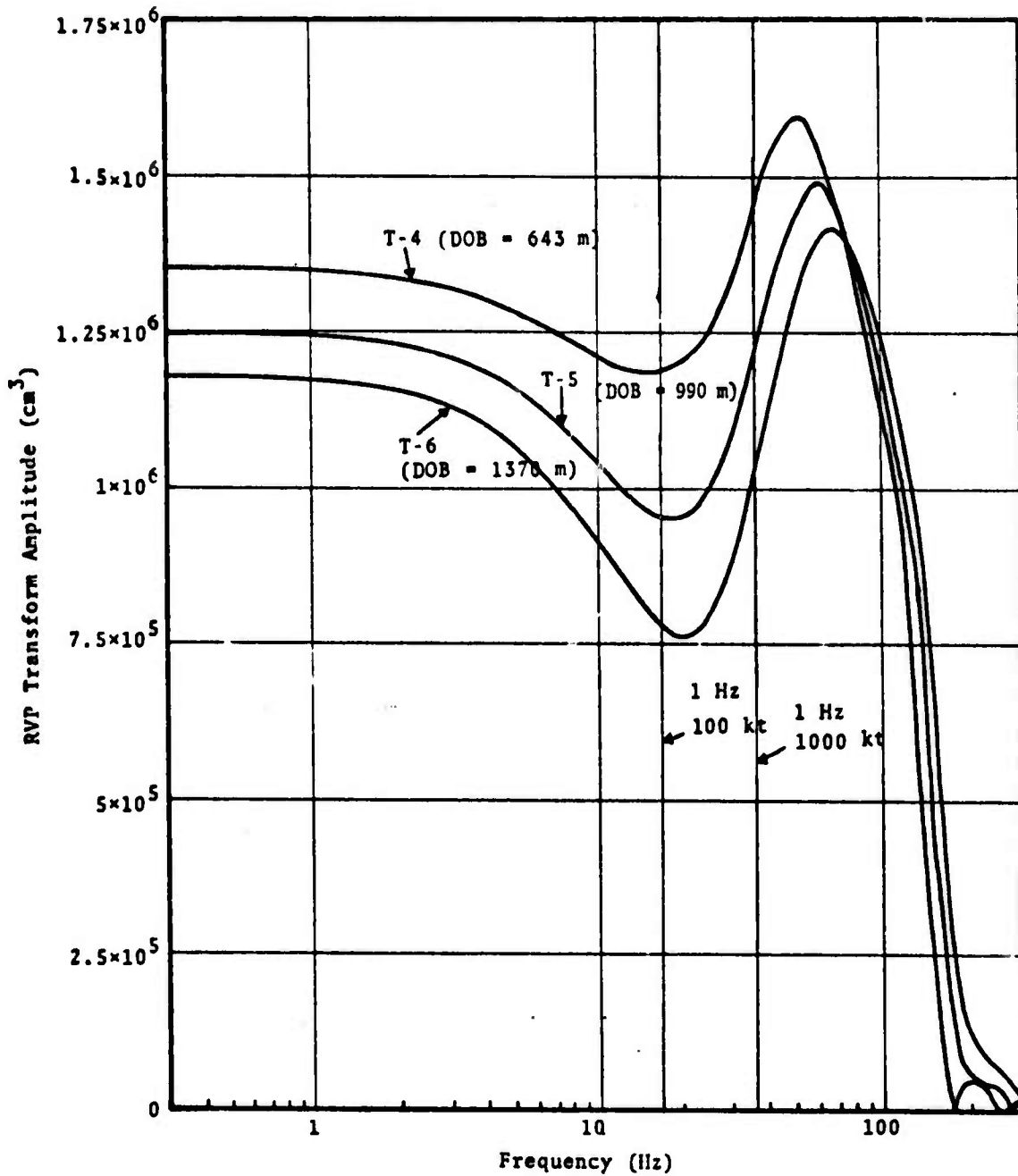


Figure 3.1. Reduced velocity potential transform amplitude versus frequency for tuff source functions T-4, T-5 and T-6. Scale is appropriate to a yield of 0.02 kt. The 1 Hz points for yields of 100 and 1000 kt are shown for reference.

then

$$u_{pp} = -AF(t-T_0) , \quad (3.2)$$

where

A = free surface reflection coefficient (≈ 1),

$$T_0 \approx 2H/V_p^{SS} ,$$

H = depth of burial (DOB),

V_p^{SS} = average source-surface P wave velocity.

In the frequency domain

$$\hat{u}_p + \hat{u}_{pp} = F(\omega) \left(1 - Ae^{-i\omega t_0} \right) , \quad (3.3)$$

and

$$|\hat{u}_p + \hat{u}_{pp}| = |F(\omega)| \left[1 - 2A \cos \omega t_0 + A^2 \right]^{1/2} \quad (3.4)$$

$$= |F(\omega)| \begin{cases} |1-A| , \omega = 2n\pi/T_0 \\ |1+A| , \omega = (2n+1)\pi/T_0 , n = 0, 1, 2, \dots \end{cases} \quad (3.5)$$

The modulation of the frequency spectrum is given by (3.5) with the spectral peaks and troughs occurring alternately at frequencies

$$f = \frac{nV_p^{SS}}{4H} , n = 0, 1, 2, \dots . \quad (3.6)$$

The effect of (3.6) is shown in Figure 3.2 where $|\hat{u}_p|$, $|\hat{u}_{pp}|$ and $|\hat{u}_p + \hat{u}_{pp}|$ are plotted for two yields and burial depths. The two source functions used were T-4 and T-6 of Figure 3.1. Thus, with the exception of overburden pressure, the material properties in the source region were held constant for both calculations and $v_p^{SS} = 2.4 \text{ km/sec}$.

To demonstrate that the shift of the spectral peak occurring for the examples in Figure 3.2 is almost entirely a DOB effect, we show in Figure 3.3 the vertical component of $|\hat{u}_p + \hat{u}_{pp}|$ plotted for six yields ranging from 800 kT with the source to surface travel time held constant.

In order to determine the effect of the interference of P and pP on m_b , it is necessary to consider the time domain signal produced by the two phases. In Figure 3.4 the basic wave form of the first motion P wave train for shallow explosions is shown. The direct P and reflected pP waves are shown along with their summation as recorded by a standard LRSM short period seismometer. In Figure 3.5 the sum of P + pP is shown for a series of burial depths. For all seismograms of Figures 3.4 and 3.5 the source T-3 and the earth structure model CIT 109 0.5Q were used. The epicentral distance was 4087 km corresponding to a ray with takeoff angle $\theta = 13.8^\circ$. For each of the calculations $v_p^{SS} = 2.4 \text{ km/sec}$ and the DOB was varied. However, the significant parameter is the travel time lag between P and pP,

$$t_L = \frac{H}{v_p^{SS} \cos\theta} (1 + \cos 2\theta) . \quad (3.7)$$

This parameter includes the combined effect of DOB and v_p^{SS} . The takeoff angle correction is small for teleseismic distances.

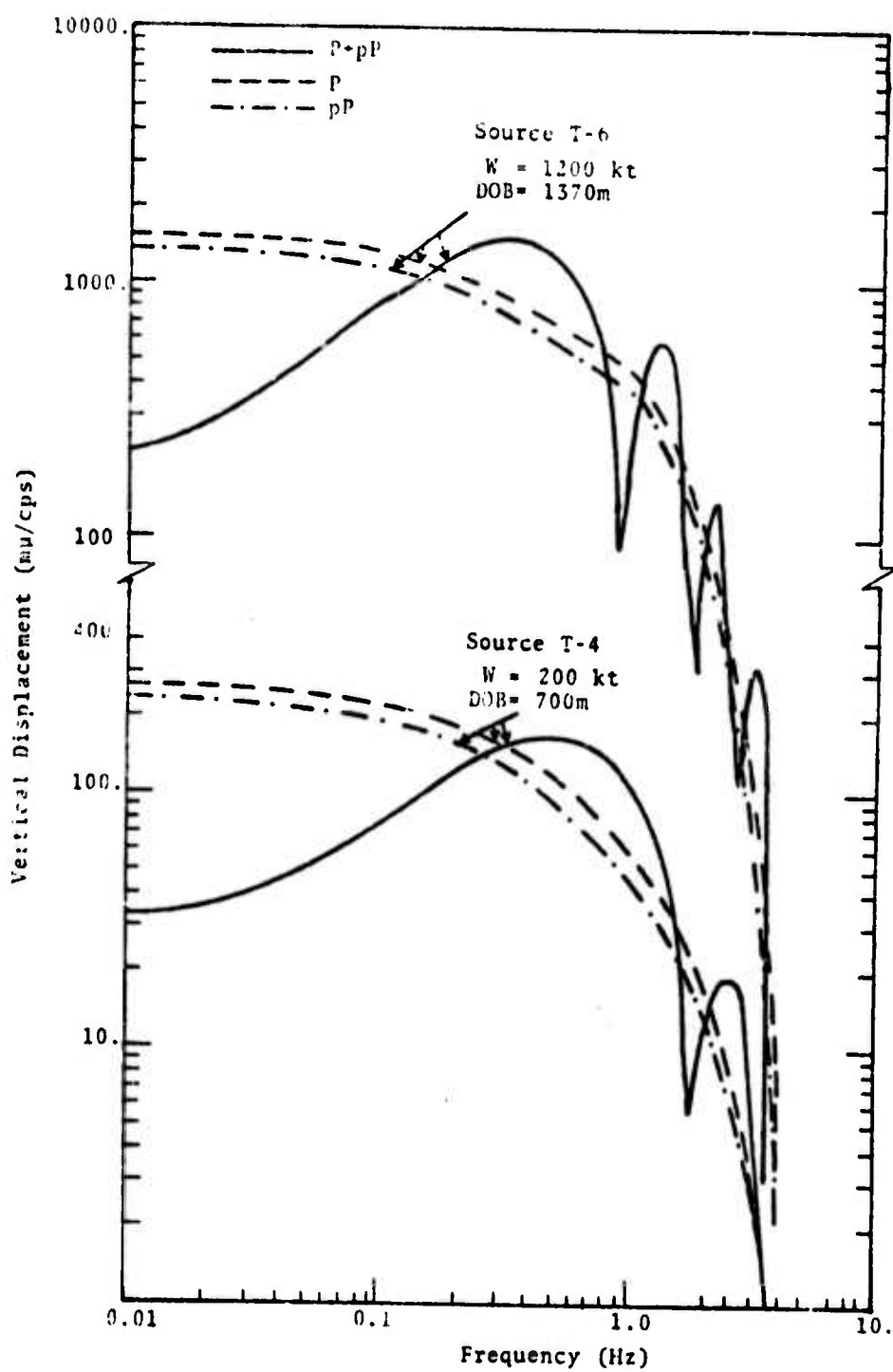


Figure 3.2. Vertical component P wave spectra at an epicentral distance of 3000 km for explosions in tuff at two yields and burial depths.

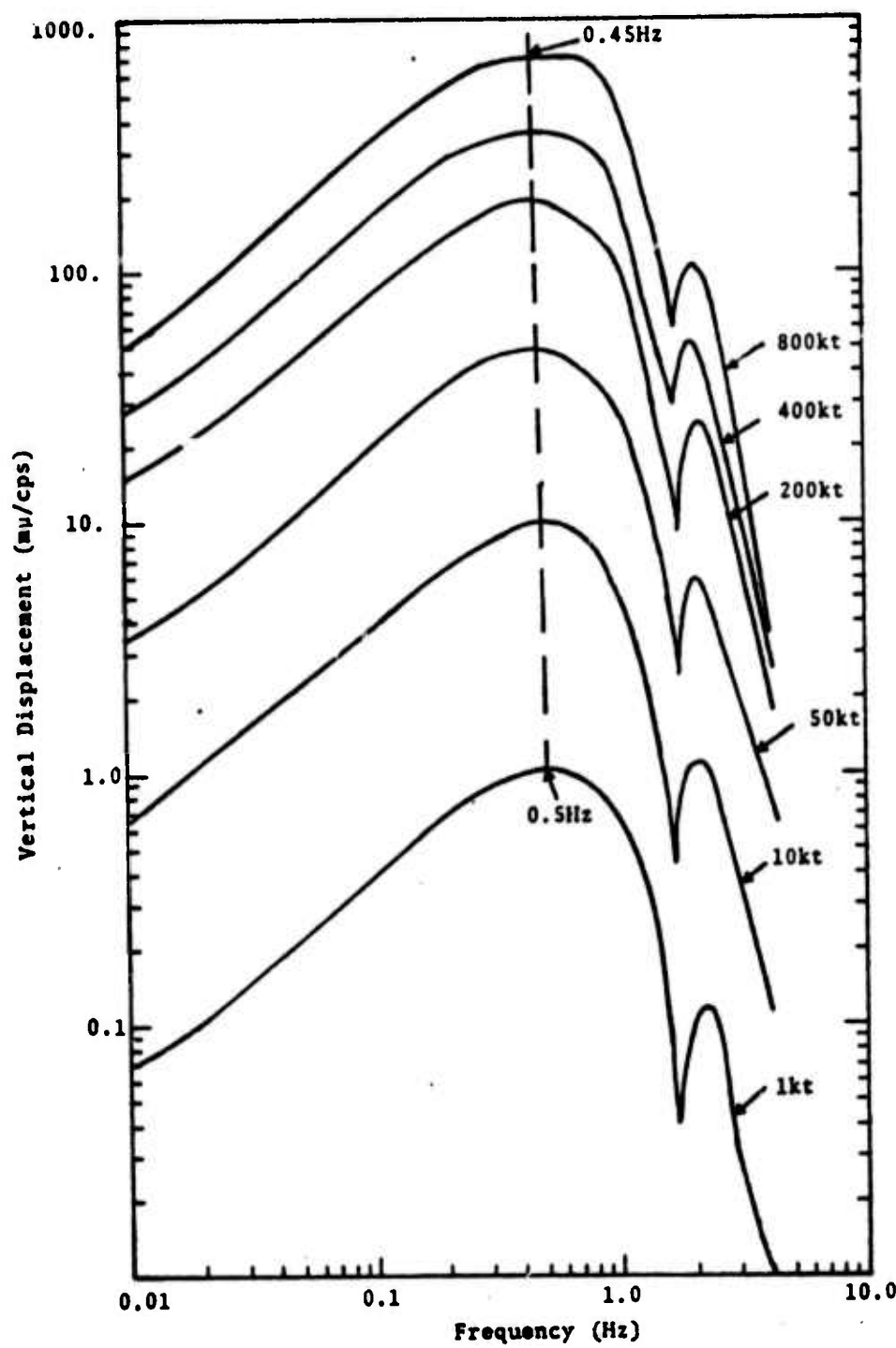
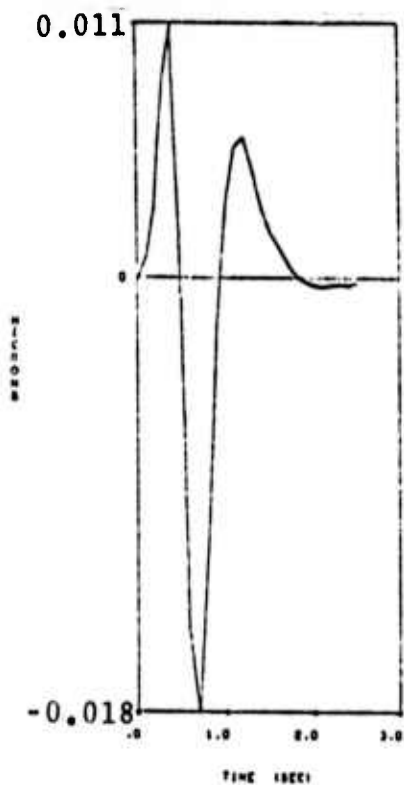
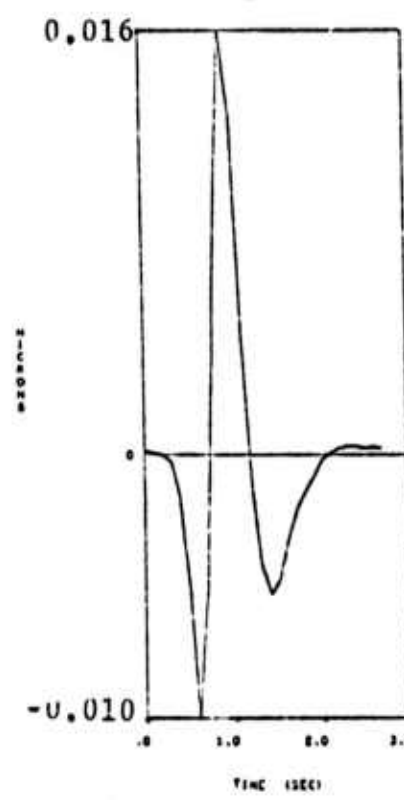


Figure 3.3. Vertical component P wave spectra for various yields at a constant DOB = 700 m. Data is for T-4 at an epicentral distance of 5000 km.



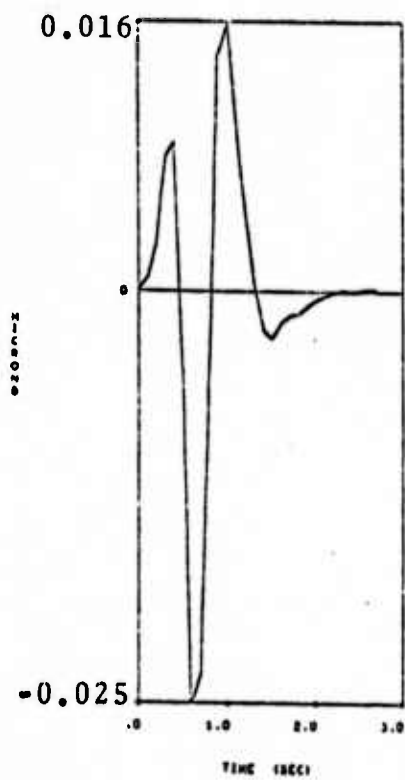
(a) Direct P Wave (P)



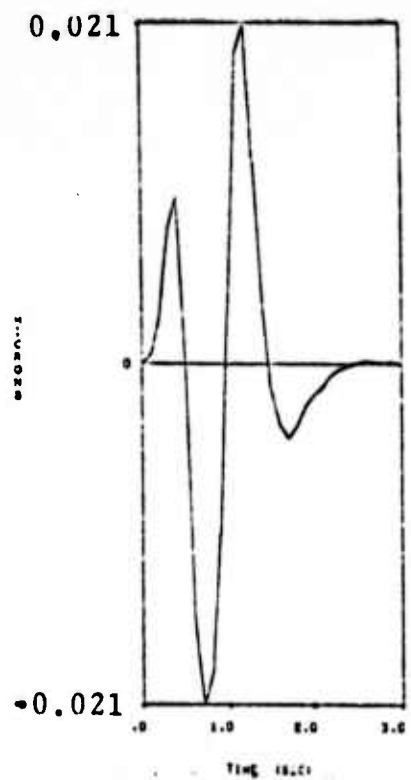
(b) Reflected P Wave (pR)

Figure 3.4. The construction of the first arrival P wave train from the direct and reflected phases.
DOB = 300 m, $V_{SS} = 2.4$ km/sec, $t_L = 0.24$ sec.

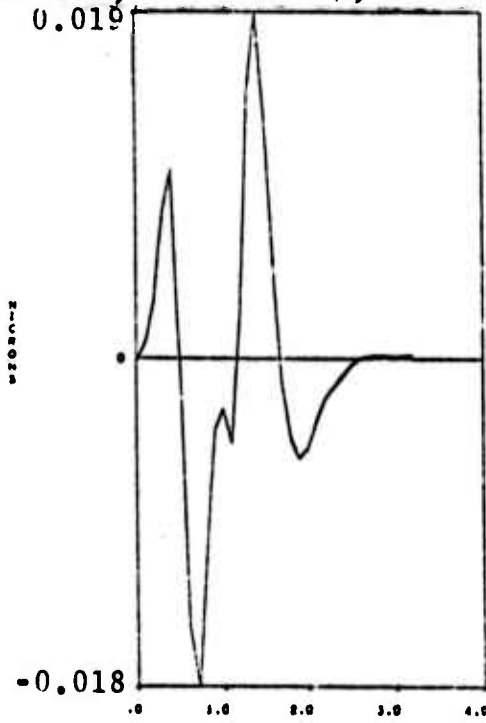
Figure 3.4 (Continued)



(c) $P+pP$, $A=20.7 \text{ m}\mu$, $T=0.75 \text{ sec}$



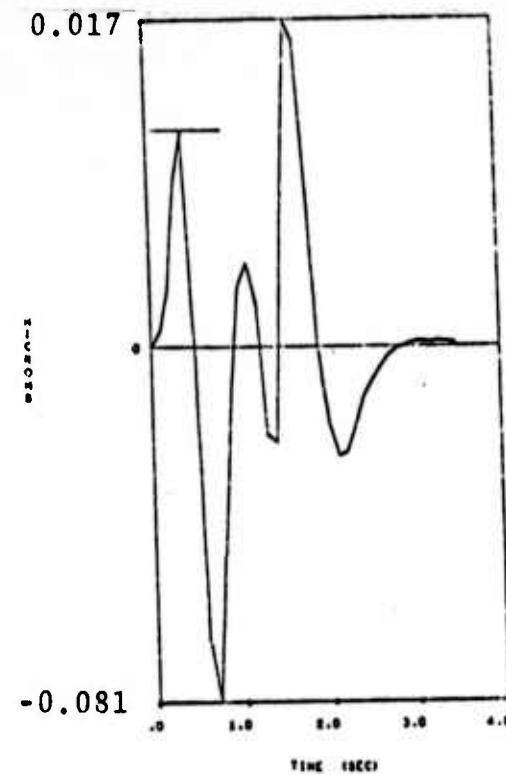
(a) $t_L = 0.49 \text{ sec}$, $A = 21.6 \text{ m}\mu$, $T = 0.95 \text{ sec}$.



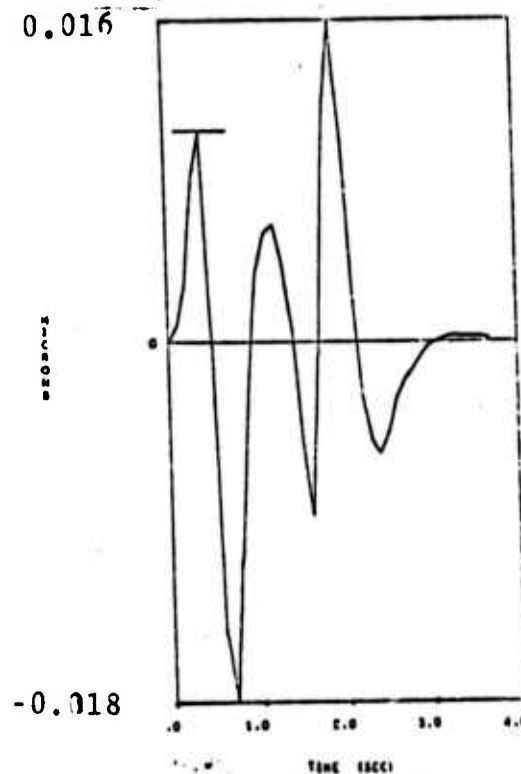
(b) $t_L = 0.73 \text{ sec}$, $A = 18.8 \text{ m}\mu$, $T = 1.4 \text{ sec}$.

Figure 3.5. $P + pP$ for a series of delay times t_L . The m_b measurement using standard procedures is indicated.

Figure 3.5 (continued)



(c) $t_L = 0.97 \text{ sec}$, $A = 14.5 \text{ m}\mu$, $T = 0.65 \text{ sec}$.



(d) $t_L = 1.2 \text{ sec}$, $A = 14.5 \text{ m}\mu$, $T = 0.65 \text{ sec}$.

In Table 3.1 the data of Figures 3.4 and 3.5 are written in terms of standard $m_b = \log A/T + B$ where B is the Gutenberg-Richter distance correction. For 4087 km a value of 3.53 was used for B .

Note that both the amplitude A and measurement period T vary with lag time. Beyond a certain lag time the two pulses cease to interfere and m_b remains constant with depth.

TABLE 3.1

Figure	Depth (DOB) (meters)	t_L (sec)	A ($m\mu$)	T (sec)	m_b
3.4	300	0.24	20.7	0.75	4.97
3.5(a)	600	0.49	21.6	0.95	4.89
3.5(b)	900	0.73	18.8	1.40	4.66
3.5(c)	1200	0.97	14.5	0.65	4.88
3.5(d)	1500	1.20	14.5	0.65	4.88

From the tabulation (3.1) we observe that the maximum variation in m_b is approximately 0.3 magnitude units. This variation clearly arises from the procedure employed in measuring m_b . That is, the amplitude and effective period used are chosen to be those associated with the largest amplitude cycle within the first two or three cycles of the P wave train. For very shallow events the P and pP signals arrive with relatively small time separation (compared to the apparent periods) and the interference is such that the second cycle of motion, corresponding to a sum of P and pP, is larger than the first cycle (pure P

wave) and the magnitude measurement is therefore increased, reflecting a pP contribution. For deeper events the pP arrival is sufficiently delayed so that little or no constructive overlap occurs, and the magnitude measurement is then made from the first cycle of motion. In this latter case the magnitude measurement is made from the direct P wave alone, while in the former case, it is made from the constructively summed P and pP phases.

If the magnitude were always measured from the first cycle of motion, then pP interference, and hence depth of burial, would have little or no effect on the m_b measurement. (This suggests a change in the m_b measurement: that is to always use the first cycle amplitude of the P wave train for the magnitude measurement. This would avoid the pP depth controlled contamination and also any sP contamination which might arise when tectonic release effects, or other S wave generating effects, are large. The latter are discussed in parts 3.2 and 3.3 of this section.)

There are three ways in which a change in source depth affects the surface wave magnitude M_s . Two of these have already been discussed, since they involve changes in near source material properties with depth. They are, first the change in the confining pressure with depth which changes the effective material strength and hence $\psi(\infty)$ (see Section II). The second is related to the fact that $M_s \propto \log [\mu \psi(\infty)]$ and since μ , the elastic rigidity, will change with depth, generally increasing with increasing depth, then M_s will also change. Of course, other material properties will, in general, change with depth as well, but these changes would be reflected in changes in $\psi(\infty)$, which have been discussed in Section II in terms of the near source material properties.

Finally the M_s value will change with depth due to the changes in the depth dependent Rayleigh wave excitation factor. However, for the range of depths involved in underground explosion tests, the changes in Rayleigh wave excitation are insignificant.

3.3 SUMMARY -- DEPTH EFFECTS

1. Since $m_b \propto \log \left[\frac{\psi(\infty)}{V_p} \right]$ and $M_s \propto \log [\mu \psi(\infty)]$, then depth changes result in changes in μ and V_p and hence variations in m_b and M_s . Further, depth changes will directly change P_0 , the confining pressure, $\psi(\infty)$ as well as other parameters controlling $\psi(\infty)$ variations in m_b and M_s .
2. The relative arrival time of P, pP and sP vary with depth. For explosions, the first two to three cycles of the P wave train usually is a composite of these phases. From this effect m_b as usually measured, may vary by roughly 0.3 magnitude units for source depth variations over the range typical for underground explosions.

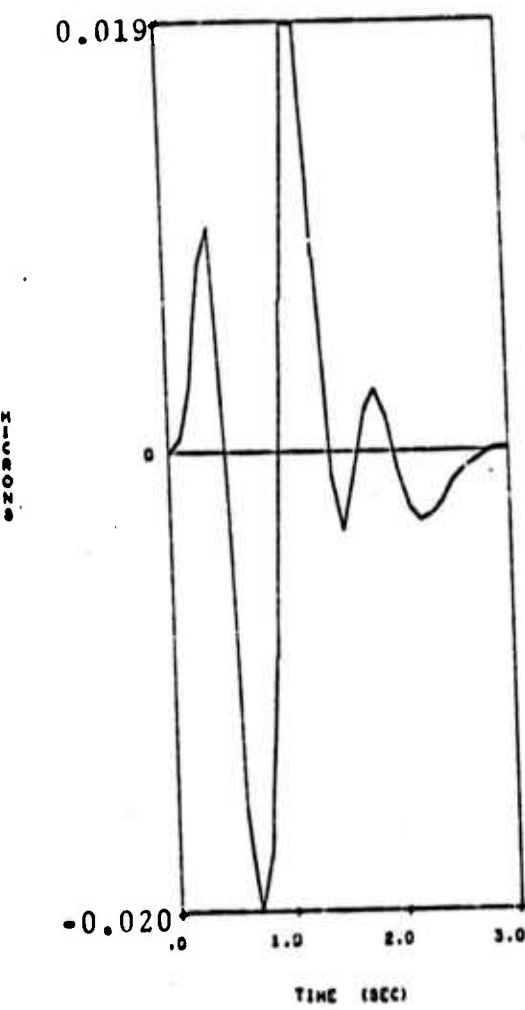
3.4 THE EFFECT OF TECTONIC RELEASE ON m_b AND M_s

The theory of the dynamic relaxation of tectonic stress due to the creation of a cavity and surrounding zone of fractured material in a prestressed geologic formation was developed by Archambeau [1972] to explain the anomalous shear waves observed from underground nuclear explosions. Tectonic release adds a double couple component to the source displacement field. The important parameters governing the tectonic release contribution to the source are the amplitude

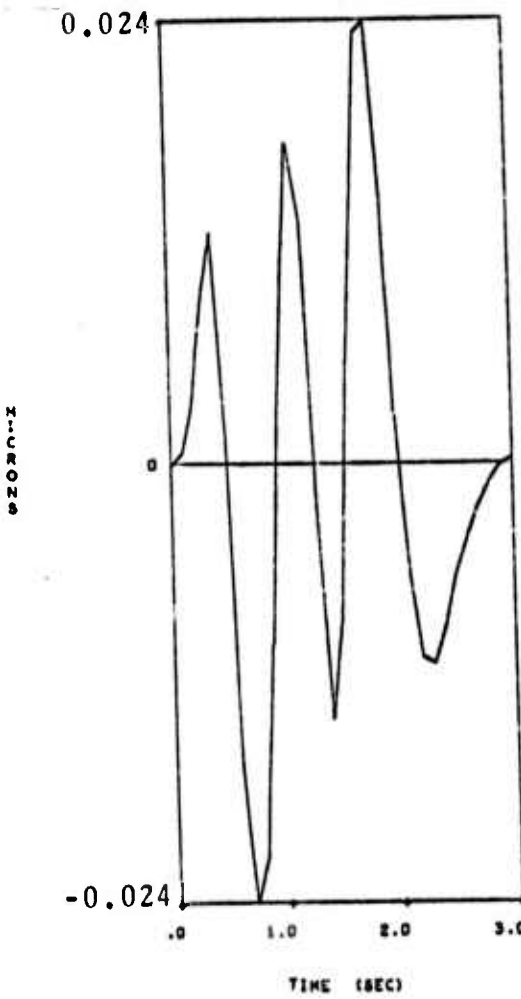
and orientation of the prestress, the radius (R_0) of the shatter zone created by the explosion shock wave and the effective size (R_s) of the prestressed region around the explosion cavity. The displacement spectral amplitudes scale directly with prestress and with the cube of the shatter zone radius. Since R_0 is expected to scale as $W^{1/3}$, the latter is equivalent to tectonic release scaling with yield. The parameter R_s controls the long period portion of the displacement spectrum. If R_s is very large, the spectrum is essentially flat while smaller R_s causes a falloff in the long period level and a peaked spectrum.

By means of an illustrative example, the kinds of effects tectonic release can have on the first few seconds of the P wave train will now be demonstrated. In Figure 3.6 two examples of the addition of tectonic release to the record of Figure 3.5a are shown. The explosion is 65 kT in tuff using Source T-3. For this explosion the computed final cavity radius was 54 meters. The shatter zone for the tectonic release was taken to be $\sim 5\frac{1}{2}$ times this radius (300 m). The parameter R_s has almost no effect on P wave ground motion as measured by an LRSM short period instrument. The convention for defining the prestress and azimuth are indicated in Figure 3.7. Note that the addition of a vertical component to the prestress field has a rather large effect on the record.

In Figure 3.8 two more examples of tectonic release are shown. In these examples the prestress field is only slightly perturbed from the horizontal. The average source-surface travel times for both P and S waves are important when tectonic release is present. The effect of changing these parameters is also illustrated in Figure 3.8. Of course, these two figures may also be interpreted to show the effect of changing depth of burial.



(a) $S_{12} = 120$ bars.



(b) $S_{12} = 120$ bars, $S_{13} = 80$ bars.

Figure 3.6. The effect of tectonic release on the first mantle arrival P wave train (vertical component). Explosion source T-3 (tuff), yield = 65 kT, $R_0 = 300$ m, $R_S = 3$ km, $H = 600$ m, $V_{PS}^S = 2.4$ km/sec, $V_{SS}^S = 1$ km/sec, $\Delta = 4087$ km, azimuth 45° .

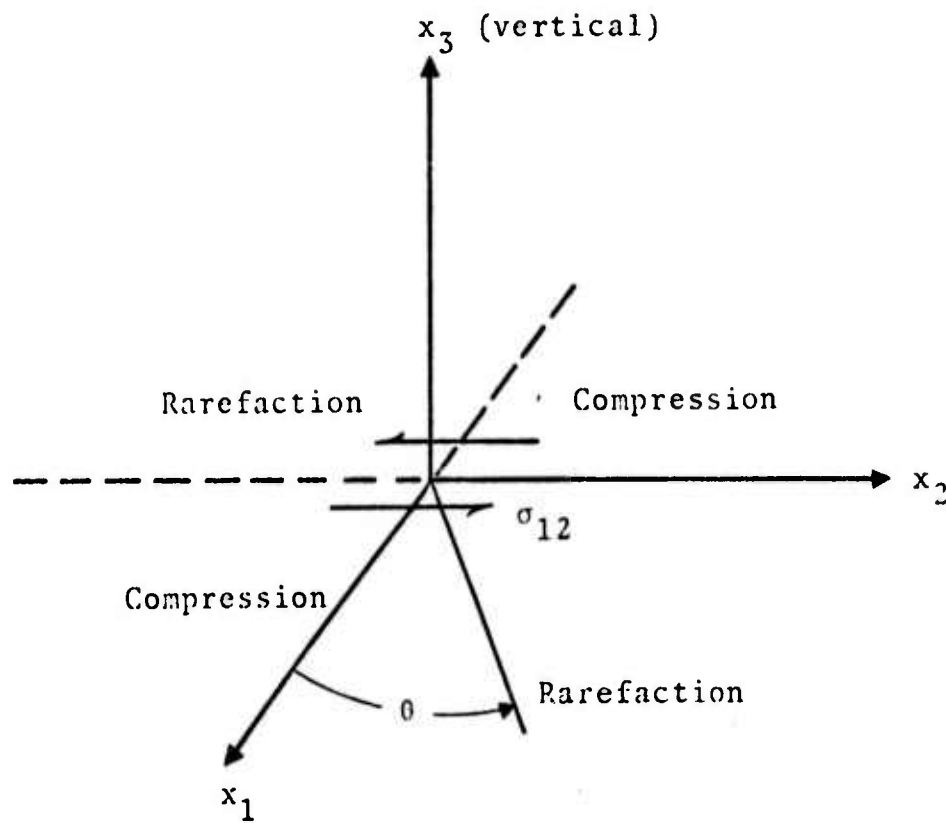
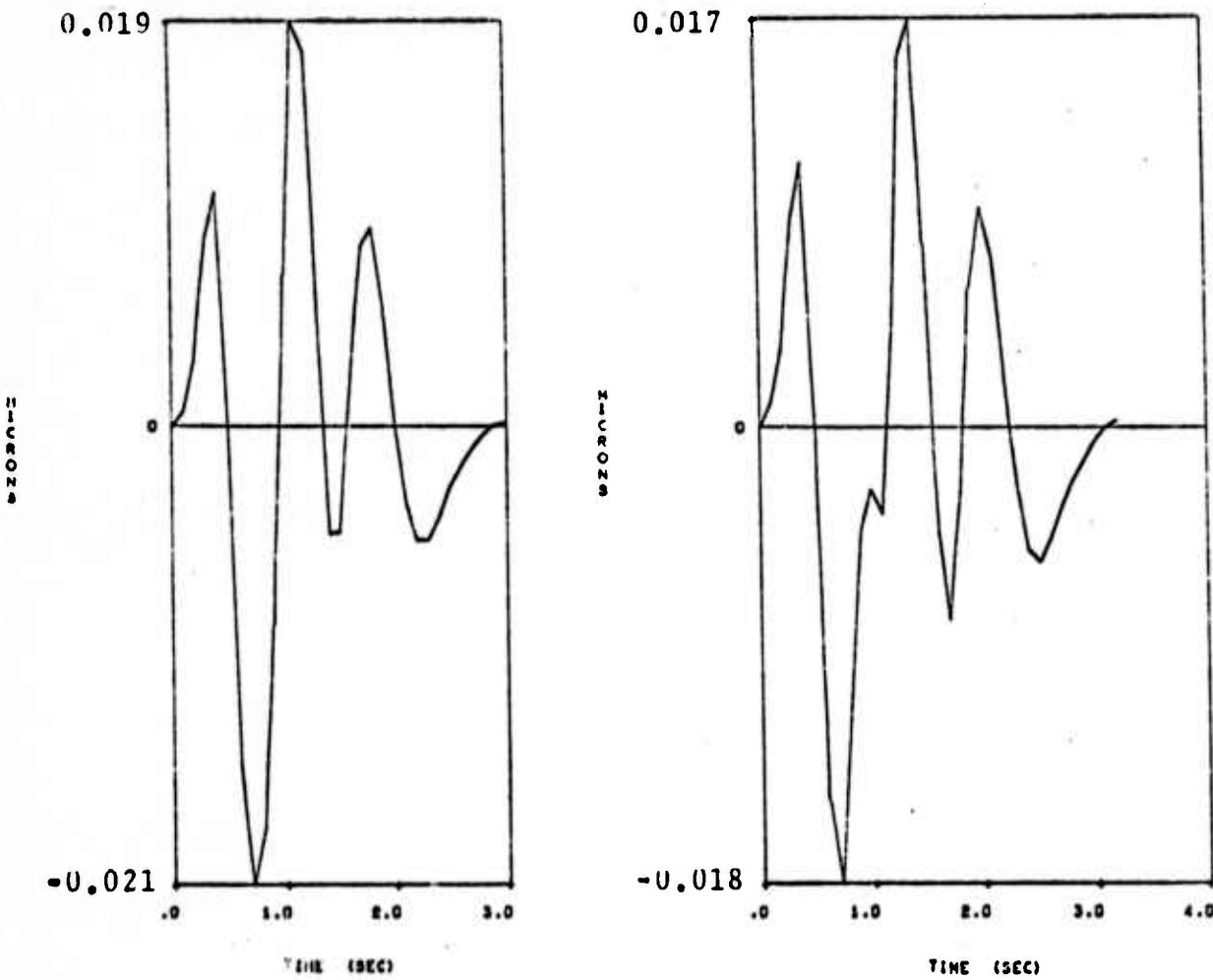


Figure 3.7. Coordinate system for defining the prestress (arrows) and source-to-receiver azimuth (θ). The first motion in the four quadrants due to an explosion in a medium with prestress $\sigma_{12} > 0$ is also indicated. Definitions of σ_{13} and σ_{23} are consistent with that of σ_{12} .



(a) $v_p^{SS} \approx 2.4 \text{ km/sec}$
 $v_s^{SS} = 1.0 \text{ km/sec}$

(b) $v_p^{SS} = 1.6 \text{ km/sec}$
 $v_s^{SS} = 0.8 \text{ km/sec}$

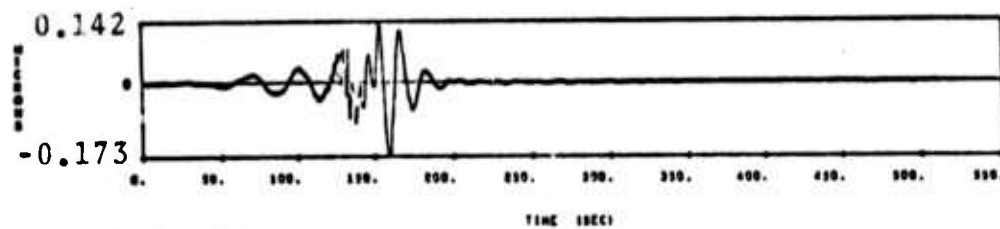
Figure 3.8. The effect of tectonic release on the first mantle arrival P wave train (vertical component). All explosion and tectonic release parameters are identical to those of Figure 3.7 except $S_{13} = 24 \text{ bars}$ for both (a) and (b).

While in none of these examples does tectonic release very strongly affect the measurement of m_b , it is important to note that the sP phase (which may be large) does arrive within the first few seconds. Thus, it may strongly influence m_b measurements under certain conditions, dependent on the magnitude and orientation of the prestress and the net time delay of the phase with respect to P.

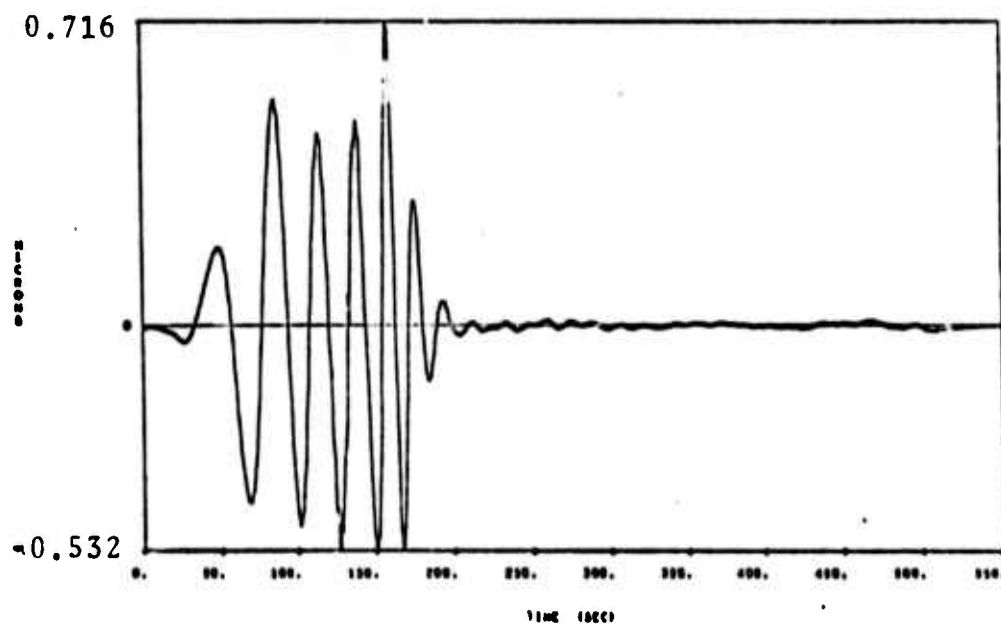
The influence that tectonic release may have on the Rayleigh wave due to an explosion is demonstrated by computing synthetic seismograms for the radial component Rayleigh wave (measured by an LRSM instrument) generated by several of the events for which P-wave seismograms were presented earlier.

In Figure 3.9 three such synthetic seismograms are shown. Figure 3.9a is a Rayleigh wave at 2000 km due to the 65 kT explosion in tuff for which body wave seismograms are shown in Figures 3.4 and 3.5. In Figures 3.6 and 3.8 the effect of two slightly different tectonic release fields on the first arrival P wave train were shown. The surface waves for these fields are shown in Figures 3.9b and c.

The presence of this level of tectonic release has a dramatic effect on the amplitude of the Rayleigh wave which is increased by nearly an order of magnitude. Note that the addition of a vertical component to the prestress field has little effect on M_s . Of course, the contribution of tectonic release to the Rayleigh wave is azimuthally dependent. This dependence is shown in Figure 3.10 where M_s enhancement due to tectonic release characterized by the parameters listed in Figure 3.8 is plotted versus azimuth. Here M_s enhancement is: M_s due to the explosion plus tectonic release minus M_s due to the explosion alone. In such a plot the effect of the source receiver travel path is removed. It is seen that the M_s enhancement is 0.7 to 1.0 units over much of the radiation pattern.



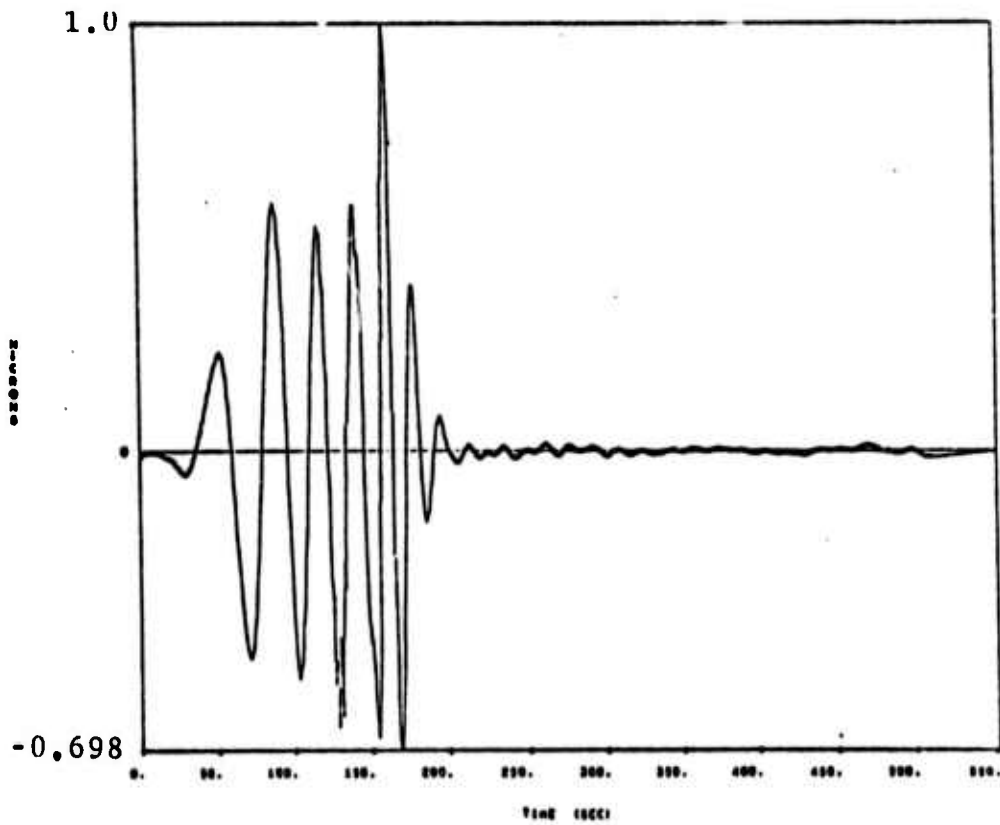
(a) Pure explosion.



(b) Explosion plus tectonic release: Prestress $S_{12} = 120$ bars.

Figure 3.9. Synthetic seismograms for the radial component of the Rayleigh waves as recorded by an LRSM long period seismogram at an epicentral distance of 2000 km and an azimuth of 45° . The explosion was modeled by the tuff source T-3 at a yield of 65 kT. The shatter zone radius $R_0 = 300$ m (~ 5 times final cavity radius) and $R_S = 3$ km.

Figure 3.9 (Continued)



(c) Explosion plus tectonic release: Prestress $S_{12} = 120$ bars,
 $S_{13} = 24$ bars.

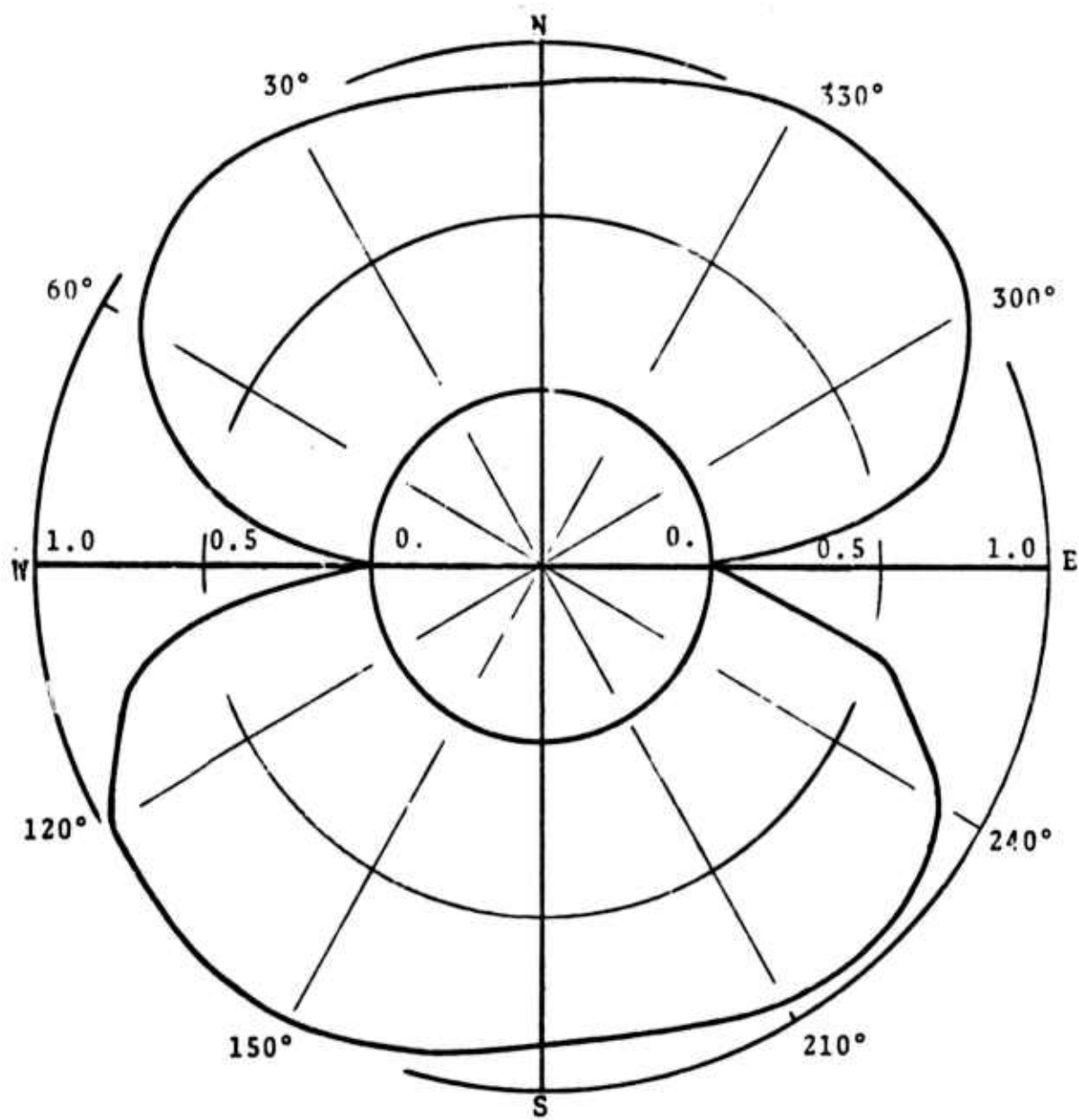


Figure 3.10. The azimuthal distribution of M_s enhancement due to tectonic release (specified by the parameters of Fig. 3.9c). On the figure, 1.0 represents the case in which M_s due to the explosion plus tectonic release is 1.0 units greater than M_s due to the spherically symmetric explosion alone.

Finally, it should be mentioned that the addition of tectonic release can account for the large Love waves often observed from underground explosions. Measurement of a surface wave magnitude based on Love waves is a direct measure of this effect, since spherically symmetric explosions should generate no Love waves.

3.5 SUMMARY -- TECTONIC RELEASE EFFECTS

Tectonic release effects on m_b and M_s include the following:

1. A free surface reflected sP phase is generated which appears within the first few seconds of the teleseismic P wave record. This phase certainly adds complexity to the record but also may influence m_b under certain circumstances, in particular when the medium is highly stressed, has a high shear velocity and/or the source is shallow.
2. Love waves are generated.
3. The Rayleigh wave may be greatly increased from its value for a similar explosion with no tectonic release.
4. All tectonic release effects are strongly dependent on the orientation and magnitude of the prestress field, and hence are strongly azimuthally dependent.

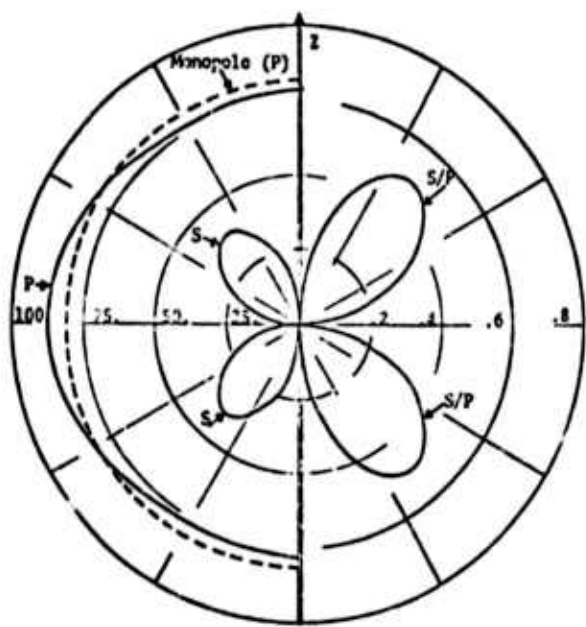
3.6 THE EFFECT OF SOURCE ASYMMETRY ON M_s AND m_b

Various factors characterizing the explosion may be responsible for adding a double couple (quadrupole) perturbation to the basic explosion center of dilatation (monopole).

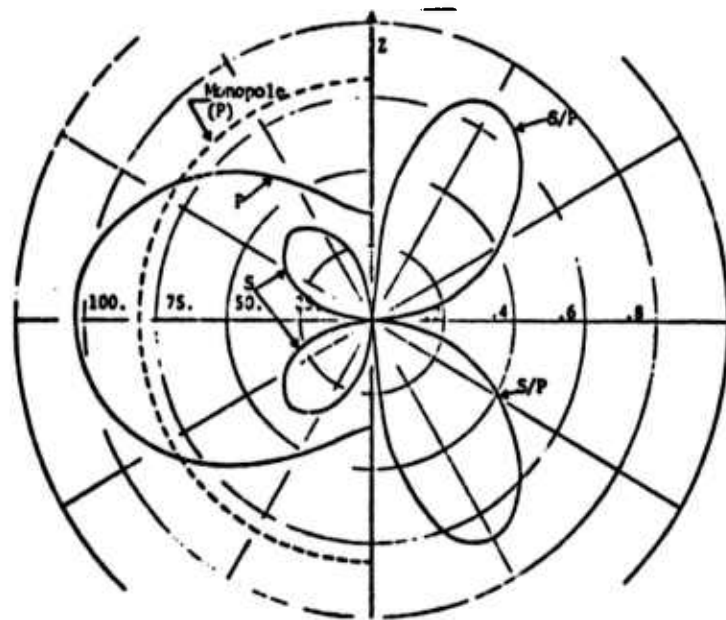
These may include jointing and other source region asymmetries, tectonic stress release due to the introduction of a large cavity in a prestressed media, earthquake triggering and the deliberate introduction of asymmetry via emplacement cavity design. The latter possibility has been discussed by Cherry, et al. [1974] in a theoretical and experimental study.

Using a computational technique in which Eulerian hydrodynamic codes were linked to a large displacement, non-linear Lagrangian code and finally to elastic wave propagation codes, Cherry, et al., computed the teleseismic ground motion generated by a nuclear explosion in a tunnel of aspect ratio 200×3 in tuff. The resulting free field displacement radiation pattern as computed 10 km from the source (retaining only far field terms) is shown in Figure 3.11. The strong double couple perturbation of the displacement field is evident, especially in the 20 second pattern.

From the displacement field pattern of Figure 3.11, Cherry, et al., computed surface waves at teleseismic distances. The effect of the layered earth structure was removed by normalizing the resulting surface wave amplitudes to those resulting from the center of dilatation component of the source. For the tunnel oriented at 45° to the horizontal, the resulting enhancement of M_s is shown in Figure 3.12. Averaged azimuthally, M_s due to this emplacement configuration was found to be 0.8 units larger than that due to the center of dilatation component alone. On the other hand, for the tunnel oriented vertically, the M_s enhancement was 0.3 units while for the horizontal orientation the average M_s enhancement was -0.4 units (M_s was less than that due to the center of dilatation component). For all orientations body wave magnitudes was essentially the



(a) 1 Second radiation pattern.



(b) 20 Second radiation pattern.

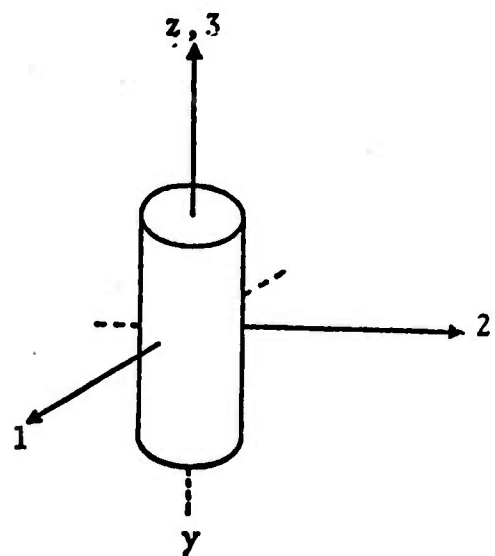


Figure 3.11. Far field displacement radiation pattern 10 km from the hypocenter. Both 1 and 20 second patterns are shown and the ratio of S to P wave displacements are indicated on the right half of each pattern. The P wave radiation from the monopole alone is also indicated.

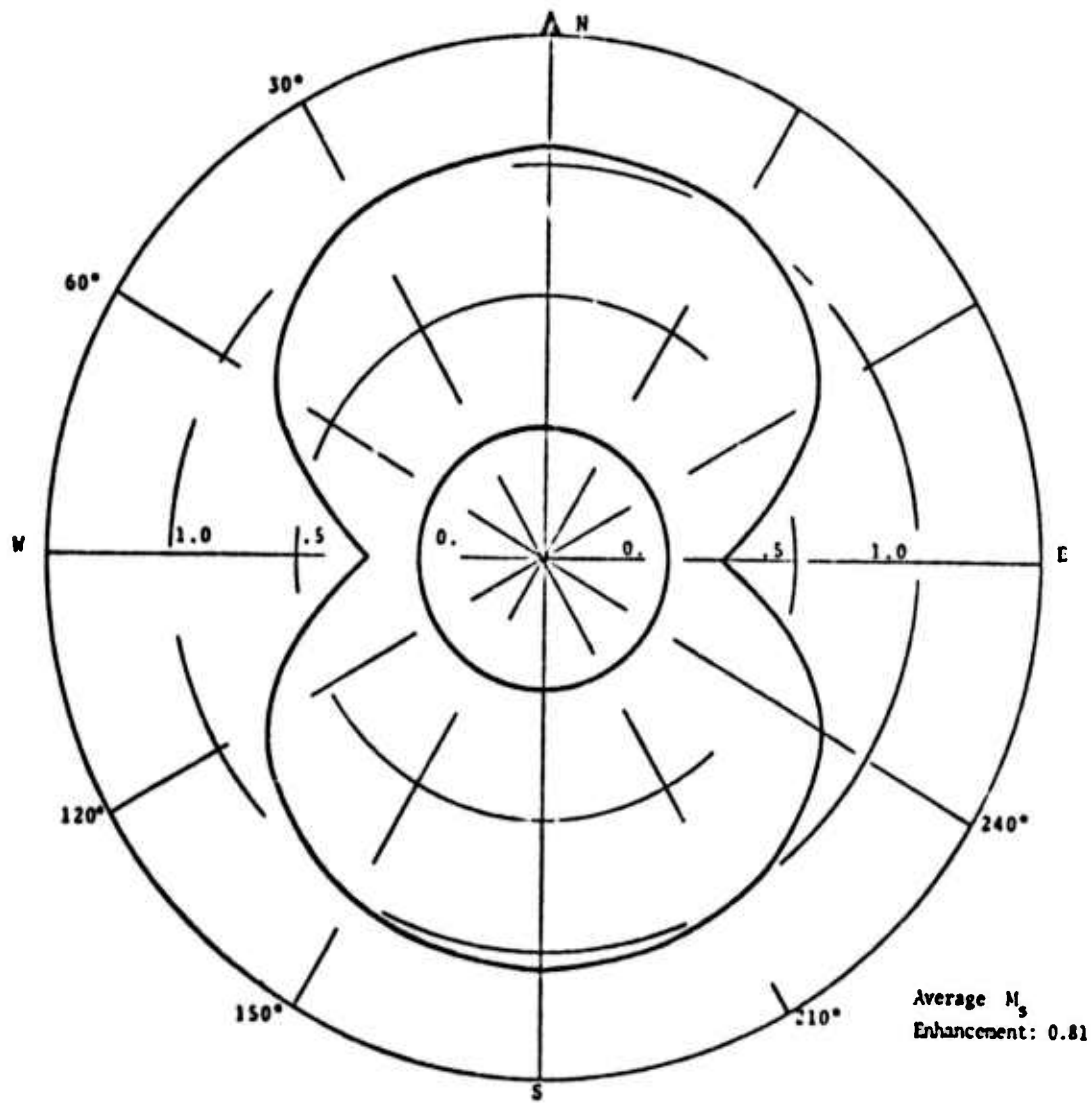


Figure 3.12. Azimuthal distribution of M_s enhancement for the tunnel oriented at 45° to the vertical.

same as that from the spherically symmetric portion of the source. This is apparent from the illustration of the source radiation pattern in Figure 3.11.

While further verification (the extremely complex calculation was carried out only once) of the quantitative results presented above is required before complete confidence is warranted, qualitatively it seems clear that a perturbation of the source from a pure center of dilatation may strongly influence surface wave amplitudes. Further, this effect is quite dependent on the orientation of the source asymmetry.

Another method by which significant source asymmetries may be introduced is the detonation of two or more explosions simultaneously or in sequence. The shock interaction of two nearby explosions detonated simultaneously is expected to generate elastic waves similar to those from an explosion in a tunnel (discussed above). On the other hand, a suite of explosions may be generated in sequence in such a way as to simulate many features of an earthquake. This constitutes an evasion procedure which has received some study (e.g., Archambeau, ACDA report, California Institute of Technology, 1974) and it appears that the m_b and M_s values of the sum of the events of the series can be determined by use of ultra narrow band filtering of both the P wave and surface wave trains from the multiple event. Because the relationship of m_b to M_s for explosions is different than for earthquakes, the event appears as an explosion under an m_b - M_s discrimination criteria. In terms of a yield estimate for such a multiple event using m_b and M_s ; one would obtain an estimate of the total yield of all the explosions of the series.

Finally, such source environment asymmetries as jointing may be responsible for many of the anomalous

radiation pattern, Love wave generation and shear wave generation effects observed from underground nuclear explosions... with other source asymmetries discussed here, this, in general, is not expected to have much effect on m_b but may have large effects on Rayleigh wave and Love wave amplitudes. Hence, yield estimates derived from m_b would be relatively unaffected.

3.7 SUMMARY

1. Source asymmetry due to emplacement cavity design produces effects similar to tectonic release with with the perturbation of m_b and M_s being of the order of that due to tectonic release with modest (75 bars) prestress. M_s levels can fluctuate by as much as a magnitude unit depending on cavity orientation. On the other hand, m_b variation from that due to a symmetric source is much smaller, on the order of 0.1 magnitude units.
2. Jointing and other medium anisotropies are thought to have effects on m_b and M_s which may be of the same order of magnitude as those produced by emplacement cavity design.
3. Multiple explosions apparently can be discriminated using revised m_b and M_s measures. The yield estimate obtained from these revised magnitude values would be (roughly) equal to the sum of the yields from all the events of the series.

IV. DEPENDENCE OF MAGNITUDE MEASUREMENTS ON VARIATIONS IN EARTH STRUCTURE

Reliable predictions of the teleseismic signature of body and surface waves excited by an underground explosion depend strongly on the knowledge of a valid velocity and Q model for the source-receiver earth structure. Variations in the velocity and Q structure of the earth's crust and upper mantle give rise to a complex seismogram. These variations must be properly modeled before statistically reliable determinations of body wave magnitudes (m_b) and surface wave magnitudes (M_s) can be obtained. In this section of the report we will emphasize the influence of the intervening earth structure on both the body wave and surface wave signatures and relate these effects to magnitude determinations.

4.1 BODY WAVES

The standard Gutenberg-Richter formula for body wave magnitude may be written

$$m_b = \log [A/T] + B , \quad (4.1)$$

where

A = Maximum zero-to-peak amplitude (millimicrons) of the most prominent P phase in the first few cycles,

T = Period of cycle on which A is measured,

B = Station correction; as usually applied (e.g., by the LRSM network) B corrects for distance only, implicitly assuming a laterally homogeneous earth.

Perhaps the most prominent characteristic of compilations of observed m_b data based on Eq. (4.1) is its wide scatter. For instance, the standard deviation associated with LRSM m_b values for U. S. underground explosions is typically as much as 0.4 or 0.5. As an example, the LRSM m_b data for the Rulison event taken from the Teledyne Geotech shot report is shown in Figure 4.1. The magnitude assigned to this event was based on data from the eleven stations at $\Delta > 17^\circ$ and was $m_b = 4.62 \pm 0.36$. The individual station magnitudes varied from 4.07 to 5.21, a range of more than a magnitude unit.

The Rulison explosion was detonated in western Colorado. However, the state of the m_b data is no different for NTS events. For example, the LRSM data for Piledriver is shown in Figure 4.2. In this case the average m_b is 5.43 ± 0.42 for $\Delta > 16^\circ$ and individual values for the ten stations in this region vary from 4.69 to 6.05, a range of 1.36 units.

There is no reason to believe that any other seismic network offers a less scattered m_b data set than the LRSM. Possible reasons for this variation that may be cited are many and include such correctable causes as calibration and measurement inconsistencies. However, by far the most important are path effects. That is, the amplitude and even the frequency content of the first motion P wave at individual stations of any seismic network will exhibit wide variation due to fundamental properties of the earth.

The P wave from an explosion which reaches several teleseismic stations has traveled a different path for each, less so in the lower mantle, more so near the surface. The effects of local and regional receiver geology on the characteristics of signals recorded are depicted in Figures 4.3a and 4.3b. Figure 4.3a shows the locations of five portable LRSM stations that were located within 4 km of the same

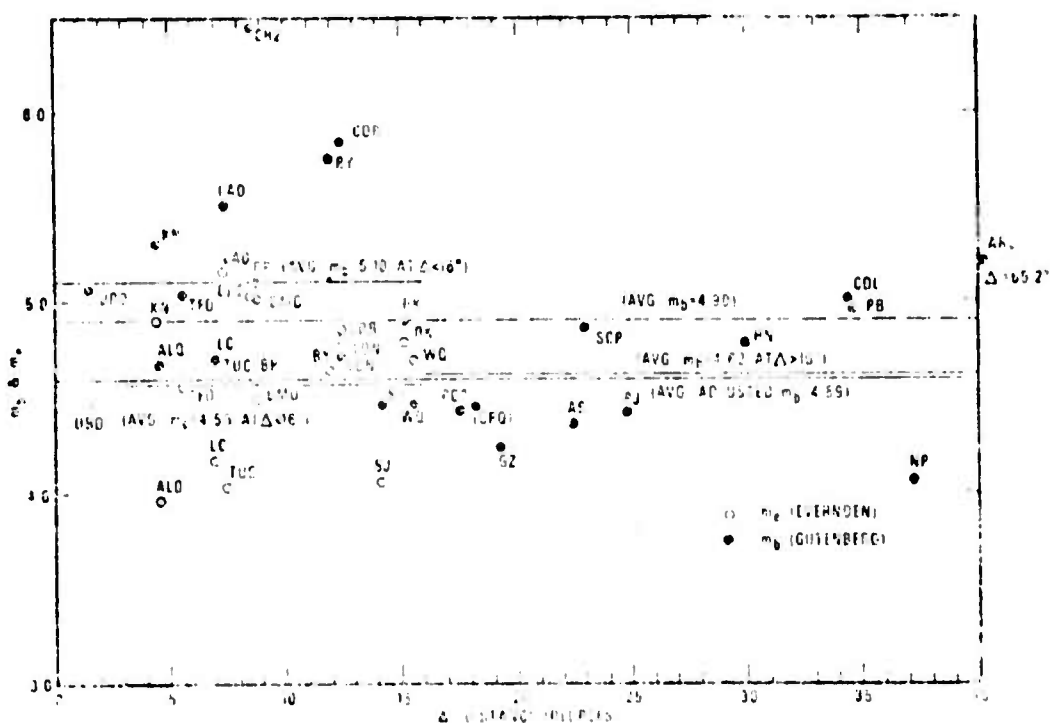


Figure 4.1. Distribution of LRSM m_b for the Rulison Event.
 (Teledyne Geotech Shot Report, Lambert, et al.,
 1972)

Reproduced from
 best available copy.

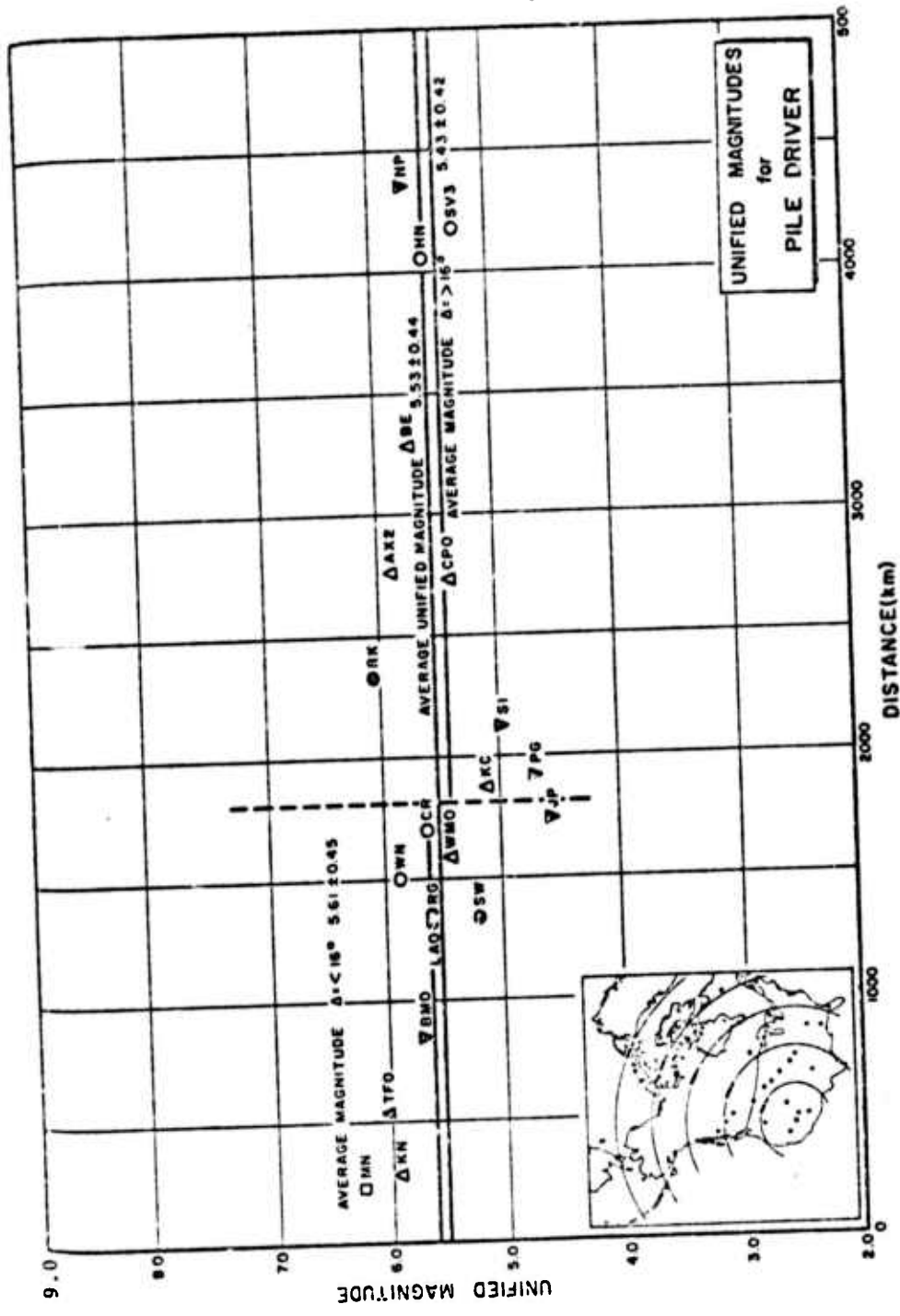


Figure 4.2. Distribution of LRSM m_b for the Piledriver Event.
(AFTAC/Teledyne Shot Report, 1966.)



Figure 4.3 (a). Locations of LRSM portable systems for the Corduroy Event. (AFTAC/Teledyne Shot Report, 1966.)

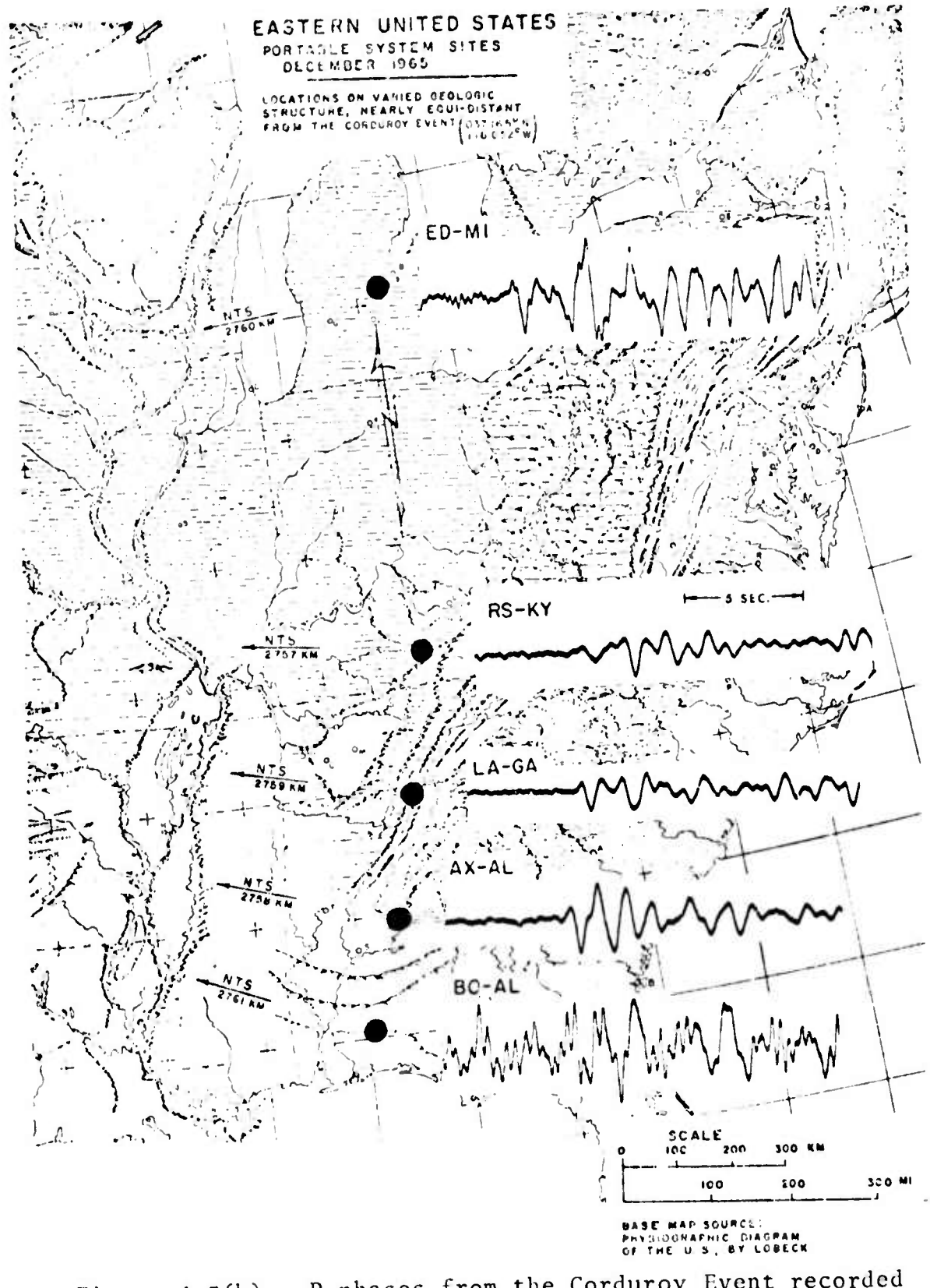


Figure 4.3(b). P phases from the Corduroy Event recorded by the LRSM portable systems, normalized to the same magnification at each site. All traces are short-period vertical at a magnification of 56.2 (at 1 cps). (AFTAC/Telodyne Shot Report, 1966.)

Reproduced from
best available copy.

distance from the shot site. While all the recording sites are located in the eastern United States, each is situated in a region of distinctly different geologic character ranging from Pre-Cambrian basement granite at AX-AL to a section of unconsolidated alluvium and glacial drift at ED-MI. Figure 4.3b shows the short-period vertical component of the P wave signals recorded at each of these five locations from the Corduroy explosion at NTS. All traces are at the same magnification. The most significant result is that m_b (AFTAC/Teledyne Shot Report, 1966) ranges from 5.2 at RS-KY to 5.7 at ED-MI and BO-Al, a spread of 0.5 m_b units.

In addition to the near station structure we must also consider the source to station travel path. Body waves propagating through a radially stratified earth structure undergo radial spreading, attenuation and dispersion. Using ray theory, a complex transfer function that accounts for these effects can be written as follows;

$$A_p(\omega) = \hat{A}_p \exp \frac{-\omega T}{2Q_p} [1 - \frac{2i}{\pi} \ln (\omega_H/\omega)] \quad (4.2)$$

where

A_p = the multiplication factor due to radial spreading,

Q_p = the dissipation constant for the ray path,

ω_H = the high frequency cutoff parameter (Strick, 1970).

The amplitude of the transfer function $|A_p(\omega)|$ at $\omega = 2\pi$ ($T = 1$ sec) for the first P arrival is plotted versus distance in Figure 4.4 for three different earth models. Each transfer function was calculated for a source depth of 1.2 km. For a particular earth model the transfer functions for other frequency components of interest for teleseismic P waves

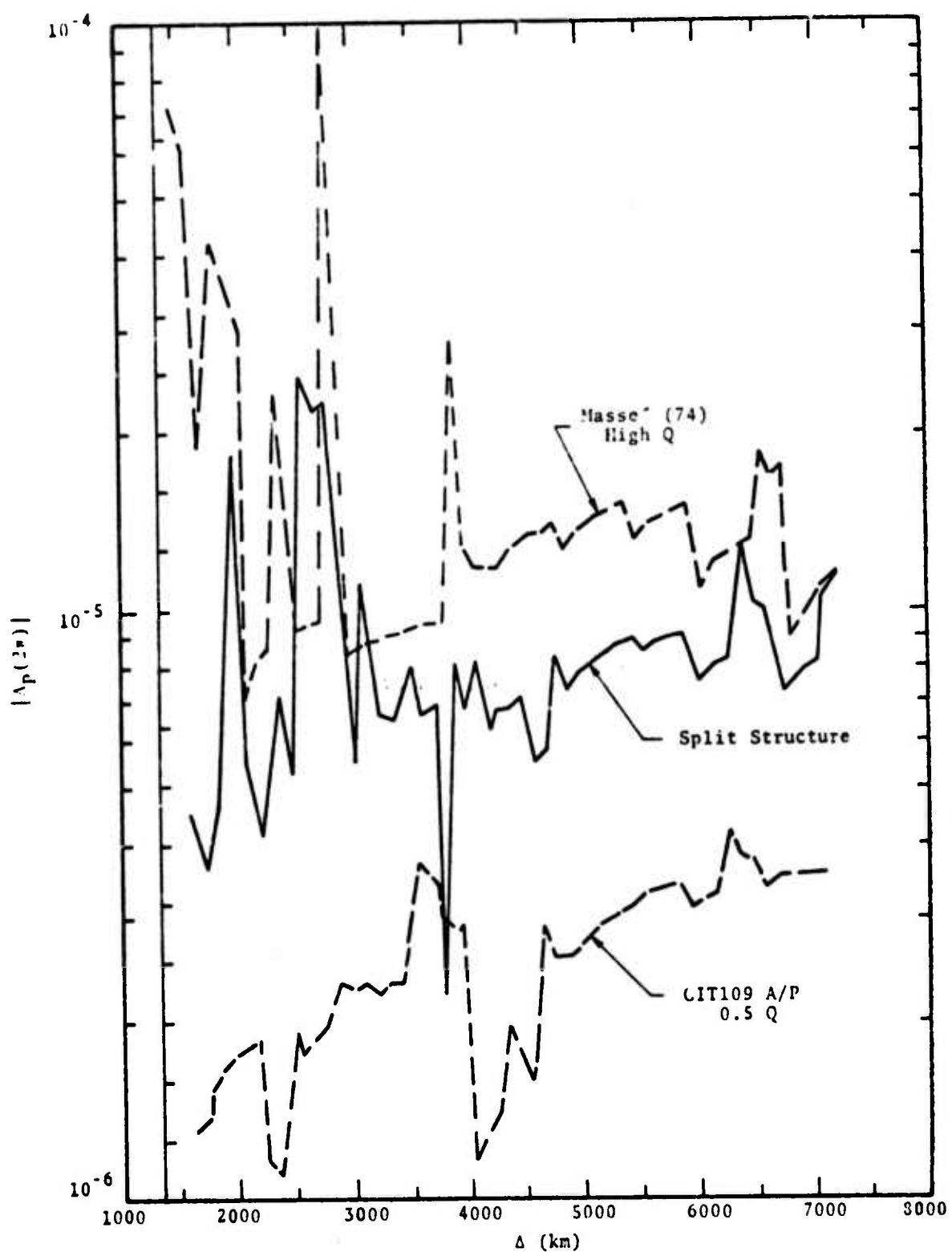


Figure 4.4. Amplitude of transfer function versus distance.

exhibit a similar distance dependence. Also, since the amplitude of the transfer function $|A_p(2\pi)|^2$ is plotted along the ordinate on a logarithmic scale the values are proportional to $\log A/T$ in Eq. (1) for $T = 1$ second. Thus the linear scale along the ordinate in Figure 4.4 gives increments in terms of m_b .

The dashed curves in Figure 4.4 give the transfer functions for two contrasting earth structures. The curve labeled CIT 109A/P 0.5Q corresponds to an earth structure appropriate, in terms of the upper mantle and crustal structure in the upper 200 km, to the Basin and Range province of the western United States (Archambeau, *et al.*, 1969). The curve labeled Masse' (74) High Q corresponds to an earth structure more appropriate to the crust and upper mantle beneath central and eastern North America. In general these two models correspond to the crust-upper mantle structure in a tectonic province (CIT 109 A/P 0.5Q) and a shield province (Masse' (74) High Q).

In terms of m_b the mean separation of these two transfer functions is approximately 0.6 units for distances greater than 2500 km. In the distance range 1600 to 2500 km the separation increases with decreasing distance from 0.6 units at 2500 km to 1.7 units at 1600 km. This latter distance range is where the major differences in the two models, namely the top 200 km of structure, are most pronounced. Considering each transfer function separately, the mean varies by 0.2 to 0.3 m_b units between 2500 and 7000 km, with a larger variation of 0.4 m_b units occurring in the distance range near 4000 km in both models.

So far, we have treated the source-receiver earth structure as being laterally homogeneous. The curve labeled "Split Structure" in Figure 4.4 is an attempt to approximate a more realistic earth model for a particular experiment

(NTS shots recorded at LRSM stations in eastern North America). Specifically, the split structure is appropriate to an earth model by two velocity/attenuation (Q) models: one for the region from the source to the ray's deepest penetration (CIT 109 A/P, 0.5Q) and one for the region from the point of deepest penetration to the receiver (Masse' (74) High Q). Note that at distances greater than 3000 km the mean of the split structure transfer function varies by 0.2 to 0.3 m_b units while at shorter distances it reflects the contrast in the two basic earth structure models.

The importance of the earth's structure on m_b can be demonstrated in another way. In Figure 4.5 $\log |A_p(2\pi)|$ (given by the solid curve and $\log A/T = m_b - B$ from Eq. (4.1) with $T = 1$ sec (given by the dashed curve) are plotted versus distance. A value of $m_b = 4.4$ was chosen in order to scale the dashed curve.

As previously mentioned, B corrects for distance only, assuming a laterally homogeneous earth. While the two curves are quite close over the distance range 3000 to 5000 km, they diverge by 0.5 m_b units or more on either end of this distance range. Clearly, to reduce the variation in m_b with distance, B must be dependent on the particular source region from which the signal emanates, the source-receiver earth structure and the regional structure in the vicinity of each receiver in a particular network.

By a careful determination of station corrections, it is possible to significantly reduce the standard deviation and range of an m_b data set. Such an exercise has been carried out by Basham (1969) on the Canadian data from NTS explosions. He was able to reduce the average standard deviation for m_b due to eleven explosions (with mean m_b ranging from 4.46 to 6.29) to 0.20. With the passage of time and accumulation of data, it is reasonable to expect further improvements.

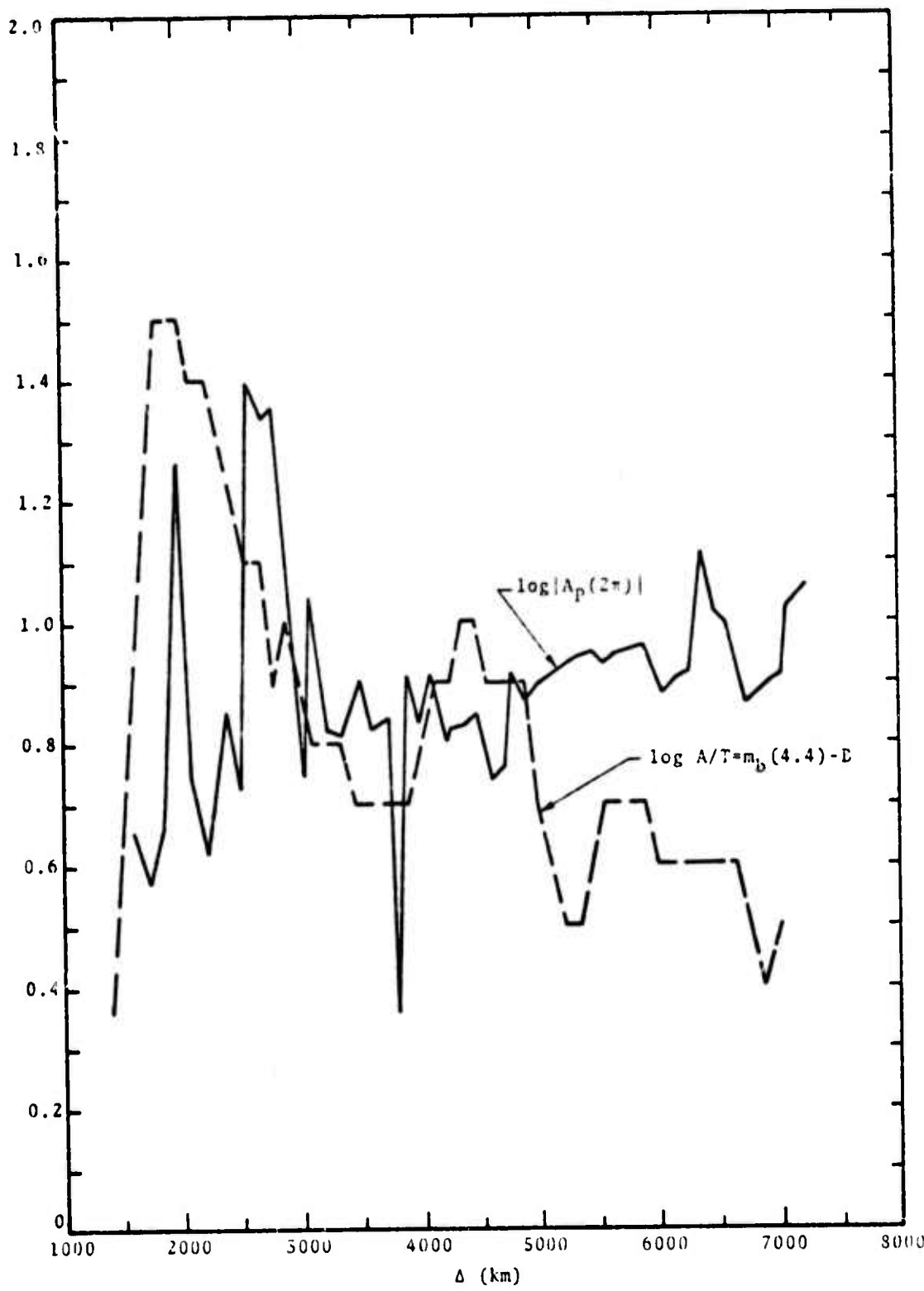


Figure 4.5. Plot of log of the transfer function for split earth model (solid curve) and the Gutenberg-Richter relationship (dashed curve) as a function of distance.

The important point to be borne in mind regarding m_b is that it is not only method dependent (i.e., which peak is measured, should the amplitude be divided by "T", etc.) but also dependent on the stations themselves; the characteristics of the sites on which they are located and the source-station travel path. Much statistical analysis of data, like that done by Basham (1969) remains to be done before reliable "mean" or "average" m_b values can be given for past or future events.

4.2 SUMMARY

1. m_b variations due to earth structure, including variations of crust-upper mantle structure at different source sites, are typically of the order of 0.5 magnitude units. Examples of variations greater than 1 magnitude unit are not uncommon however. Current models of the earth, plus taking account of local station structure and source site structure can probably reduce the station to station variation, after correction, to from 0.1 to 0.2 magnitude units and provide an average m_b which is accurate to at least 0.1 magnitude unit and probably much better than this if only random station to station fluctuations remain after correction.

4.3 SURFACE WAVES

The amplitude and frequency of surface waves recorded at teleseismic distances from underground explosions are quite sensitive to variations in the source-receiver velocity (P,S) profile of the crust and upper mantle. The effect of such variations may be seen by the following examples.

Synthetic seismograms at 4000 km from the source were generated for three earth structure models. The techniques described by Cherry, et al (1974) were used in the calculations. The three models, which are presented in Figure 4.6, are representative of the earth structure in the vicinity of NTS and are therefore quite similar. The synthetic seismograms are appropriate to the Piledriver event which was a 61 kt explosion at a burial depth of 463 meters in NTS granite.

The earth structure affects both the arrival time (group velocity) and amplitudes of the various frequency components. Surface waves from different events are often compared through the surface wave magnitude, M_s . The form of M_s used here is

$$M_s = \log \left(\frac{A_{II}}{T} \right) + 1.656 \log \Delta + 3.119 \quad (4.3)$$

where A_{II} is the maximum zero-to-peak amplitude in microns of the horizontal component of the Rayleigh wave having a period T near 20 seconds, and Δ is the epicentral distance in degrees. This formula is to be applied only in the distance range $15^\circ < \Delta < 130^\circ$.

In Table 4.1 the M_s values based on the synthetic seismograms are summarized. The seismograms were made to correspond to those written by an LRSM long period seismometer. From the table we see that the earth structure can have a noticeable effect on M_s , even for these three similar models. A more significant variation in M_s results from the choice of the phase of maximum amplitude, the Airy phase, for M_s measurements, rather than the amplitude at 20 seconds. Values of M_s from the two are really not comparable.

The extent of the M_s variations in Table 4.1, namely 0.2 units, should be considered a minimum in view of the

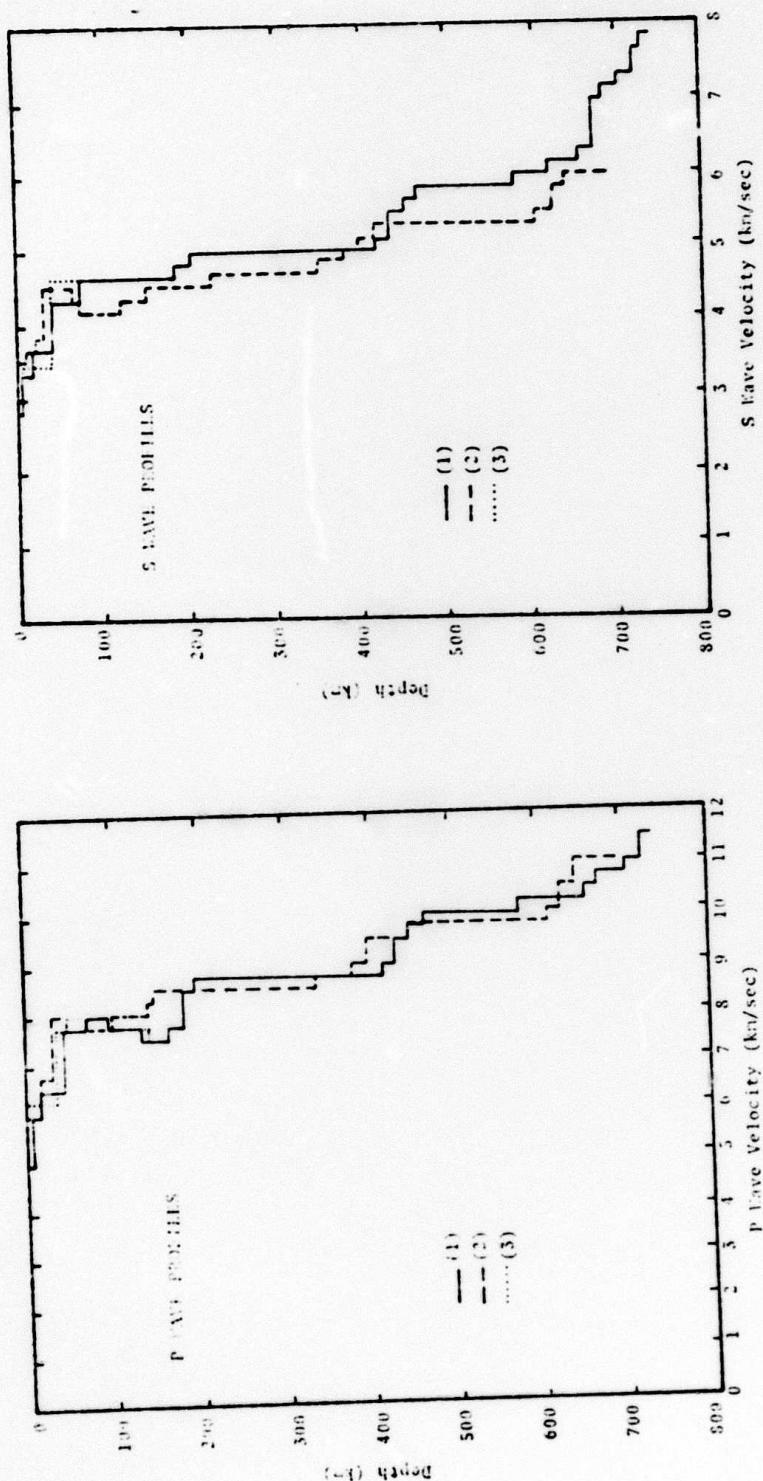


Figure 4.6. P and S wave velocity versus depth for three models of the crust and upper mantle. Line (1) is Fallon to Ruth crust, over Helmburger mantle; line (2) is model CIT 109; line (3) is NTS granite crust over Helmburger mantle.

TABLE 4.1
 M_s VALUES FOR THE MODELS OF FIGURE 6

Structure	Period (sec)	M_s
CIT 109	20	3.52
	14	4.34
NTS Granite/H.M.	20	3.45
	14	4.19
Fallon to Ruth/H.M.	20	3.37
	14	4.14

similarity of the three earth structure models (Figure 4.6). Propagation of surface waves through continental-oceanic boundaries or into regions of quite different crustal structure can, of course, result in average velocity-depth profiles quite different from those of Figure 4.6 and introduce a more significant variation into the M_s measurements.

An example of the wide scatter in M_s determinations associated with a source located in one region and the recording stations in different regions (in terms of velocity-depth profiles) is given in Figure 4.7. In particular, we see that the M_s values for the Rulison explosion, determined at $\Delta > 15^\circ$, scatter by as much as 1.4 units. The M_s measurements were made on Rayleigh waves in the period range 11 to 19 seconds with a preponderance of measurements at the shorter periods. The average M_s in this distance range is given (Lambert and Ahner, 1972) as $M_s = 3.99 \pm 0.44$ based on 12 stations (Figure 4.7). Since a large variation in M_s values (0.94 units) is observed at stations along nearly the same azimuth from Rulison and since the observed Love waves were considerably smaller (1/2 to 1/3) than Rayleigh waves of similar period, the wide scatter in M_s is most probably a result of path effects rather than possible tectonic strain release or source asymmetries.

Marshall and Basham (1972) argue that if measurements of M_s are confined to Rayleigh waves of 20 second periods, then for distances $> 25^\circ$ the largest relative difference due to path alone should be about 0.2, M_s units. However, for $\Delta < 25^\circ$, it is necessary to make careful path corrections for each source-receiver combination. That is, the accuracy of the earth structure model will determine the reliability of the M_s determination.

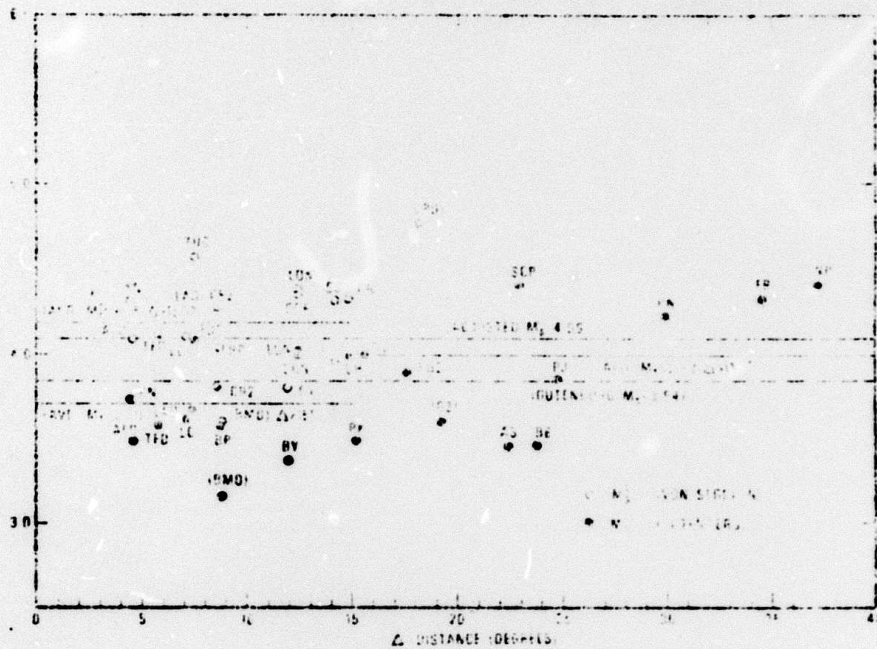


Figure 4.7. Surface wave magnitudes for Rulison.

4.4 SUMMARY

The variations in observed M_s values are to some considerable extent due to measurements of Rayleigh waves of different apparent periods at different points of observations. This can be avoided by measuring only the 20 second Rayleigh wave amplitude. True structural variations can nevertheless cause variations in point to point measurements of at least 0.2 magnitude units, and in some cases of around 0.4 units. Corrections for structure, amounting to different B value corrections for different paths based on currently obtainable crust-mantle structure, should reduce this variation to a (random) ± 0.1 to 0.2 variation and a resulting mean M_s value which should be accurate to less than 0.1 magnitude unit.

V. CONCLUSIONS

Results from a deterministic model have been presented which permit a systematic analysis of the factors which affect body wave and surface wave magnitudes, m_b and M_s , obtained from a nuclear explosion. The model merges nonlinear shock code calculations in the near-field with seismic code calculations of far-field stress wave propagation through a realistic earth structure.

In this study the model was used to produce theoretical seismograms at teleseismic distances. The theoretical seismograms were then used to determine m_b and M_s . Variations in these magnitudes have been correlated with variations in the parameters in the model.

The effect of near source material properties on magnitude were presented in Section II. Magnitude dependence on depth of burial, medium prestress and source asymmetry are discussed in Section III. Effects of earth structure on teleseismic magnitudes are given in Section IV.

The important conclusions concerning teleseismic magnitude variations are contained in each section and will not be repeated here. However, we do wish to emphasize that a complete predictive capability now exists for estimating body wave and surface wave ground motion caused by an explosive source as a function of depth of burial, emplacement technique, near-source environment, tectonic stress release and earth structure. These ground motion predictions permit an "inversion" of field observations in order to uncover device yield and also provide an evaluation of the effectiveness of existing and proposed discriminatory criteria.

Refinement of the model will certainly occur in the future. These modifications will only proceed as a result

of comparing predicted and recorded ground motion over as large a frequency and/or time interval as possible. This comparative study is proceeding at S³. The current status of the model reflects our satisfaction with its ability to match the data available to us at the present time.

VI. REFERENCES

- Archambeau, C. B., E. A. Flinn, and D. G. Lambert, "Fine Structure of the Upper Mantle," *J. Geophys. Res.*, 74, 5825-5865, 1969.
- Archambeau, C. B., "The Theory of Stress Wave Radiation from Explosions in Prestressed Media," *Geophysical J. Roy. Astr. Soc.*, 29, 329-366, 1972.
- Basham, P. W., "Canadian Magnitudes of Earthquakes and Nuclear Explosions in Southwestern North America," *Geophysical J. Roy. Astr. Soc.*, 17, 1-13, 1969.
- Basham, P. W., and R. B. Horner, "Seismic Magnitudes of Underground Nuclear Explosions," *Bull. Seis. Soc. Am.*, 63, 105-132, 1973.
- Cherry, J. T., T. C. Bache, and D. F. Patch, "The Teleseismic Ground Motion Generated by a Nuclear Explosion Detonated in a Tunnel and its Effect on the M_s/mb Discriminant," *Systems, Science and Software Final Report*, Contract No. DNA 001-73-C-0109, May 1974.
- Harkrider, D. G., "Surface Waves in Multilayered Media I. Rayleigh and Love Waves from Buried Sources in a Multilayered Elastic Half-Space," *Bull. Seis. Soc. Am.*, 54, pp. 627-679, 1964.
- Lambert, D. G., and R. O. Ahner, "Seismic Analysis of the Rulison Explosion," ARPA Report prepared by Teledyne Geotech, ARPA Order No. 1714, 1972.
- Marshall, P. D., and P. W. Basham, "Discrimination Between Earthquakes and Underground Explosions Employing an Improved M_s Scale," *Geophysical J. R. Astr. Soc.*, 28, 431-458, 1972.
- Masse', R. P., "Compressional Velocity Distribution Beneath Central and Eastern North America in the Depth Range 450-800 km," *Geophysical J. R. Astr. Soc.*, 36, 705-716, 1974.
- Strick, E., "A Predicted Pedestal Effect for Pulse Propagation in Constant-Q Solids," *Geophysics*, 35, 387-403, 1970.